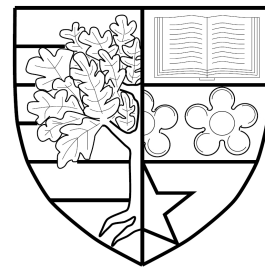


**AN INVESTIGATION OF LATTICE DYNAMICS USING
WAVEGUIDE ARRAYS**

by

Alexander Spracklen



Submitted for the degree of
Doctor of Philosophy

SCHOOL OF ENGINEERING AND PHYSICAL SCIENCES (EPS)
INSTITUTE OF PHOTONICS AND QUANTUM SCIENCES (IPAQS)
HERIOT-WATT UNIVERSITY

December 2017

The copyright in this thesis is owned by the author. Any quotation from the report or use of any of the information contained in it must acknowledge this report as the source of the quotation or information.

Abstract

The propagation of light through a periodic array of evanescently coupled optical waveguides is described by the paraxial equation. This Schrödinger-like equation closely resembles the Schrödinger equation describing the motion of a particle in a periodic potential. This close correspondence means that the evolution of the light mimics the complex dynamics of a quantum particle in a lattice. This mapping combined with the powerful capabilities of ultrafast laser inscription to precisely control the properties of the simulated lattice makes coupled optical waveguides a potent probe of solid-state phenomena. In this thesis we theoretically investigate and experimentally observe, using the photonic platform, various single-particle effects from solid-state physics. These include a new type of particle localisation due to flat energy bands and a novel type of topological edge mode which is unique to slowly-driven lattices. In addition theoretical results are presented which show how a particle subject to an artificial magnetic flux can be simulated using optical waveguides. This result paves the way for the use of photonic lattices to investigate the paradigmatic Hofstadter-Harper model and its associated topological properties. Moving beyond single-particle effects photonic lattices are capable of investigating certain phenomena associated with particle interactions, such as the dynamics of two interacting particles in one-dimension. In this thesis the dynamics of two interacting particles in two quasi one-dimensional lattices, the cross-stitch and diamond lattices, are theoretically investigated. The single-particle energy spectrums of these lattices both feature a flat band which implies that the particle's dynamics within this band are determined solely by the interaction. The theoretical work conducted in this thesis is mainly focused around the experimental platform of photonic lattices. The results, however, are derived from a Schrödinger-like equation which implies that they will be relevant to a wide community of researchers.

Acknowledgements

I sincerely thank my supervisor Prof. Erika Andersson for all her help, encouragement and advice throughout my thesis. I am very grateful that I was allowed to study the topics that interested me, it made the research and creation of this thesis a most enjoyable experience.

I am very grateful to my collaborators, Prof. Nathan Goldman, Prof. Patrik Öhberg, Prof. Robert Thomson, Dr. Sebabrata Mukherjee, and Dr. Manuel Valiente for always being available for discussion and help. I would like to extend particular thanks to Sebabrata for helping me to understand many of the experimental details about photonic lattices.

I would like to thank my family for all their support over the course of my PhD. Finally, I would like to thank my partner Katherine and our two children Isla and Nicholas. This thesis is for them.

Publications discussed within this thesis

1. Mukherjee, S., Spracklen, A., Choudhury, D., Goldman, N., Öhberg, P., Andersson, E. and Thomson, R.R., Observation of a localized flat-band state in a photonic Lieb lattice, *Physical Review Letters* **114**, 245504 (2015).
[A.S.'s contributions: Performed theoretical analysis and analysed experimental data. Contributed to manuscript preparation.]

2. Mukherjee, S., Spracklen, A., Valiente, M., Andersson, E., Öhberg, P., Goldman, N. and Thomson, R.R. Experimental observation of anomalous topological edge modes in a slowly driven photonic lattice. *Nature communications*, **8**, p.13918.
[A.S.'s contributions: Performed theoretical analysis and analysed experimental data. Contributed to manuscript preparation.]

Additional publications

1. Mukherjee, S., Spracklen, A., Choudhury, D., Goldman, N., Öhberg, P., Andersson, E. and Thomson, R.R., 2015. Modulation-assisted tunneling in laser-fabricated photonic Wannier-Stark ladders. *New Journal of Physics*, **17**(11), p.115002.
[A.S.'s contributions: Contributed to theoretical analysis. Contributed to manuscript preparation.]

2. Mukherjee, S., Valiente, M., Goldman, N., Spracklen, A., Andersson, E., Öhberg, P. and Thomson, R.R., 2016. Observation of pair tunneling and coherent destruction of tunneling in arrays of optical waveguides. *Physical Review A*, **94**(5), p.053853.
[A.S.'s contributions: Contributed to theoretical analysis. Contributed to manuscript preparation.]

Contents

1	Introduction	1
1.1	Aim of thesis	1
1.2	Thesis outline	2
2	Simulation of a quantum particle using waveguide arrays	4
2.1	Introduction	4
2.1.1	Paraxial equation	5
2.2	Coupled mode approximation	8
2.2.1	Tight-binding models	10
2.3	Chapter summary	11
3	Photonic Lieb lattice	12
3.1	Introduction	12
3.1.1	Band structure of the Lieb lattice	13
3.2	Experimental observation	15
3.3	Experimental disorder	16
3.3.1	Diagonal disorder	21
3.4	Chapter summary	22
4	Simulation of a magnetic field	23
4.1	Introduction	23
4.2	Background	25
4.2.1	Complex tunnelling elements	25
4.2.2	Floquet's theorem	27
4.2.3	Complex tunnelings in a photonic lattice	29

4.2.4	Inhomogenous bending	30
4.3	An artificial magnetic field	31
4.4	Application	35
4.4.1	Single plaquette	35
4.4.2	Square lattice	37
4.5	Chapter summary	39
5	Observation of anomalous topological edge modes	40
5.1	Introduction	40
5.1.1	Floquet engineering	42
5.1.2	Anomalous topological edge modes	44
5.2	Slowly-driven square lattice	46
5.2.1	Coupling control	49
5.3	Experimental realisation	50
5.4	Experimental disorder	53
5.4.1	Topological transition	55
5.4.2	Future work	58
5.5	Chapter summary	59
6	Two-Body physics in the cross-stitch and diamond lattices	60
6.1	Introduction	60
6.1.1	Cross-Stitch lattice	62
6.1.2	Interaction	63
6.2	Wave functions of the two-body problem	64
6.2.1	Single particle mapping	64
6.2.2	One flat-band particle	65
6.2.3	Doubly occupied bands	66
6.2.4	Fano-Anderson model	67
6.2.5	Green's function solution	68
6.2.6	Bound states	71
6.2.7	Bound state wavefunctions	72

6.3	Diamond lattice	73
6.3.1	Single-particle mapping	74
6.3.1.1	One flat-band particle	76
6.3.1.2	Two flat-band particles	77
6.3.2	Bethe ansatz	78
6.3.3	Bound state in the continuum	80
6.3.4	Bound states	82
6.4	Chapter summary	84
7	Conclusion and future work	85
7.0.1	Future work	86
A	Derivation of inhomogeneous bending couplings	88
A.1	Integrals	90

Chapter 1

Introduction

1.1 Aim of thesis

One of the great successes of early quantum mechanics was the development of electronic band theory to help explain single-particle electronic properties in a lattice. The introduction of a underlying crystalline structure gives rise to a rich variety of effects, such as bandgaps and Brillouin zones, that have no free-space counterpart and strongly effect the motion of the electron. Predicting this motion, or more generally the motion of a quantum particle in a lattice, is at the heart of solid-state physics and in the last two decades photonic lattices have emerged as a powerful experimental technique with which this motion can be simulated and probed. Photonic lattices are comprised of a periodic array of evanescently coupled optical waveguides where, at the input facet, laser light is launched into one or more of the optical waveguides. As the light travels down the input waveguides it spreads to neighbouring waveguides and these waveguides can then couple to their neighbours and so forth. Intriguingly, the interference and spreading of the light can be shown to be equivalent to the time evolution of the wavefunction of a quantum particle initially placed in the lattice. Consequently, photonic lattices offer the possibility to directly visualise the time evolution of the quantum particle's wavefunction. This analogy is based on the remarkable similarity between the paraxial equation, which governs how light propagates within these photonic lattices and the Schrödinger equation for a particle. Therefore, by the appropriate construction

of a photonic lattice the dynamics of a quantum particle in an arbitrary one or two-dimensional lattice can be studied. Moreover, if the waveguides comprising the lattice are designed to bend along the propagation direction then the evolution of the light directly simulates how a particle's wavefunction evolves when subject to a time-dependent external force. The ability to implement an external force is a valuable tool that dramatically increases the toolbox available as it can allow for the designing of effective Hamiltonians that are difficult to reproduce in static systems. The primary objective of this thesis is to work with this toolbox to study the time evolution of particles in both static and driven lattices. The theoretical results obtained are applicable to any experimental set-up as they are derived from a Schrödinger-like equation; however, in many cases the work conducted was done in close collaboration with an experimental team using photonic lattices and so the focus will be directed around this technology.

1.2 Thesis outline

In Chapter 2, the Maxwell equations that govern how light propagates in an array of waveguides will be used to derive the paraxial equation. It is the close analogy between the paraxial and the Schrödinger equations that allows the interpretation of the electric field distribution of the light as representing the wavefunction of a fictitious quantum particle. A very useful tight-binding approximation of the paraxial equation is briefly derived.

In Chapter 3, a two-dimensional lattice called the Lieb lattice is investigated. The tight-binding band structure for this lattice geometry displays a flat energy band. The presence of this flat band gives rise to a novel type of particle localisation whereby the particle is prevented from expanding by destructive interference of the wavefunction. This represents an extreme example of how the presence of a lattice can effect the motion of a particle. This flat band is investigated both theoretically and experimentally and it is shown that this flat band remains even if the perfect periodicity of the lattice is disrupted by disorder.

In Chapter 4, the bending of the waveguides along the propagation direction is discussed. The mapping between the evolution of the light within these systems to that of a particle subject to an external force is discussed. An experimental setup is proposed that makes use of these bending effects to enable the simulation of a particle moving in a lattice subject to a strong magnetic field. It is shown that the dynamics of a particle evolving under the iconic Hofstader-Harper Hamiltonian can be accurately reproduced in a photonic lattice.

In Chapter 5, the photonic analogue of an anomalous Floquet topological insulator is demonstrated. The experimental observation of a novel type of edge mode, which are unique to driven systems, using a slowly-driven photonic square lattice is presented. These topological edge modes can exist even if all the usual topological invariants that are used to describe static systems are zero. In slowly-driven systems the topological invariants used to describe static systems fail to properly capture the physics and so a new invariant, the winding number, is needed to capture the topology.

Photonic lattices are also capable of simulating two interacting particles. In Chapter 6, the interaction between two particles in the cross-stitch and diamond lattices is investigated. These quasi-one-dimensional lattices both host flat energy bands. In the flat band there is no kinetic energy and so the dynamics are completely determined by the interactions. In the case of the cross-stitch lattice the problem is mapped onto the exactly solvable Fano-Anderson model whilst for the diamond lattice a modified Bethe Ansatz is used to probe the properties of the interaction induced bound states.

In Chapter 7, the conclusions and possible future work will be presented.

Chapter 2

Simulation of a quantum particle using waveguide arrays

2.1 Introduction

The interior of a solid-state system is a complicated environment. The dynamics of the particles within these materials are the result of a multitude of competing, possibly many-body, effects which include amongst others: lattice geometry, disorder, particle-particle interactions and phononic interactions. In order to produce a satisfactory theoretical model of these complex environments it is necessary to be able to compare theoretical predictions to an experiment which has good control over these competing effects. In recent years a number of techniques such as – cold atoms in optical lattices, atoms in arrays of cavities, trapped ions experiments, quantum dots and superconducting circuits have all been proposed as being useful in the study of fundamental solid-state effects, see refs. [13, 35] for reviews. In recent years photonic lattices have also been included in this grouping as they possess a number of desirable properties [34, 79]. Firstly, they allow for excellent control over lattice geometry and disorder levels whilst allowing for the simulation of external influences such as electric fields. Secondly, they allow for complex initial states, which are not the ground state, to be generated, a feat which is difficult in many other setups. Finally, as we will see, in a photonic lattice the evolution of the light’s electric field along the propagation direction directly mimics how the parti-

cle's wavefunction evolves in time. Therefore, by measuring the output intensity a direct measure of the particle's probability distribution can be obtained.

In this chapter the Schrödinger-like paraxial equation which governs how light propagates in a photonic lattice will be derived starting from Maxwell's equations. The close analogy between the paraxial and Schrödinger equations defines a mapping that allows the experimental observations that are made in the photonic system to be converted into statements about quantum particles. This analogy can be further strengthened by utilising a coupled-mode description of the paraxial equation. The resultant system of equations can be directly related to the second quantised tight-binding models that are often used in the condensed matter and solid state fields.

2.1.1 Paraxial equation

In this section, we will derive the paraxial equation –a Schrödinger-like equation that governs how light propagates in a photonic lattice. There are several different techniques that can be used to create photonic lattices but the experimental work discussed in this thesis used laser inscription to write the optical waveguides into silica glass. In the construction process laser light is focused from the top to a tight spot inside the glass, see fig. 2.1(a). The laser light at the focus is so intense that it leads to a permanent modification of the refractive index of the glass. Therefore, by moving the glass on a controllable stage a waveguide can be written. Repeating this process at different positions allows a lattice of waveguides to be constructed. These lattices are usually written inside a glass-like dielectric medium that is isotropic, linear and non-conducting and where the charge density and current density are both zero. The Maxwell equations for materials of this type can be written as [77]

$$\nabla \times \mathbf{E} = -\mu_0 \frac{\partial \mathbf{H}}{\partial t}, \quad (2.1)$$

$$\nabla \times \mathbf{H} = n^2(x, y, z) \epsilon_0 \frac{\partial \mathbf{E}}{\partial t}, \quad (2.2)$$

$$\nabla \cdot \mathbf{D} = 0, \quad (2.3)$$

$$\nabla \cdot \mathbf{B} = 0 \quad (2.4)$$

where \mathbf{E} , $\mathbf{H} = \mu_0 \mathbf{B}$, $\mathbf{D} = \mathbf{n}^2(\mathbf{x}, \mathbf{y}, \mathbf{z})\epsilon_0 \mathbf{E}$, \mathbf{B} are the electric field, magnetic field strength, electric displacement and magnetic field respectively and ϵ_0 and μ_0 are the permittivity and permeability of free space respectively. The function $n(x, y, z)$ describes how the refractive index varies inside the material and in particular describes the position and properties of the optical waveguides. Taking the curl of Eq. (2.1) and substituting for \mathbf{H} using Eq. (2.2) and using the vector curl identity, $\nabla \times (\nabla \times \mathbf{A}) = \nabla(\nabla \cdot \mathbf{A}) - \nabla^2 \mathbf{A}$, gives

$$\nabla^2 \mathbf{E} - \nabla(\nabla \cdot \mathbf{E}) = \mu_0 \epsilon_0 \mathbf{n}^2 \frac{\partial^2 \mathbf{E}}{\partial t^2}. \quad (2.5)$$

Gauss's law, Eq. (2.3), may be used to obtain

$$\nabla^2 \mathbf{E} + \nabla \left(\frac{1}{\mathbf{n}^2} (\nabla \mathbf{n}^2) \cdot \mathbf{E} \right) = \mu_0 \epsilon_0 \mathbf{n}^2 \frac{\partial^2 \mathbf{E}}{\partial t^2}. \quad (2.6)$$

The analysis up to this point has been exact but now two key approximations are

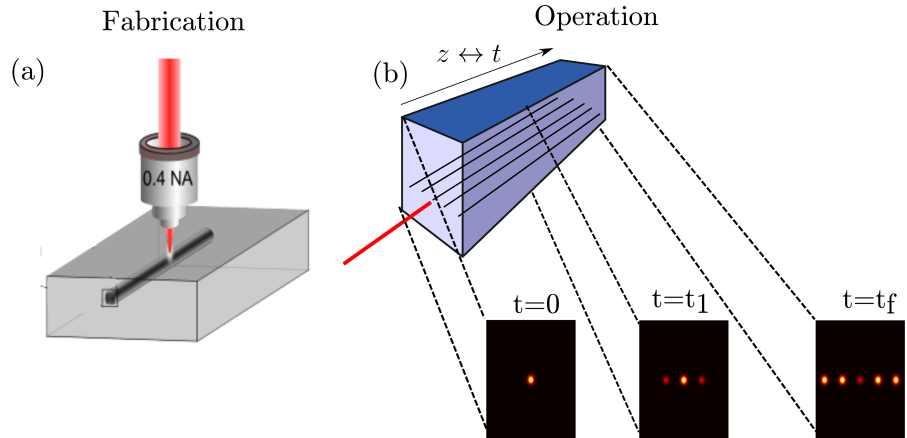


Figure 2.1: In the fabrication of a photonic lattice, fig. (a), an intense laser beam is used to inscribe a waveguide inside a glass-like medium. The glass is mounted on a movable stage which allows a lattice of waveguides to be written. In the operation of the device, fig. (b), laser light is coupled into the central waveguide. The light couples into neighbouring waveguides via evanescent coupling and the spreading of the light mimics the motion of a quantum particle in a lattice. In this analogy the propagation direction, z , plays the role of time.

introduced that simplify this wave equation. The first approximation regards the refractive index profile $n(x, y)$. The refractive index change induced by the fabricating laser is very small, roughly 10^{-3} , which allows the weakly-guiding approximation to be invoked. This approximation involves neglecting the ∇n^2 term in Eq. (2.6)

[107]. This term is the only one that contributes to coupling among the different components of the electric field. The neglecting of this term implies the model will be polarisation preserving and so only a single component of the electric field need be considered. The weakly guiding approximation therefore allows the vector wave equation to simplify to a scalar wave equation

$$\nabla^2 E(x, y, z, t) = \mu_0 \epsilon_0 n^2 \frac{\partial^2 E(x, y, z, t)}{\partial t^2}. \quad (2.7)$$

where $E(x, y, z, t)$ describes the x or y component of the electric field. The time dependence of the electric field is harmonic, $e^{-i\omega t}$, where the frequency $\omega = 2\pi c/\lambda$ is set by the speed of light, c , and the free space wavelength λ . Substituting this time dependence into the scalar wave equation gives the scalar Helmholtz equation

$$\nabla^2 E(x, y, z) = -\frac{n^2}{\lambda^2} E(x, y, z), \quad (2.8)$$

where $\lambda = \lambda/(2\pi)$ and $\mu_0 \epsilon_0 = 1/c^2$ has been used. If the wave propagation is primarily along the z -axis, then the field $E(x, y, z)$ can be represented as a slowly varying envelope and a fast oscillating wave, $E(x, y, z) = \psi(x, y, z) \exp[i\frac{n_s}{\lambda} z]$ where n_s is the refractive index of the unmodified medium. Substituting this form for E into Eq. (2.8) gives a term proportion to $\frac{\partial^2 \psi}{\partial z^2}$. Assuming ψ is slowly-varying allows this term to be dropped, the so called slowly-varying envelope approximation. Using this approximation we obtain the Schrödinger-like equation

$$i\lambda \frac{\partial}{\partial z} \psi(x, y, z) = \left[-\frac{\lambda^2}{2n_s} \nabla_{\perp}^2 + \frac{n_s^2 - n^2}{2n_s} \right] \psi(x, y, z) \quad (2.9)$$

where $\nabla_{\perp}^2 = (\frac{\partial^2}{\partial x^2} + \frac{\partial^2}{\partial y^2})$ is the transverse Laplacian. The final term can be simplified further by again invoking the weakly guiding assumption so that $n(x, y, z)^2 = (n_s + \Delta n(x, y, z))^2 \approx n_s^2 + 2n_s \Delta n(x, y, z)$ to finally give the paraxial equation

$$i\lambda \frac{\partial}{\partial z} \psi(x, y, z) = \left[-\frac{\lambda^2}{2n_s} \nabla_{\perp}^2 - \Delta n(x, y, z) \right] \psi(x, y, z). \quad (2.10)$$

The paraxial equation bears very close resemblance to the Schrödinger equation but with Planck's constant being replaced by the wavelength and the mass of the particle being given by the refractive index of the glass. The refractive index modification caused by the writing laser, Δn , defines the potential energy landscape that the fictitious particle is moving in. It is important to note that the propagation direction, z , has taken the place of time and therefore measuring the electric field at different points along the propagation direction corresponds to measuring the wavefunction at different times, see fig. 2.1(b). This mapping between t and z also effects the refractive index profile $\Delta n(x, y, z)$ which if z dependent corresponds to a time-dependent Schrödinger equation.

2.2 Coupled mode approximation

In this section a coupled-mode approximation of the paraxial equation, Eq. (2.10), is developed. The exact form of the refractive index modification induced by the writing laser is difficult to obtain experimentally which makes the paraxial equation difficult to use. The advantage of the coupled-mode approach is that it converts the paraxial equation into a theoretical model with parameters that can be easily accessed experimentally. Consider for illustration that the waveguides have been written in a square lattice geometry. The total refractive index modification can be written as a sum of the individual waveguide contributions

$$\Delta n(x, y) = \sum_{m,n} \Delta n_0(x - x_{m,n}, y - y_{m,n}), \quad (2.11)$$

where (m, n) labels the waveguide with coordinates $(x_{m,n}, y_{m,n})$ and $\Delta n_0(x, y)$ is the refractive index profile of a single isolated waveguide. The overall electric field can be expanded as [34]

$$\psi(x, y, z) = \sum_{m,n} c_{m,n}(z) u(x - x_{m,n}, y - y_{m,n}) e^{i\beta z} \quad (2.12)$$

Here β is the propagation constant of the waveguides, which are assumed identical, $u(x, y)$ is the normalised transverse profile of the eigenmode of an isolated waveguide and $c_{m,n}(z)$ quantifies the contribution of $u(x - x_{m,n}, y - y_{m,n})$ to the overall electric field. Substituting Eqs.(2.11) and (2.12) into Eq.(2.10) and using that the fact that $u(x - x_{m,n}, y - y_{m,n})$ is an eigenmode of an isolated waveguide gives [34]

$$i\lambda \sum_{m,n} \dot{c}_{m,n} u_{m,n} = - \sum_{p,q} c_{m,n} u_{m,n} V_{m,n} \quad (2.13)$$

where

$$V_{m,n} = \Delta n(x, y) - \Delta n_0(x - x_{m,n}, y - y_{m,n}) \quad (2.14)$$

where we have introduced the shorthand $u_{m,n} = u(x - x_{m,n}, y - y_{m,n})$. Multiplying by $u_{a,b}$ and integrating transversely gives the coupled-mode equations

$$i \sum_{m,n} \dot{c}_{m,n} p_{a,m}^{b,n} = - \sum_{m,n} t_{a,m}^{b,n} c_{m,n} \quad (2.15)$$

where p , t and e represent overlap integrals of the form

$$\begin{aligned} p_{a,m}^{b,n} &= \frac{1}{N} \int dx dy u_{a,b} u_{m,n}, \\ t_{a,m}^{b,n} &= \frac{1}{N\lambda} \int dx dy u_{a,b} u_{m,n} V_{m,n}, \\ N &= \int dx dy u_{m,n} u_{m,n}. \end{aligned}$$

The eigenmodes, $u_{m,n}$, typically decay exponentially which means that only a small number of these integrals are non-negligible. If the distance between adjacent guides is much larger than the full-width-half-maximum of the eigenmodes the $p_{a,m}^{b,n}$ integrals can be approximated by [40, 90]

$$p_{a,m}^{b,n} = \delta_{m,a} \delta_{n,b}. \quad (2.16)$$

The overlap integrals, $t_{a,m}^{b,n}$, cause coupling of optical energy between the mode amplitudes $c_{m,n}$ and $c_{a,b}$ via a process called evanescent coupling. The origin of this coupling is that the electromagnetic field of a waveguide mode extends beyond the

core of the waveguide and into the surrounding host material. This exponentially decaying tail is called the evanescent wave. When two waveguides are close together, such that the evanescent fields of the guided modes overlap, the waveguide modes interact with one another, this interaction results in the transfer of energy from one waveguide to another [90]. Typically this coupling decays exponentially with the separation of the waveguides and so for well separated waveguides only nearest-neighbour couplings need be included in the analysis [114]. Consequently, in the square lattice geometry the evolution of the light is now determined by the simplified coupled mode equations

$$i\dot{c}_{m,n} = -J(c_{m+1,n} + c_{m-1,n} + c_{m,n+1} + c_{m,n-1}). \quad (2.17)$$

Here J is the coupling constant which captures the effect of the evanescent coupling. A first principles calculation of this parameter is difficult as it depends upon difficult to measure quantities such as Δn_0 , ref. [90] contains calculations for J for particular forms of Δn_0 . The difficulty of calculating J directly does not present a problem as in photonic lattices this parameter can be accurately measured using a lattice consisting of only two waveguides [114].

2.2.1 Tight-binding models

An advantage of the coupled-mode formalism discussed in the previous section is its close connection to the second quantised tight-binding models that are often used in the literature to study condensed matter systems. The connection between the two approaches is most easily seen with an example and so consider a single particle moving in a square lattice governed by the tight-binding Hamiltonian

$$\hat{H}_{TB} = -J \sum_{m,n} \left(\hat{c}_{m,n}^\dagger \hat{c}_{m+1,n} + \hat{c}_{m,n}^\dagger \hat{c}_{m,n+1} \right) + h.c. \quad (2.18)$$

where $\hat{c}_{m,n}^\dagger$ creates a particle at the $(m, n)^{th}$ lattice site and J describes the tunnelling rate of the particle between nearest neighbour lattice sites. An arbitrary state of

the system can be written as

$$|\phi(t)\rangle = \sum_{m,n} \phi_{m,n}(t) \hat{c}_{m,n}^\dagger |0\rangle \quad (2.19)$$

where $|\phi_{m,n}(t)|^2$ gives the probability of finding the particle at the lattice site (m, n) at time t . The time-dependent Schrödinger equation for the probability amplitudes $\phi_{m,n}$ is given by

$$i\dot{\phi}_{m,n} = -J(\phi_{m+1,n} + \phi_{m-1,n} + \phi_{m,n+1} + \phi_{m,n-1}). \quad (2.20)$$

Comparison of Eqs. (2.17) and (2.20) shows that the evolution of the light's electric field in the photonic lattice simulates the evolution of the particle's probability amplitude in a second quantised description. It is this analogy that makes waveguide arrays such a potent probe of particle dynamics.

2.3 Chapter summary

In this chapter, we have discussed the propagation of light in coupled optical waveguides and shown the mapping between a crystalline solid and an array of coupled optical waveguides. In particular, we have examined how a coupled-mode description of the light evolution in these photonic lattice reproduces the dynamics of a particle in a lattice as predicted by a second quantised tight-binding model. In future chapters extensions to these ideas will be discussed to simulate the effects of magnetic and electric fields. These mappings will prove invaluable in using photonic lattices to demonstrate various solid-state physics phenomena.

Chapter 3

Photonic Lieb lattice

3.1 Introduction

The study of transport in lattices reveals a diverse range of phenomena ranging from cases with robust transport such as chiral edge modes in topological materials right through to situations where transport can be inhibited or even halted. The inhibition of transport stems from the presence of localised eigenstates which can lead to a particle being trapped in a subsection of the lattice. There are numerous physical mechanisms that induce this localisation and perhaps the most famous example is Anderson localisation which is due to the presence of disorder in the system [4, 101, 103]. The presence of disorder, however, is not a requirement and localisation can be induced by a wide variety of different effects including external forces [24, 26, 42], non-linearities [113], magnetic fields [135] and particle interactions, see for instance the bound state discussion of the diamond lattice in chapter 6. Interestingly, the geometry of a lattice can also lead to localisation of the wavefunction. In certain specific geometries there exist eigenfunctions that are localised and prevented from expanding or changing by destructive interference of the wavefunction. A non-exhaustive list of such lattice geometries include the Kagome, diamond, cross-stitch, pyrochlore, stub and sawtooth lattices. The presence of this destructive interference in these lattice geometries leads to the formation of perfectly flat energy bands. One of the simplest lattices where this phenomenon occurs is the Lieb lattice, see fig. 3.1(a). This two-dimensional lattice hosts three energy bands, including a perfectly

flat middle band, and in this chapter the evolution of these flat-band states is studied both theoretically and experimentally using a photonic lattice. See ref. [46, 130] for similar experimental work in photonic lattices and ref. [117] for experimental work showing the flat-band localisation with a Bose-Einstein condensate.

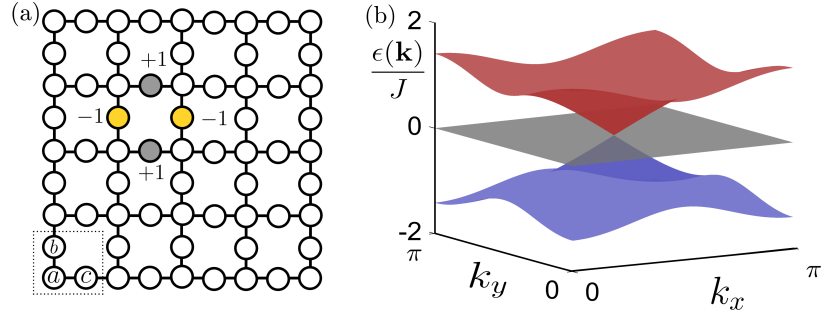


Figure 3.1: Figure (a) sketches the geometry of the Lieb lattice. The coloured circles depict the flat-band localised state that is experimentally probed. The dotted box shows the unit cell and the sublattice labelling. The numbers show the value of the wavefunction at that lattice site. Figure (b) shows the energy spectrum of the Lieb lattice and consists of two dispersive bands plus a flat energy band.

3.1.1 Band structure of the Lieb lattice

The nearest-neighbour tight-binding Hamiltonian for the Lieb Lattice can be written as

$$\hat{H} = - \sum_{m,n} (J_y \hat{b}_{m,n}^\dagger \hat{a}_{m,n} + J_y \hat{b}_{m,n-1}^\dagger \hat{a}_{m,n} + J_x \hat{c}_{m,n}^\dagger \hat{a}_{m,n} + J_x \hat{c}_{m-1,n}^\dagger \hat{a}_{m,n}) + \text{h.c.}, \quad (3.1)$$

where $\hat{a}_{n,m}$, $\hat{b}_{n,m}$ and $\hat{c}_{n,m}$ are the destruction operators for the A, B and C sites in the $(m, n)^{th}$ unit cell, respectively. Fourier transforming the real-space tight-binding Hamiltonian results in a 3x3 matrix \mathbf{k} -space Hamiltonian [89],

$$\hat{H} = \sum_{\mathbf{k}} \begin{pmatrix} \hat{a}_{\mathbf{k}}^\dagger & \hat{b}_{\mathbf{k}}^\dagger & \hat{c}_{\mathbf{k}}^\dagger \end{pmatrix} \begin{pmatrix} 0 & 2J_y \cos(k_y) & 2J_x \cos(k_x) \\ 2J_y \cos(k_y) & 0 & 0 \\ 2J_x \cos(k_x) & 0 & 0 \end{pmatrix} \begin{pmatrix} \hat{a}_{\mathbf{k}} \\ \hat{b}_{\mathbf{k}} \\ \hat{c}_{\mathbf{k}} \end{pmatrix}. \quad (3.2)$$

The energy spectrum, $\epsilon(\mathbf{k})$, consists of three bands, two dispersive and one flat band,

$$\begin{aligned}\epsilon_{\pm}(\mathbf{k}) &= \pm 2\sqrt{J_x^2 \cos^2(k_x a) + J_y^2 \cos^2(k_y a)} \\ \epsilon_0(\mathbf{k}) &= 0.\end{aligned}\tag{3.3}$$

Here ϵ_{\pm} are the energies of the dispersive bands and ϵ_0 represents the flat band; the energy spectrum is shown in fig. 3.1(b) for the case of $J_x = J_y$. The remarkable feature about the flat band is that every \mathbf{k} state within this band has the same energy. This consequently implies that any linear superposition of the flat-band's Bloch states is also an eigenstate. This degeneracy raises the possibility of constructing a localised eigenstate by an appropriate superposition of these extended Bloch states. In the Lieb lattice it is possible to show that an eigenstate consisting of only four occupied lattice sites may be constructed and that this state is composed entirely of flat band Bloch states [87]. This flat-band state is shown in fig. 3.1(a) and consists of only four lattice sites, two of which have probability amplitude $+1$ and two which have -1 . The localisation of this state may be interpreted as arising from destructive interference. The only way for this state to expand is for the probability amplitude to first tunnel to the neighbouring A sites and then expand into the rest of the lattice. However, due to the π phase difference between the neighbouring occupied sites, and assuming that the x and y tunnellings are equal, destructive interference will prevent the accumulation of any probability on the neighbouring A sites. The initial state is therefore trapped and expansion is prevented. Interestingly, this destructive interference argument suggests that disorder in the tunnelling rates could destroy the flat band as the delicate balance between neighbouring lattice sites would not be maintained. However, we will show later in the chapter that the flat band does survive even in the presence of arbitrary strength tunnelling rate disorder (so called off-diagonal disorder).

The idea that destructive interference prevents motion is neatly complemented by considering the effective mass of a particle in the flat band. The effective mass model approximates the dispersion relation of the particle as being the usual free-space one, $\epsilon(\mathbf{k}) = \frac{\hbar \mathbf{k}^2}{2m^*}$, but where the effects of the lattice and/or other perturbations

are contained in the bare mass of the particle being modified to an effective mass, denoted m^* [43]. The effective mass is related to the local curvature of the energy band, $m^* = \left(\frac{1}{\hbar} \frac{d^2 E}{dk^2}\right)^{-1}$, which for the flat band yields $m^* = \infty$. This infinite effective mass implies that the particle motion is prevented and furthermore suggests zero acceleration under an external force. See ref. [64] for a discussion of the effects of external fields on a flat band. This effective mass interpretation of the flat band is a dramatic demonstration of how lattice geometry can profoundly alter the dynamics of a particle.

3.2 Experimental observation

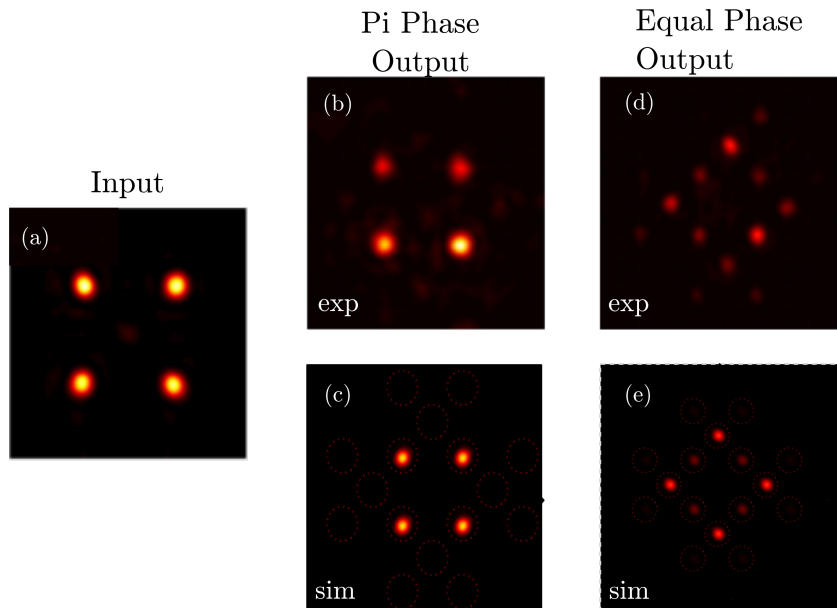


Figure 3.2: Figure comparing experimental and theoretical results for two different initial states one comprised of entirely flat-band states and the other entirely of dispersive band states. The two initial states differ only in their phase and so have identical intensity distributions, (a). In the experiment the flat-band state is largely unchanged at the output,(b), in close agreement with theoretical expectations,(c). By contrast the dispersive initial state does not remain localised and at the output has expanded into the lattice, (d,e).

The experimental investigation into the Lieb lattice involved preparing two orthogonal initial states: one comprised of only flat-band states, $|\phi_F\rangle$, and one that solely excited the dispersive bands, $|\phi_D\rangle$. The experiment then comprised measuring the evolution of these orthogonal states along the propagation direction. The flat-band initial state, $|\phi_F\rangle$, was chosen to be the one shown in fig. 3.1(a) which

consists of four occupied states of equal intensity but where the C sites are π out of phase with respect to the B sites. The dispersive state, $|\phi_D\rangle$, has the same shape as $|\phi_F\rangle$ however all the sites are in phase. The initial state $|\psi_F\rangle$ is composed entirely of flat-band states [87] and therefore should not disperse along the propagation direction. The orthogonal initial state, $|\phi_D\rangle$, by contrast has zero overlap with the flat band and therefore should disperse along the propagation direction. Fig. 3.2 shows the experimental and simulation results with (a) showing the intensity of the experimental input state, note that both $|\phi_D\rangle$ and $|\phi_F\rangle$ have the same intensity distribution, while figs. (b – e) compare the experimental and simulated results for the two different initial states. It can be clearly seen that the flat-band state, figs. (b – c), remains unchanged whilst the dispersive state, figs. (d – e), expands into the surrounding lattice.

3.3 Experimental disorder

The experiment was repeated by launching the initial states at different unit cells in order to test the homogeneity of the photonic lattice. In all cases similar, but not identical results, were observed with the output intensity distribution changing depending on the location of the launch. The presence of these slight discrepancies suggest that there is some disorder in the lattice. In order to identify the source of this disorder a number of experimental investigations were preformed with two waveguide couplers. It was observed that the primary source of disorder was due to small random variations in waveguide-to-waveguide separations that led to disorder in the tunnelling strengths between lattice sites. The experimental presence of this off-diagonal disorder motivated the theoretical investigation into the effect of this type of disorder on the flat band and this topic occupies the remainder of this chapter. See ref. [12] for a discussion of flat bands and correlated disorder. In the next section we will show how the flat band is preserved in the presence of off-diagonal disorder. In particular, in the case of a Lieb Hamiltonian with random couplings it will be shown that there are N eigenvectors which satisfy the equation

$\hat{H}_D|\eta_i\rangle = 0$ where N is the number of unit cells and \hat{H}_D is the disordered Lieb Hamiltonian.

Disordered flat band

Let $|\psi^0(\mathbf{k})\rangle$ and $|\psi^\pm(\mathbf{k})\rangle$ be eigenvectors of the disorder-free Hamiltonian \hat{H}_0 where the superscript refers to the band, see ref. [89] for their explicit form. Let \hat{H}_D be the disordered Hamiltonian. In a finite but periodic lattice, there are only a discrete number of allowed quasimomenta-there are as many values of \mathbf{k} as there are unit cells, N , and these are labelled \mathbf{k}_i . We make the following ansatz for the flat-band states, $|\eta_i\rangle$

$$|\eta_i\rangle = |\psi^0(\mathbf{k}_i)\rangle + \sum_{\mathbf{k}} c_i(\mathbf{k})[|\psi^+(\mathbf{k})\rangle + |\psi^-(\mathbf{k})\rangle], \quad (3.4)$$

where $i = 1..N$. The key steps are

1. We prove that $\hat{H}_D|\psi^0(\mathbf{k})\rangle$ only contains population on A sublattice sites.
2. We prove that the vectors $\hat{H}_D[|\psi^+(\mathbf{k})\rangle + |\psi^-(\mathbf{k})\rangle]$ only have A site population and these vectors form a basis for the A sites.
3. Combining points 1.-2. show that there exist zero-energy eigenfunctions of the form given by Eq. (3.4).
4. We show that the $|\eta_i\rangle$ are linearly independent.

More specifically, point 3. can be seen in the following way. It follows from point 1. that acting with \hat{H}_D on the first term on the rhs of $|\eta_i\rangle$, $|\psi^0(\mathbf{k}_i)\rangle$, gives a vector that only has A site population. Item 2 says that $\hat{H}_D[|\psi^+(\mathbf{k})\rangle + |\psi^-(\mathbf{k})\rangle]$ form a basis for the A sites. Therefore, any state with A site population can be written in the form $\sum_{\mathbf{k}} c(\mathbf{k})[\hat{H}_D(|\psi^+(\mathbf{k}_i)\rangle + |\psi^-(\mathbf{k}_i)\rangle)]$. In particular, by a suitable choice of $c(\mathbf{k})$, the A site population coming from $\hat{H}_D|\psi^0(\mathbf{k})\rangle$ can be cancelled, giving $\hat{H}_D|\eta_i\rangle = 0$ as desired.

Claim. The state $\hat{H}_D|\psi^0(\mathbf{k})\rangle$ only has A-site population.

Proof. The disordered Hamiltonian can be written

$$\begin{aligned}\hat{H}_D = \sum_{m,n} [& (J_{x,(m,n)}^S) \hat{c}_{m,n}^\dagger \hat{a}_{m,n} + (J_{x,(m,n)}^D) \hat{c}_{m-1,n}^\dagger \hat{a}_{m,n} \\ & + (J_{y,(m,n)}^S) \hat{b}_{m,n}^\dagger \hat{a}_{m,n} + (J_{y,(m,n)}^D) \hat{b}_{m,n-1}^\dagger \hat{a}_{m,n}] + \text{h.c.}\end{aligned}$$

where J^S refers to hopping within the same unit cell whilst J^D refers to hopping to a different unit cell. The subscripts are needed on the hoppings due to the disorder. Any arbitrary state in the Lieb lattice can be expressed as $|\xi\rangle = \sum_{x,y} [a_{x,y} \hat{a}_{x,y}^\dagger + b_{x,y} \hat{b}_{x,y}^\dagger + c_{x,y} \hat{c}_{x,y}^\dagger] |0\rangle$, where $|s_{x,y}|^2$ gives the probability of finding the particle on the s^{th} sublattice site of the $(x, y)^{th}$ unit cell. The action of \hat{H}_D on $|\xi\rangle$ produces a new vector

$$\begin{aligned}\hat{H}_D |\xi\rangle = \sum_{m,n} [& (J_{x,(m,n)}^S) a_{m,n} \hat{c}_{m,n}^\dagger + (J_{x,(m,n)}^D) a_{m,n} \hat{c}_{m-1,n}^\dagger \\ & + (J_{y,(m,n)}^S) a_{m,n} \hat{b}_{m,n}^\dagger + (J_{y,(m,n)}^D) a_{m,n} \hat{b}_{m,n-1}^\dagger \\ & + (J_{x,(m,n)}^S) c_{n,m} \hat{a}_{m,n}^\dagger + (J_{x,(m+1,n)}^D) c_{m,n} \hat{a}_{m+1,n}^\dagger \\ & + (J_{y,(m,n)}^S) b_{m,n} \hat{a}_{m,n}^\dagger + (J_{y,(m,n+1)}^D) b_{m,n} \hat{a}_{m,n+1}^\dagger] |0\rangle.\end{aligned}\quad (3.5)$$

The probability amplitude on the B and C sites of the new vector, first two lines of Eq. (3.5), is proportional to $|\xi\rangle$'s A-site probability amplitude. The vectors $|\psi^0(\mathbf{k})\rangle$ have no A site population which in turn guarantees that $\hat{H}_D |\psi^0(\mathbf{k})\rangle$ only has A site population.

Claim. $\hat{H}_D (|\psi^+(\mathbf{k})\rangle + |\psi^-(\mathbf{k})\rangle)$ has only A-site population.

Proof. This proof is very similar to that used in proving $\hat{H}_D |\psi^0(\mathbf{k})\rangle$ only has A-site population. The form of the dispersive Bloch states on the A sites is given by

$$\langle \mathbf{R}_A | \psi^\pm(\mathbf{k}) \rangle = \pm \frac{1}{\sqrt{N}} e^{-i\mathbf{k} \cdot \mathbf{R}_a} A_\mathbf{k}, \quad (3.6)$$

where \mathbf{R}_a are the lattice positions of the A sites. The two dispersive bands differ only in the sign of their $A_\mathbf{k}$ coefficients and so the vector $|\psi^+(\mathbf{k})\rangle + |\psi^-(\mathbf{k})\rangle$ has no A site population. The action of \hat{H}_D on an arbitrary vector produces a vector whose

probability amplitude on the B and C sublattice sites is proportional to the original vector's A-site probability amplitude. The vector $|\psi^+(\mathbf{k})\rangle + |\psi^-(\mathbf{k})\rangle$ has no A site popultaion which in turn guarantees that $\hat{H}_D(|\psi^+(\mathbf{k})\rangle + |\psi^-(\mathbf{k})\rangle)$ only has A site population.

Claim. The vectors $|\mu_{\mathbf{k}}\rangle = \hat{H}_D(|\psi^+(\mathbf{k})\rangle + |\psi^-(\mathbf{k})\rangle)$, are a basis for the A sites.

Proof. In the disorder-free case there are as many values of \mathbf{k} as there are unit cells, N , and so there are N different $|\mu_{\mathbf{k}}\rangle$ states. There are N A sites in the lattice, and so if it can be shown that the $|\mu_{\mathbf{k}}\rangle$ are linearly independent then $|\mu_{\mathbf{k}}\rangle$ will form a basis for the A sites.

In order to test for linear independence it must be shown that the only solution to $\sum_{\mathbf{k}} \alpha_{\mathbf{k}} |\mu_{\mathbf{k}}\rangle = 0$ is $\alpha_{\mathbf{k}} = 0 \forall \mathbf{k}$. Therefore the equation under consideration is

$$\hat{H}_D \sum_{\mathbf{k}} \alpha_{\mathbf{k}} [|\psi^+(\mathbf{k})\rangle + |\psi^-(\mathbf{k})\rangle] = 0.$$

If a solution would exist which does not have $\alpha_{\mathbf{k}} \neq 0 \forall \mathbf{k}$ then this solution, denoted $|D\rangle$, satisfies $\hat{H}_D|D\rangle = 0$ and hence represents a zero-energy eigenstate. In order for $|D\rangle$ to be a zero energy eigenvector equation it must satisfy

$$0 = \sum_{\mathbf{k}} e^{-i\mathbf{k}\mathbf{R}_A} \left\{ \alpha_{\mathbf{k}} \left[J_{x,(m,n)}^S e^{-ik_x} + J_{x,(m,n)}^D e^{ik_x} + (J_{y,(m,n)}^S e^{-ik_y} + J_{y,(m,n)}^D e^{ik_y}) \cos(k_y) \sec(k_x) \right] \right\} \quad (3.7)$$

The phase and magnitude of the coefficients in this sum depend on the disordered tunnelling rates in the $(m, n)^{th}$ unit cell. Therefore, in order for this equality to hold for every unit cell the term inside the curly brackets must equal zero. The term within the square brackets cannot equal zero as the disordered hoppings are all real and positive. Therefore for this equality to hold it is required that $\alpha_{\mathbf{k}} = 0$. This statement implies that the only solution to $\sum_{\mathbf{k}} \alpha_{\mathbf{k}} |\mu(\mathbf{k})\rangle = 0$ is $\alpha_{\mathbf{k}} = 0$ which in turn implies the $|\mu(\mathbf{k})\rangle$ are linearly independent and hence form a basis for the A sites.

Zero-energy eigenstates

The consequence of the $|\mu_{\mathbf{k}}\rangle$ being linearly independent is that the $|\mu_{\mathbf{k}}\rangle$ form a basis for the A sites. This is crucial as it allows the creation of zero-energy eigenstates of the disordered lattice. A zero-energy eigenstate has the form

$$|\eta^0\rangle = |\psi^0(\mathbf{k})\rangle + \sum_{\mathbf{k}} c(\mathbf{k})(|\psi^+(\mathbf{k})\rangle + |\psi^-(\mathbf{k})\rangle). \quad (3.8)$$

A zero-energy eigenvector must satisfy $\hat{H}_D|\eta^0\rangle = 0$, and this holds for the state of Eq. (3.8) as shown now. Acting with \hat{H}_D on the first term on the rhs of Eq. (3.8) gives a vector that only has A site population. Acting with \hat{H}_D on the second term gives $\sum_{\mathbf{k}} c(\mathbf{k})|\mu^k\rangle$ where $|\mu^k\rangle$ have population only on the A sites and form a basis for the A sites. Therefore, by a suitable choice of $c(\mathbf{k})$, the A site population coming from $\hat{H}_D|\psi^0(\mathbf{k})\rangle$ can be cancelled giving $\hat{H}_D|\eta^0\rangle = 0$ as desired.

Flat band

A whole family of such zero-energy eigenvectors can be created by changing the value of \mathbf{k} that is used for $|\psi^0(\mathbf{k})\rangle$. A general member of this family has the form

$$|\eta_i^0\rangle = |\psi^0(\mathbf{k}_i)\rangle + \sum_{\mathbf{k}} c_i(\mathbf{k})(|\psi^+(\mathbf{k})\rangle + |\psi^-(\mathbf{k})\rangle).$$

Claim. The $|\eta_i^0\rangle$ are linearly independent.

Proof. The vectors $|\eta_i^0\rangle$ are linearly independent if the only solution to the equation $\sum_i \alpha_i |\eta_i^0\rangle = 0$ is $\alpha_i = 0 \forall i$. Inserting the explicit form for the $|\eta_i^0\rangle$ gives

$$0 = \sum_i \alpha_i \left[|\psi^0(\mathbf{k}_i)\rangle + \sum_{\mathbf{k}} c_i(\mathbf{k})(|\psi^+(\mathbf{k})\rangle + |\psi^-(\mathbf{k})\rangle) \right].$$

The term inside the square brackets is a linear combination of disorder-free eigenstates, and therefore it cannot be zero as this would mean that the disorder-free eigenvectors were not linearly independent. The other possibility is that the brackets corresponding to different \mathbf{k} values cancel. Therefore assume that there is a

solution with $\alpha_i \neq 0$ for some i . Let one of the non-zero α_i be α_0 . Then

$$0 = \alpha_0 |\psi^0(\mathbf{k}_0)\rangle + \alpha_0 \sum_{\mathbf{k}} c_0(\mathbf{k}) (|\psi^+(\mathbf{k})\rangle + |\psi^-(\mathbf{k})\rangle) \\ + \sum_{i,i \neq 0} \alpha_i [|\psi^0(\mathbf{k}_i)\rangle + \sum_{\mathbf{k}} c_i(\mathbf{k}) (|\psi^+(\mathbf{k})\rangle + |\psi^-(\mathbf{k})\rangle)]$$

and

$$|\psi^0(\mathbf{k}_0)\rangle = \sum_{\mathbf{k}} c_0(\mathbf{k}) (|\psi^+(\mathbf{k})\rangle + |\psi^-(\mathbf{k})\rangle) \\ + \frac{1}{\alpha_0} \sum_{i,i \neq 0} \alpha_i [|\psi^0(\mathbf{k}_i)\rangle + \sum_{\mathbf{k}} c_i(\mathbf{k}) (|\psi^+(\mathbf{k})\rangle + |\psi^-(\mathbf{k})\rangle)].$$

This expression violates the linear independence of the disorder-free eigenvectors, which are a basis. Therefore, the only solution is $\alpha_i = 0 \forall i$, and therefore the $|\eta_i\rangle$ are linearly independent. These linearly independent eigenvectors when combined with other linearly independent non-zero energy state can be converted into a orthonormal basis via the Gram-Schmidt process. This procedure does not change the eigenvalues, and so the disordered Hamiltonian always possesses N zero-energy orthonormal eigenvectors, where N is the number of unit cells. Hence the flat band persists even in the presence of disorder.

3.3.1 Diagonal disorder

Finally we would like to note that in the case of diagonal disorder it can be seen numerically that the flat band is destroyed by this type of disorder. The breaking of this flat band can be directly related to the diagonal disorder using the Bauer-Fike theorem [8]. The theorem states that the eigenvalues of the perturbed matrix, i.e. the Hamiltonian with disorder, cannot differ from the eigenvalues of the disorder-free Hamiltonian by more than the largest eigenvalue of the perturbing Hamiltonian. As the perturbation matrix is diagonal the eigenvalues are easily obtained. Therefore, for weak disorder the flat band is almost maintained. In the very long time limit the experimental state would disperse throughout the lattice for diagonal disorder.

The same is not true for off-diagonal disorder. In this case the flat band persists, as shown above, and therefore the projection of the original state onto this flat band will remain localised.

3.4 Chapter summary

In this chapter, we have presented a photonic realisation of a two-dimensional Lieb lattice using waveguide arrays. This lattice supports three energy bands, including a perfectly flat middle band with an infinite effective mass. We analyse, both experimentally and theoretically, the evolution of localised flat-band states, and show that these states remain localised along the propagation direction. We have shown theoretically that the flat band persists even in the presence of arbitrary strength tunnelling rate disorder, off-diagonal disorder. In addition to having potential technical applications involving diffractionless image transport [132, 139] flat bands also present the potential for investigating novel non-linear dynamics owing to the absence of any kinetic terms [71, 73, 131] in these bands.

Chapter 4

Simulation of a magnetic field

4.1 Introduction

In recent years the importance of ultrafast laser-written photonic lattices as an experimental tool to investigate coherent quantum phenomena has increased greatly. In particular, the equivalence between how light evolves within these waveguide arrays to how a quantum particle moves in a lattice has made these systems a potent tool in probing particle behaviour. One of the most productive applications of this platform is in simulating the effect of an external electric field. This utilisation relies on the flexibility in waveguide positioning that is allowed by the laser inscription process to curve the array along the propagation direction. The evolution of the light within this curved array now simulates the dynamics of a particle, in a lattice, subject to an external electric field. This analogy has allowed the experimental observation of a number of theoretically predicted solid-state effects such as Bloch oscillations [70], Landau-Zener tunneling [23] and topologically protected chiral edge modes [100] amongst others. The capability of photonic lattices, as an experimental tool, would be further enhanced by the ability to simulate a magnetic field. This capacity, for example, would allow the simulation of the paradigmatic example of the quantum Hall effect: the Hofstadter-Harper Hamiltonian [10, 49, 55] which describes a single-particle moving in a square lattice exposed to a strong uniform magnetic field. The application of a magnetic field dramatically enriches the physics as while the magnetic field is translationally invariant the gauge potential generating the

magnetic field need not be. The magnetic field therefore gives rise to a new unit cell in the lattice called the magnetic unit cell which can be either be commensurate or incommensurate with the normal field-free unit cell. The interplay between these length scales causes the resulting single-particle energy spectrum to show a fractal structure as a function of the magnetic flux per unit cell, a result which is known as the Hofstadter butterfly. In addition to this rich spectral behaviour the Hofstader-Harper model is one of the simplest tight-binding lattice model exhibiting topological transport properties as, for certain values of magnetic flux, there exist well-separated energy bands that can be associated non-trivial topological invariants, i.e. non-zero Chern numbers [68, 119]. These topological properties are directly related to the existence of robust chiral edge states [51, 52, 97] and so realising this model using laser-written photonic lattices would allow for the study of these rich phenomena in a highly controllable environment. The Hofstader-Harper model has been realised in several different experimental platforms including cold atoms [1, 3, 62, 86, 112, 116] and photonics [27, 47, 48] but not in laser-written waveguide arrays. There has been a theoretical suggestion to realise an effective magnetic field [81] but this technique required precise control of the propagation constant along the propagation direction. In principle this is possible by altering the write-speed of the fabricating laser however changing it dynamically and from waveguide to waveguide is difficult. In this work we use the powerful ability present in photonic lattices to individually control waveguide placement to *inhomogeneously* curve a lattice of waveguides and show through theory and numerical simulation that an artificial magnetic field can be created. Whilst this chapter focuses on square lattices the theoretical work conducted herein would apply to any lattice where the nearest neighbour bonds are perpendicular to one another. These geometries include a number of interesting possibilities such as the Lieb [6, 39] and one-dimensional diamond lattices [17, 134, 135].

4.2 Background

The most widely used mechanism for incorporating a magnetic field into a tight-binding description of a lattice is to use the Peierls substitution [93]. The substitution involves taking the tight-binding description of the lattice, in the absence of a field, and making a replacement given by

$$t_{m,a}^{n,b} \rightarrow t_{m,a}^{n,b} e^{-i\phi_{m,a}^{n,b}} = t_{m,a}^{n,b} \exp\left[-\frac{iq}{\hbar} \int_{r_{a,b}}^{r_{m,n}} d\mathbf{r} \cdot \mathbf{A}\right] \quad (4.1)$$

where $t_{m,a}^{n,b}$ is the coupling between the sites $r_{a,b}$ and $r_{m,n}$, $\mathbf{A}(\mathbf{r})$ is the vector potential generating the magnetic field and q is the charge of the particle. The exact form of the Peierls phase, $\phi_{m,a}^{n,b}$, on each bond depends upon the choice of gauge that is made for the vector potential. The sum, however, of the Peierls phase around an elementary plaquette of the lattice is a gauge invariant quantity and can be understood physically as being proportional to the magnetic flux per unit cell [10]

$$\Phi = \sum_{\text{Plaquette}} \phi_{m,a}^{n,b} = \frac{q}{\hbar} \int_{A_p} \mathbf{B}(\mathbf{r}) d\mathbf{n}, \quad (4.2)$$

where \mathbf{n} is the normal vector of the surface A_p enclosed by the bonds of the elementary plaquette and q is the charge of the particle. Fig. 4.1 illustrates how this quantity is obtained on a square lattice. The creation of complex tunnelling elements is therefore a critical component of generating an artificial magnetic field and in the next section a useful mechanism for achieving this is discussed.

4.2.1 Complex tunnelling elements

The generation of complex tunnelling elements can be achieved in photonic lattices using a technique inspired by photon-assisted tunnelling in cold-atom experiments [9, 25, 106]. Photon-assisted tunnelling is composed of two parts and we will briefly describe the mechanism as it plays such a central role in the proposal used in this chapter. The starting point is the tight-binding equations describing a particle

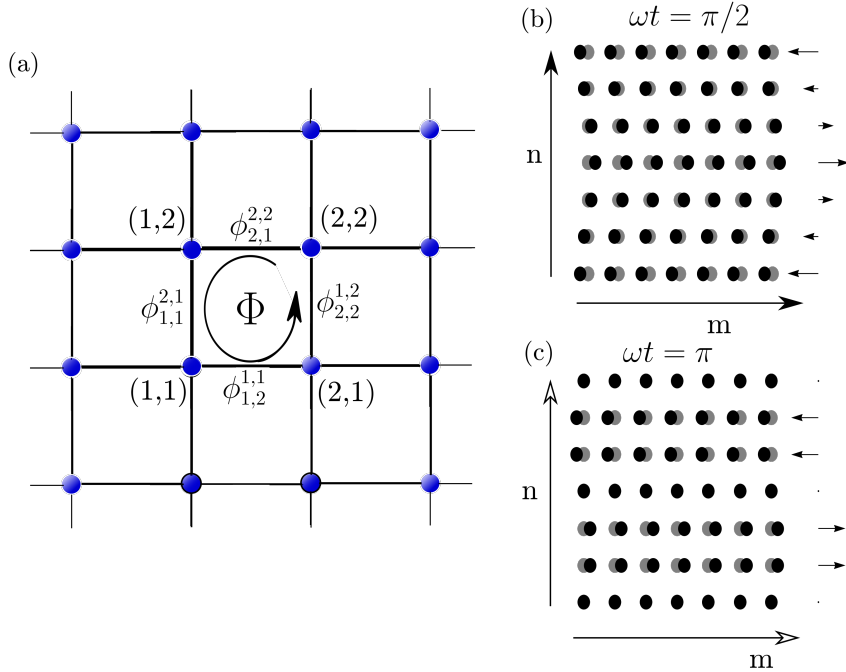


Figure 4.1: (a) Schematic drawing of a 2D lattice with complex tunnelling amplitudes. An electron that tunnels around the borders of one plaquette picks up a phase, $\Phi = \phi_{1,2}^{1,1} + \phi_{2,2}^{1,2} + \phi_{2,1}^{2,2} + \phi_{1,1}^{2,1}$, due to the presence of the vector potential \mathbf{A} . (b)-(c) show two different snapshots of a sinusoidally shaken square lattice where the initial phase of modulation depends on the row index n . The light gray squares show the position of an undriven square lattice and the arrows show the direction and magnitude of the displacement of that row compared to the undriven case. Note that the shape of the lattice changes with propagation distance.

moving in a square lattice subject to a static plus sinusoidally varying electric fields which are polarised in the x-direction [32]

$$\hat{H}(t) = -\kappa \sum_{m,n} \left[\hat{c}_{m,n}^\dagger \hat{c}_{m+1,n} + \hat{c}_{m,n}^\dagger \hat{c}_{m,n+1} \right] + \text{h.c} + q(E_s + E(t)) \sum_{m,n} x_{m,n} \hat{c}_m^\dagger \hat{c}_m. \quad (4.3)$$

The first bracket describes a single-particle moving in a square lattice. The second term describes the coupling between the particle and the electric field where $qE_s = F$ and $qE(t) = A \sin(\omega t + \phi)$ are the x-polarised static and sinusoidally varying electric fields respectively and $x_{m,n}$ is the x-coordinate of the $(m, n)^{\text{th}}$ lattice site. A new Hamiltonian can be made by making a time-dependent unitary transformation of $\hat{H}(t)$, $\hat{\mathcal{H}}(t) = \hat{R}\hat{H}\hat{R}^\dagger - i\hat{R}\frac{\partial}{\partial t}\hat{R}^\dagger$ [37, 38]. The unitary transformation, \hat{R} , is chosen so that the term $i\hat{R}\frac{\partial}{\partial t}\hat{R}^\dagger$ removes the electric field term from $\hat{H}(t)$. The transformed

Hamiltonian is then given by

$$\hat{\mathcal{H}} = -\kappa \sum_{m,n} \left[e^{ia\left(Ft - \frac{A}{\omega} \cos(\omega t + \phi)\right)} \hat{c}_{m,n}^\dagger \hat{c}_{m+1,n} + \hat{c}_{m,n}^\dagger \hat{c}_{m,n+1} \right] + \text{h.c.} \quad (4.4)$$

where a is the lattice spacing and Hadamard's lemma [104] has been used to treat terms of the form $\hat{R}\hat{c}_{m,n}^\dagger \hat{c}_{m,n}\hat{R}^\dagger$. Importantly, the x-polarised electric field only affects the x-direction hoppings and leaves the y-direction hoppings unaffected. The field strength F is chosen such that $Fa = M\omega$ where M is an integer and we define $A_x = \frac{A}{\omega}a$ to give

$$\hat{\mathcal{H}} = -\kappa \sum_{m,n} \left[e^{i(M\omega t - A_x \cos(\omega t + \phi))} \hat{c}_{m,n}^\dagger \hat{c}_{m+1,n} + \hat{c}_{m,n}^\dagger \hat{c}_{m,n+1} \right] + \text{h.c.} \quad (4.5)$$

4.2.2 Floquet's theorem

The transformed Hamiltonian, Eq. (4.5), is periodic in time with a period given by $T = 2\pi/\omega$. Time-periodic Hamiltonians can be treated using Floquet's theorem [41, 105], which guarantees that solutions of the Schrödinger equation can be written in the form

$$|\psi_\alpha(t)\rangle = e^{-i\epsilon_\alpha t} |\phi_\alpha(t)\rangle \quad \text{with} \quad |\phi_\alpha(t+T)\rangle = |\phi_\alpha(t)\rangle, \quad (4.6)$$

where $|\phi_\alpha(t)\rangle$ and ϵ_α are the Floquet eigenstate and quasi-energy respectively. The name quasi-energy is chosen suggestively because of the close similarity between periodic in time systems and systems which are periodic in space which give rise to quasi-momentum. In close analogy with Bloch's theorem the quasi-energy also has Brillouin zone-like structure in which each unique eigenstate of the time-dependent Schrödinger equation can be represented by a Floquet eigenstate with a quasi-energy within the range $-\omega/2 < \epsilon \leq \omega/2$. In practice this implies that the Floquet states with quasi-energies ϵ_α and $\epsilon_\alpha + q\omega$, where q is an integer, physically represent the same state.

The interest in time-periodic systems is that in the limit of fast driving the evolution of the time-dependent system can be well described by a *static* effective

Hamiltonian. The spectrum of this effective Hamiltonian is given by the quasi-energy and by modifying the driving protocol potentially interesting features that are difficult to generate in static systems can be observed in the quasi-energy. This Floquet engineering approach has allowed the observation of a number of interesting phenomena in both cold-atom experiments [1, 2, 7, 15, 36, 63, 111] and photonics [100]. The time evolution operator describing the dynamics over the time frame $t_i \rightarrow t_f$ can be written as [37]

$$\hat{U}(t_i \rightarrow t_f) = e^{-i\hat{K}(t_f)} e^{-i(t_f - t_i)\hat{H}_{\text{eff}}} e^{i\hat{K}(t_i)}. \quad (4.7)$$

The time independent effective Hamiltonian, \hat{H}_{eff} describes the system stroboscopically, i.e. at integer multiples of T , whilst $\hat{K}(t)$ is the micro-motion operator which describes the dynamics that take place within each period of the driving. In the limit of high-frequency driving, as the period is small, the observables are generally only slightly affected by the micro-motion and the dynamics are well captured by the effective Hamiltonian. In this fast driving regime the effective Hamiltonian and the kick operators can be derived perturbatively in powers of $1/\omega$. Expanding the time dependent Hamiltonian in Fourier components as $\hat{\mathcal{H}}(t) = \sum_{j=-\infty}^{\infty} \mathcal{H}^{(j)} e^{ij\omega t}$ the effective Hamiltonian to first order can be written as [37]

$$\hat{\mathcal{H}}_{\text{eff}} = \mathcal{H}^{(0)} + \frac{1}{\hbar\omega} \sum_{j>0} \frac{1}{j} [\mathcal{H}^{(j)}, \mathcal{H}^{(-j)}] + \mathcal{O}\left(\frac{1}{\omega^2}\right). \quad (4.8)$$

Following this prescription to leading order the transformed Hamiltonian of Eq. (4.5) produces an effective Hamiltonian given by

$$\hat{\mathcal{H}}_{\text{eff}} = -\kappa \sum_{m,n} \left[i^M \mathcal{J}_M(A_x) e^{-iM\phi} \hat{c}_{m,n}^\dagger \hat{c}_{m+1,n} + \hat{c}_{m,n}^\dagger \hat{c}_{m,n+1} \right] + \text{h.c.} \quad (4.9)$$

where \mathcal{J}_M is the M^{th} order Bessel function of the first kind and the Jacobi-Anger expansion,

$\exp(ix \cos(y)) = \sum_{n=-\infty}^{\infty} i^n \mathcal{J}_n(x) e^{iny}$, has been used. The effective Hamiltonian describes a particle hopping in a square lattice but where the x-direction tunnelling

elements are complex with the phase given by the initial phase of the sinusoidal modulation. The generation of these complex tunnelling elements resembles the Peierls phase needed to generate a magnetic flux. Unfortunately, as it stands this technique can not be used to produce a magnetic flux as there is no spatial dependence to the phases and so adding the complex phases around an elementary plaquette gives zero and hence no magnetic flux. In the next section the photonic analogue of the technique is discussed and this analysis suggests a mechanism by which a spatial dependence can be imparted to the phases.

4.2.3 Complex tunnelings in a photonic lattice

In this section the photonic analogue of photon-assisted tunneling is discussed and in particular how an electric field can be simulated. It will be shown that curving the waveguides along the propagation direction, z , allows the simulation of arbitrary time dependent electric fields by an appropriate choice of bending profile. The starting point is the paraxial equation

$$i\lambda \frac{\partial \psi(x, y, z)}{\partial z} = -\frac{\lambda^2}{2n_s} \nabla_{\perp}^2 \psi(x, y, z) + V(x - x_0(z), y - y_0(z))\psi(x, y, z) \quad (4.10)$$

where $V(x, y) = -\Delta n(x, y)$ is the effective refractive index profile of the waveguide array and $x_0(z)$ and $y_0(z)$ describe the bending profiles of the waveguide arrays along the propagation direction in the x and y directions respectively. It is important to note that all the waveguides are moving identically and so this kind of movement will be referred to as homogeneous bending. The fact that the array moves as a whole means it is possible to transform to the frame moving with the array. The waveguides appear straight in this moving frame and the effect of the bending manifests in the addition of a new term in the paraxial equation. This can be seen by using the Kramers-Henneberger transformation [54, 83] which introduces the new variables $x' = x - x_0(z)$, $y' = y - y_0(z)$, $z' = z$ and $\Phi(x', y', z') = \psi(x', y', z')\exp[-i(n_s/\lambda)\dot{x}_0x' -$

$in_s/(2\lambda) \int_0^{z'} \dot{x}_0^2(\alpha) d\alpha$. The transformed paraxial equation becomes

$$i\lambda \frac{\partial \Phi(x', y', z')}{\partial z'} = \left[-\frac{\lambda^2}{2n_s} \nabla_{\perp}^2 + V(x', y') \right] \Phi(x', y', z') + n_s [x' \ddot{x}_0(z') + y' \ddot{y}_0(z')] \Phi(x', y', z')$$
(4.11)

The transformed paraxial equation is analogous to the Schrödinger equation of a particle of charge q moving in a *static* potential whilst subject to a electric field given by $\mathbf{E}(z') = E_x \hat{x} + E_y \hat{y}$. The field components are given by $qE_x(z') = -n_s \ddot{x}_0(z')$ and $qE_y(z') = -n_s \ddot{y}_0(z')$ respectively. The simulated electric field is therefore determined by the bending profile and so in order to construct the necessary fields for photon-assisted tunnelling a bending profile such as $x_0(z) = Fz^2 + A \sin(\omega z + \phi)$ should be used. Applying a tight-binding analysis to Eq. (4.11) results in a Hamiltonian of exactly the form described by Eq. (4.3) and so the analysis conducted in sections 4.2.1 and 4.2.2 can be straightforwardly applied. Consequently, the combination of periodic bending and constant curving of a waveguide array mimics a static+AC electric field and so allows the creation of complex tunnelling elements by utilising a photonic analogue of photon-assisted tunnelling.

4.2.4 Inhomogenous bending

The analysis conducted in the previous section applied to homogeneously curving waveguide arrays, however, one of the key advantages of laser written waveguides arrays is that the position of each waveguide can be individually controlled. Importantly, this ability allows for the creation of inhomogeneously bent lattices where the bending profile varies from waveguide to waveguide. For illustration consider a square lattice where the waveguides are labelled by their row and column indices. The bending profile of the $(m, n)^{th}$ waveguide is given by $x_{m,n}(z) = Fz^2 + A \sin(\omega z + \phi_n)$ which is composed of two parts: the first term is waveguide independent and can be recognised from the previous section as being analogous to a static electric field. The second term describes sinusoidal bending but where the initial phase of the modulation depends on the row number of the lattice. In the

effective Hamiltonian of Eq. (4.9) the phase of the tunnellings in the x-direction depended on the initial phase of the sinusoidal modulation. Therefore, intuitively one might expect that if different rows of the square lattice had different initial phases, fig. 4.1(b-c), this would introduce a position dependence to the phase of the x-tunnellings which if properly tailored could give rise to a non-zero magnetic flux. The presence of inhomogeneous shaking does imply, however, that some waveguide separations will be changing along the propagation direction. In the next section, it will be however shown that this has little effect and that the intuitive picture holds.

4.3 An artificial magnetic field

The starting point for the derivation is the paraxial equation

$$i\lambda \frac{\partial E}{\partial z} = -\frac{\lambda^2}{2n_s} \left(\frac{\partial^2 E}{\partial x^2} + \frac{\partial^2 E}{\partial y^2} \right) + V[x, y, z]E \quad (4.12)$$

where $\lambda = \lambda/(2\pi)$, n_s is the refractive index of the glass and the function $V[x, y, z]$ describes how the refractive index modulation in the transverse direction varies along the propagation direction. For the purposes of this chapter we choose $V[x, y, z]$ to only have inhomogeneous bending in the x-direction

$$V[x, y, z] = \sum_{m,n} V_0[x - x_{m,n}^0 - x_0(z) - x_{m,n}(z), y - y_{m,n}^0 - y_0(z)]. \quad (4.13)$$

Here $V_0(x, y)$ is the refractive index profile of a single waveguide, $(x_{m,n}^0, y_{m,n}^0)$ is the static waveguide position in the absence of any bending and the integers (m, n) label the waveguide. The functions $x_0(z)$ and $y_0(z)$ describe homogeneous curving of the lattice in the x - and y -directions respectively. The function $x_{m,n}(z)$ describes the inhomogeneous movement of the $(m, n)^{th}$ waveguide. In a lattice with inhomogeneous movement it is not possible to transform to a moving frame where all the waveguides appear stationary and therefore the Kramers-Henneberger transformation can no longer be used and a different approach must be used. In this work we generalise the approach used in ref. [34], which was used to treat homogeneous bending, to

analyse inhomogeneously bending waveguides. This approach involves applying a tight-binding analysis where the field is represented as a sum of individual waveguide modes

$$\begin{aligned}
 E[x, y, z] &= \sum_{m,n} c_{m,n} u_{m,n} e^{i\gamma_{m,n}} \\
 &= \sum_{m,n} c_{m,n}(z) u[x - x_{m,n}^0 - x_0 - \tilde{x}_{m,n}, y - y_{m,n}^0 - y_0] \\
 &\quad \exp[2ip(\dot{x}_0 + \dot{\tilde{x}}_{m,n})(x - x_{m,n}^0 - x_0 - \tilde{x}_{m,n}) + ip \int_0^z (\dot{x}_0(\alpha) + \dot{x}_{m,n}(\alpha))^2 d\alpha] \\
 &\quad \exp[2ip\dot{y}_0(y - y_{m,n}^0 - y_0) + ip \int_0^z \dot{y}_0(\alpha)^2 d\alpha + i\frac{\beta}{\lambda}z], \quad (4.14)
 \end{aligned}$$

where $p = n_s/(2\lambda)$ and $u[x, y]$ satisfies the equation

$$-\beta u[x, y] = -\frac{\lambda^2}{2n_s} \left(\frac{\partial^2}{\partial x^2} + \frac{\partial^2}{\partial y^2} \right) u[x, y] + V_0[x, y] u[x, y]. \quad (4.15)$$

Inserting the expansion of Eq. (4.14) into Eq. (4.12) gives

$$\begin{aligned}
 0 &= \sum_{m,n} e^{i\gamma_{m,n}} \left[-i\lambda u_{m,n} \dot{c}_{m,n} + c_{m,n} u_{m,n} (V[x, y, z] - V_0^{m,n}) \right. \\
 &\quad \left. + c_{m,n} \left(n_s (x - x_{m,n}^0 - x_0 - \tilde{x}_{m,n}) (\ddot{x}_0 + \ddot{\tilde{x}}_{m,n}) + n_s (y - y_{m,n}^0 - y_0) \ddot{y}_0 \right) \right] \quad (4.16)
 \end{aligned}$$

where Eq. (4.15) has been used. Multiplying by $u_{a,b} e^{-i\gamma_{a,b}}$ and integrating transversely gives the coupled mode equations

$$i \sum_{m,n} \dot{c}_{m,n} p_{a,m}^{b,n} = - \sum_{m,n} \left(t_{a,m}^{b,n} + e_{a,m}^{b,n} \right) c_{m,n} \quad (4.17)$$

where p , t and e represent overlap integrals of the form

$$\begin{aligned}
 p_{a,m}^{b,n} &= \frac{1}{N} \int dx dy e^{i(\gamma_{m,n} - \gamma_{a,b})} u_{a,b} u_{m,n}, \\
 t_{a,m}^{b,n} &= \frac{1}{N\lambda} \int dx dy e^{i(\gamma_{m,n} - \gamma_{a,b})} u_{a,b} u_{m,n} (V[x, y] - V_0^{m,n}), \\
 e_{a,m}^{b,n} &= \frac{n_s}{N\lambda} \left[(\ddot{x}_0 + \ddot{x}_{m,n}) \int dx dy \left(e^{i(\gamma_{m,n} - \gamma_{a,b})} u_{a,b} u_{m,n} \right. \right. \\
 &\quad \left. \left. (x - x_{m,n}^0 - x_0(z) - x_{m,n}(z)) \right) \right. \\
 &\quad \left. + \ddot{y}_0 \int dx dy e^{i(\gamma_{m,n} - \gamma_{a,b})} u_{a,b} u_{m,n} (y - y_{m,n}^0 - y_0(z)) \right], \\
 N &= \int dx dy u_{m,n} u_{m,n}.
 \end{aligned} \tag{4.18}$$

The diagonal p integrals, those with $a = m$ and $b = n$, are equal to 1 by the normalisation convention chosen while the diagonal e integrals are 0 by symmetry. The off-diagonal p and e integrals are also present in the tight-binding analysis of a homogeneously bent waveguide array and are negligible as long as the waveguide separation remains large compared to the dimensions of the waveguide mode [90]. In the inhomogeneously bending square lattice the waveguide separations are always bigger than or equal to a , the lattice constant of a static square lattice, and so these terms may be safely neglected.

The effect of the bending is therefore encoded in the z dependent modification of the tunnelling elements $t_{m,a}^{n,b}$. In this work we will focus on the square lattice geometry with nearest neighbour tunnellings only and use the bending profiles given by

$$\begin{aligned}
 y_0(z) &= B \sin(\omega z), \\
 x_0(z) &= F z^2 = \frac{\omega}{4pa} z^2, \\
 x_{m,n}(z) &= x_n(z) = A \sin(\omega z + \phi_n)
 \end{aligned} \tag{4.19}$$

where n refers to the row number of the lattice, see fig. 4.1(b-c). It is shown in the appendix that for realistic experimental parameters the coupled-mode equations are

given by

$$i \frac{dc_{m,n}}{dz} = - \left(t_x^n c_{m+1,n} + (t_x^n)^* c_{m-1,n} + t_y^{n,n+1} c_{m,n+1} + (t_y^{n-1,n})^* c_{m,n-1} \right) \quad (4.20)$$

where

$$t_x^n = \exp[iK_x \cos(\omega z + \phi_n) + i\omega z] C_0, \quad (4.21)$$

$$t_y^{n,n+1} = \exp[iK_y \cos(\omega z) + i \frac{2A}{a} \sin(\frac{\phi_{n+1} - \phi_n}{2}) \sin(\omega z + \frac{\phi_n + \phi_{n+1}}{2})] C_{n,n+1}(z). \quad (4.22)$$

Here $K_x(K_y) = 2p\omega a A(B)$ and C_0 is the tunnelling constant between static waveguides separated by the lattice constant a . $C_{n,n+1}(z)$ describes how the magnitude of the y-direction tunnellings changes along the propagation direction. In the presence of inhomogeneous shaking in the x-direction the waveguide separations between waveguides in different rows of the square lattice are changing along the propagation direction. Assuming the coupling is exponentially dependent upon the waveguide separation this z-dependent modification is described by the term $C_{n,n+1}(z) = \kappa_0 \exp[-d_{n,n+1}(z)/\tau]$. Here $d_{n,n+1}(z) = \sqrt{a^2 + (A \sin(\omega z + \phi_n) - A \sin(\omega z + \phi_{n+1}))^2}$ is the distance between waveguides in neighbouring rows and κ_0 and τ are material dependent coefficients.

The salient point about the coupled mode equations, Eq. (4.20)-(4.22), is that they are periodic in z and so are amenable to the Floquet formalism discussed in the previous sections. To leading order the z -independent effective coupled-mode equations are given by

$$i \frac{dc_{m,n}}{dz} = - \left(t_x e^{-i\phi_n} c_{m+1,n} + t_x^* e^{i\phi_n} c_{m-1,n} + t_y^n c_{m,n+1} + t_y^{n-1} c_{m,n-1} \right), \quad (4.23)$$

where the effective couplings have the form

$$\begin{aligned}\frac{t_x^n}{C_0} &= \mathcal{J}_1(K_x)e^{i\pi/2}, \\ \frac{t_y^n}{C_0} &= \exp\left[-\frac{A^2}{\tau a} \sin^2\left(\frac{\phi_{n+1} - \phi_n}{2}\right)\right] \mathcal{J}_0\left(\sqrt{K_y^2 + P^2 + 2K_y P \sin(\gamma_n)}\right)\end{aligned}\quad (4.24)$$

with

$$\begin{aligned}P &= \frac{2A}{a} \sin\left(\frac{\phi_{n+1} - \phi_n}{2}\right), \\ \gamma_n &= \frac{1}{2}(\phi_{n+1} + \phi_n), \\ K_{x,(y)} &= 2p\omega a A(B)\end{aligned}$$

Here C_0 is the coupling between two static waveguides and \mathcal{J}_n is the n^{th} order Bessel function of the first kind. The effective coupled mode equations, Eq. (4.23), have x-direction couplings that feature a site dependent phase that can be interpreted as a Peierls phase. Summing these phases around a single square plaquette gives a non-zero result of $\phi_{n+1} - \phi_n$. Thereby, these effective equations model the dynamics of a single-particle moving in a lattice subject to a magnetic field. It should be emphasised that this technique allows the strength and shape of the magnetic field to be engineered by control of the ϕ_n 's. Therefore, inhomogeneously shaken photonic lattices provide a highly controllable platform to allow the study of a whole range of different systems like uniform magnetic fields, staggered magnetic fields and even inhomogeneous structures such as barriers. Note that in order to realise a uniform flux of Φ the initial phases of modulation should be chosen as $\phi_n = n\Phi$.

4.4 Application

4.4.1 Single plaquette

To demonstrate the validity of this procedure in generating an artificial magnetic field we begin by considering the simplest possible structure namely a single square

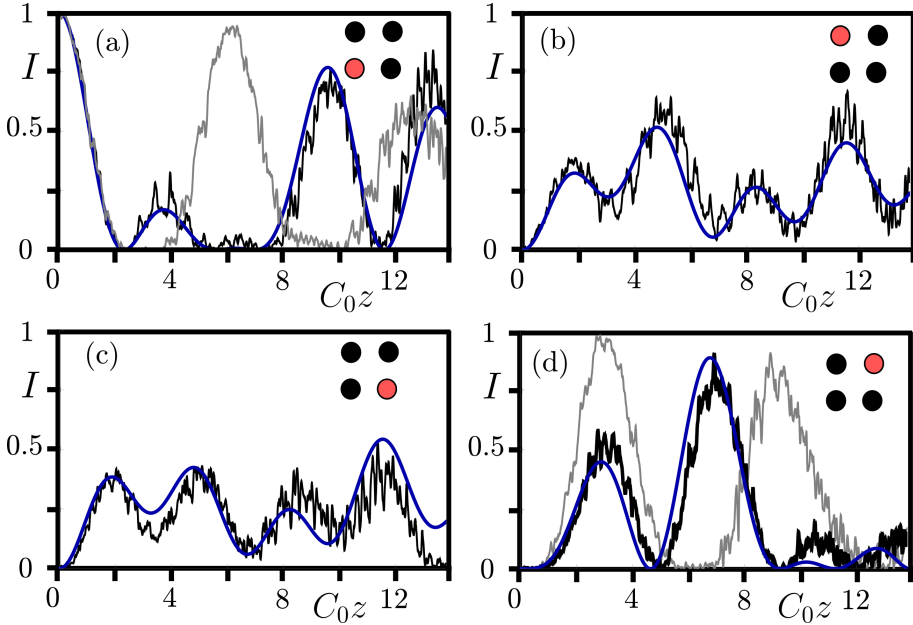


Figure 4.2: Figure comparing the results from the effective coupled-mode theory, blue curve, and a split step simulation of the paraxial equation, black curve, for an inhomogenously shaken four waveguide plaquette. The curves show how the intensity in the pink highlighted waveguide changes along the propagation direction. The lower two waveguides are shaken with a phase $\phi_0 = 0$ whilst the upper two waveguides have a initial phase of $\phi_1 = \pi/2$ which should correspond to a flux of $\frac{\pi}{2}$ piercing the plaquette. The light gray curves in (a) and (d) show paraxial simulation results for a homogeneously shaken plaquette and show significant difference. The light gray curves are omitted from figures (b) and (d) for clarity.

plaquette consisting of four waveguides, see black discs in fig. 4.2. The accuracy of the effective coupled mode equations can be tested by comparing their predictions to those coming from a split-step solution [75] of the paraxial equation, Eq. (4.12). The waveguides were chosen to possess Gaussian refractive index profiles, $\Delta e^{-\frac{r^2}{\rho^2}}$ with Δ and ρ chosen to be 6.9×10^{-4} and $\rho = 5 \mu m$ respectively [107, 115]. The wavelength of the incident light is chosen to be $700 nm$. The particular bending profiles that are used in the simulation are chosen as $x_n(z) = A \sin(\omega z + \phi_n)$ and $y(z) = B \sin(\omega z)$ with $A = 5.5 \mu m$, $B = 6.5 \mu m$ and the driving frequency is chosen to be $\omega \approx 11C_0$. The shaking amplitudes are chosen so that the magnitude of the x and y couplings are approximately equal. The magnitude of the nearest neighbour couplings used in this coupled mode analysis are extracted by simulating within the paraxial equation two shaken waveguides. The phases are chosen as $\phi_0 = 0$ for the $y = 0$ waveguides and $\phi_1 = \pi/2$ for the $y = a = 20 \mu m$ waveguides. The figures show the evolution of the intensity in each of the four waveguides as a function of the

propagation distance z . The blue lines in each figure indicate the results predicted by the coupled-mode equations. The all-important phases of the nearest neighbour couplings are obtained using the predictions of Eq. (4.20)-(4.22). The effective coupled mode equations very accurately capture the evolution of the intensity over long propagation distances and the results differ dramatically from what is expected in the homogeneous bending case, light gray curve.

4.4.2 Square lattice

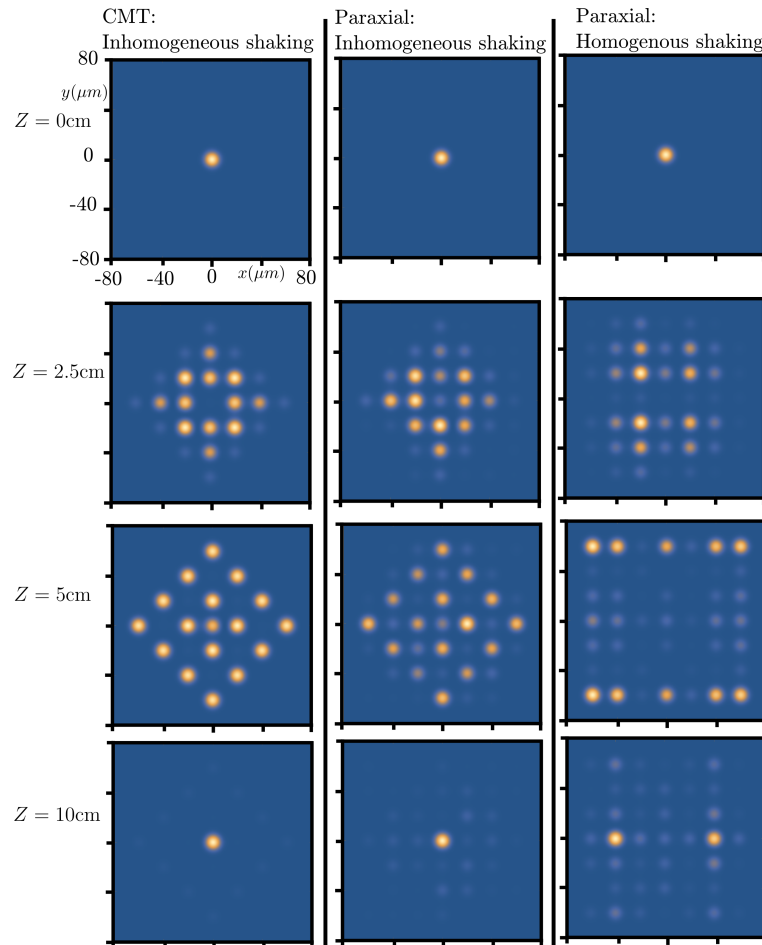


Figure 4.3: Figure comparing the output facet images generated by the Hofstadter model of Eq. (4.23), left-hand images, and a split-step solution of the paraxial equation with inhomogeneous and homogeneous shaking profiles. The agreement between the Hofstadter model and the inhomogeneously shaken lattice is excellent indicating that the inhomogeneous shaking of a waveguide array is an excellent way of emulating the Hofstadter Hamiltonian.

A straightforward extension of the plaquette studied in the previous section can be used to generate a flux ladder which could be experimentally probed [7, 61, 91]. In the remainder of this section however, the work will focus on the generation of

a uniform flux in a square lattice geometry. The tight-binding model describing the dynamics is called the Hofstadter-Harper model and, as previously discussed, features a rich variety of physical phenomena such as non-trivial topological indices and the famous Hofstadter butterfly.

In principle the same x and y shaking profiles that were used for the single plaquette could be used to generate a flux in the square lattice. These parameters, however, give rise to an inhomogeneous coupling rate in the y direction. The origin of this inhomogeneity is the $2K_y P \sin(\gamma_n)$ term in the argument of the Bessel function in Eq. (4.22). For instance, in the case of generating a uniform flux of Φ the shaking phases are chosen as $\phi_n = n\Phi$ and it is easily checked that the $\sin(\gamma_n)$ term can change value and sign depending upon the value of n leading to local modifications of the effective y tunnelling. Importantly, these local modifications are present only if there is shaking in the y direction, i.e. non-zero K_y . However, without any y -direction shaking the effective equations will be anisotropic with the y tunnellings significantly larger than the x -couplings. A potential method for dealing with this anisotropy is to deform the square lattice so that the lattice constant in the y -direction is larger than in the x -direction. This has the effect of decreasing the static coupling constant in the y -direction. The difference between the x and y lattice constants can then be tuned so as to allow for the magnitude of the x and y couplings to become equal. The simulation parameters were chosen to be $x_n(z) = A \sin(\omega z + n\pi/2)$ with $A = 5.5\mu m$, $y_0(z) = 0$ whilst the x and y lattice constants were chosen to be $a_x = 20\mu m$ and $a_y = 22\mu m$ respectively. These lattice constants were found by simulating a series of inhomogeneously shaken two waveguide couplers with different lattice constants and finding the parameter that gave roughly equal tunnellings in the x and y directions. The effective coupled mode equations for these particular bending profiles can then be written as:

$$i \frac{dc_{m,n}}{dz} = - \left(C_x e^{-in\pi/2} c_{m+1,n} + C_x^* e^{in\pi/2} c_{m-1,n} + C_y c_{m,n+1} + C_y^* c_{m,n-1} \right) \quad (4.25)$$

with $|C_y| = |C_x|$ which corresponds to the simulation of an isotropic Hofstadter model subject to a flux of $\pi/2$. Fig. 4.3 shows a comparison of the output facet

images obtained from the coupled mode equations, left-hand images, and the simulation of the paraxial equation, middle images, for a range of different propagation distances when the central site of a 7×7 lattice is excited at the input. The right hand images show paraxial results for a homogeneously shaken lattice, i.e a flux free lattice, and the output images show a clear difference. The close agreement between the coupled mode theory and the paraxial solution demonstrates that the effective equations are accurately capturing the complicated dynamics that occur over long propagation length scales. The close agreement between theory and simulation for both the plaquette and lattice geometries indicates that inhomogeneous bending is an effective mechanism for generating an artificial magnetic flux.

4.5 Chapter summary

In this chapter we have, through theory and simulation, demonstrated how periodic inhomogeneous curving of a waveguide array can be used to simulate the dynamics of a particle subject to a magnetic field. In the regime where the frequency of the periodic curving is much larger than any of the native couplings present a set of coupled-mode equations are obtained that link the strength and shape of the magnetic field to the initial phase of the inhomogeneous modulation. The excellent control over waveguide placement that is allowed in photonic lattices allows this initial phase to be easily tuned. This flexibility will enable these lattices to serve as powerful laboratory to study particle dynamics in strong, weak and even inhomogeneous magnetic fields.

Chapter 5

Observation of anomalous topological edge modes

5.1 Introduction

The discovery of the quantized Hall effect [67], and its subsequent topological explanation, demonstrated the important role topology can play in determining the properties of quantum systems [50, 98, 119]. At a stroke this discovery showed that not only were existing band theories incomplete but also that there existed a new class of materials, the topological insulators, that was heretofore unexplored. The conduction properties of these materials proved quite remarkable and consist of an insulating bulk and conducting edges states that chirally propagate around the surface without back-scattering on defects. The existence of these edge states and their remarkable robustness against disorder are both vivid demonstrations of the important role topology can play in determining material properties. The desire to explain the origin of these effects led to the development of topological band theory, where, in addition to band index and quasimomentum, Bloch bands are also characterised by a set of topological invariants [10]. An important example of one such invariant is the Chern number, \mathcal{C}_n , where n labels the Bloch band. The values of these Chern numbers can be used to infer physical properties about the system; the most famous example of this is the bulk-edge correspondence which states that \mathcal{C}_n is equal to the difference between the number of chiral edge modes

in the bandgaps above and below the n^{th} band [51, 52, 97]. In order to illustrate some of these ideas fig. 5.1(a) sketches the energy spectrum for a 2D topological insulator where the Bloch bands have non-zero Chern numbers. The material is translationally invariant in the x -direction but finite in the y -direction as shown in fig. (b). The shaded grey regions in (a) show the Bloch bands whilst the coloured lines show the energy dispersions of the topological edge modes. The edge states are localised on one side of the sample with the blue and red modes being confined to the bottom and top edges respectively. The edge modes possess almost linearly dispersing spectra which implies that a wavepacket composed of these edge modes will propagate with an almost constant velocity along the edges as shown in fig. (b). It is important to note that there are no left(right) propagating edge modes on the bottom(top) edge. This is at the heart of the observed robustness of these topological modes as a wavepacket composed of these edge modes encountering a defect cannot backscatter due to the absence of any counter-propagating states at the same energy.

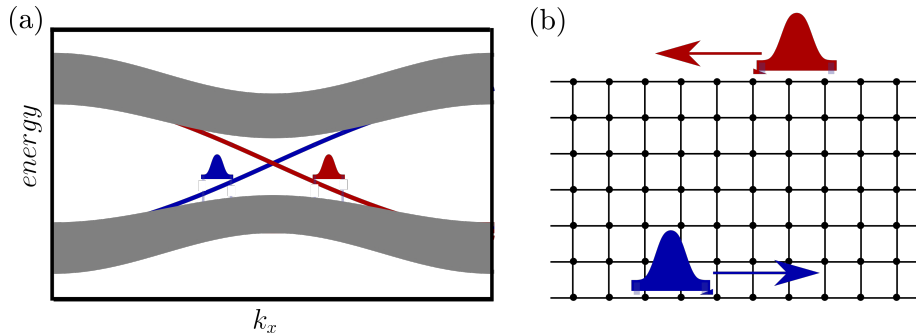


Figure 5.1: (a) Sketch illustrating the energy spectrum of a topological(Chern) insulator in a strip geometry that is periodic in the x -direction but finite in the y -direction. The red and blue lines correspond to edge modes that are localised on the top and bottom edges of the sample respectively. The almost linear nature of these dispersions implies a wavepacket composed of these edge modes will propagate along the edge as shown in (b).

The topological band theory for describing static systems can be readily extended to periodically driven system by exploiting the analogy between the energy spectrum of a static system and the quasi-energy spectrum of a time-periodic system, see chapter 4 for a discussion of Floquet's theorem, quasi-energy and effective Hamiltonians. The quasi-energy spectrum can host Bloch bands which can be assigned the

topological invariants that are used to describe static systems. In the limit of fast driving, driving frequency \gg hopping amplitude, the topological phase of a system can be predicted by the Chern numbers that are used to describe static systems. However, in the limit of slow driving, driving frequency \approx hopping amplitude, robust chiral edge modes can still be observed even if the Chern numbers associated with all the bulk bands are zero. These so called anomalous topological edge modes have no static analogue, and are associated with a distinct topological invariant, which takes into account the full time-evolution over a driving period. This intriguing regime of periodically-driven systems has been investigated in a diverse range of experimental platforms including a photonic setup realising a discrete time quantum walk [66], a designer surface plasmon platform [33] and a one-dimensional microwave network [57]. In this chapter we demonstrate the experimental observation of such anomalous topological edge modes in an ultrafast-laser-inscribed photonic lattice. See ref. [84] for similar experimental results.

5.1.1 Floquet engineering

Subjecting a system to time-periodic driving has proven a powerful method to engineer band structures with non-trivial topological properties [14, 37, 53, 65, 76, 108], as recently demonstrated in cold-atom experiments [2, 36, 63] and photonics [100]. The evolution of a driven system over an arbitrarily long duration $\Delta_t = t_f - t_i$ can be described by the time evolution operator which takes the form [37, 99]

$$\hat{U}(t_i \rightarrow t_f) = e^{-i\hat{K}(t_f)} e^{-i(t_f - t_i)\hat{H}_{\text{eff}}} e^{i\hat{K}(t_i)} \quad (5.1)$$

The time-independent effective Hamiltonian, \hat{H}_{eff} , describes the system stroboscopically, i.e. at integer multiples of T , whilst $\hat{K}(t)$ is the micro-motion operator which describes the dynamics that take place within each period of the driving. In the high-frequency limit the time-independent effective Hamiltonian accurately captures the dynamics and the micro-motion operators have little effect. The topological invariants used to describe static systems therefore accurately describe these high-frequency driven systems. In the slow-driving case, where driving

frequency~hopping amplitudes, the micro-motion operators can no longer be neglected and what happens during the driving period can strongly effect the topology of the system. In this regime the topological invariants used to describe static systems are no longer adequate as situations can arise where all the standard topological invariants are zero but topologically protected edge modes can still arise. In these slowly-driven systems a new topological invariant is introduced called the winding number, W , that takes into account the micro-motion.

The failure of the standard topological invariants in describing slowly-driven systems can be traced to a breakdown in the analogy between the energy spectrum of a static system and the quasi-energy spectrum of a periodically driven system. Recalling, the discussion from chapter 4 the quasi-energy, ϵ , is only defined in the fundamental quasi-energy zone $-\omega/2 < \epsilon \leq \omega/2$ which implies that for slow-driving, small ω , the Bloch bands can start to reach the edges of this fundamental zone. In particular, this means that in addition to the usual bandgap closings that occur in static systems there is also the possibility of a bandgap closing between the highest- and lowest-lying energy Bloch bands through the edge of the fundamental quasi-energy zone. The existence of these two distinct types of bandgap closing has important consequences for the topology of a driven system.

The presence of degeneracies between Bloch bands is crucial in determining the topological properties of the system. Firstly, the topological invariants of a band can only change at a bandgap closing and secondly, the number of topological edge modes in a given bandgap can only change if that bandgap closes. In a driven system the combination of these facts and the presence of zone-edge gap closings can allow the Chern numbers of the bands to change without any of the inter-zone gaps closing. Consequently, it is possible for situations to arise where all the Bloch bands have zero Chern number but yet robust chiral edge modes are still observed, see fig. 5.4 for an illustration. These so-called anomalous topological edge modes are unique to driven systems and have no static analogue.

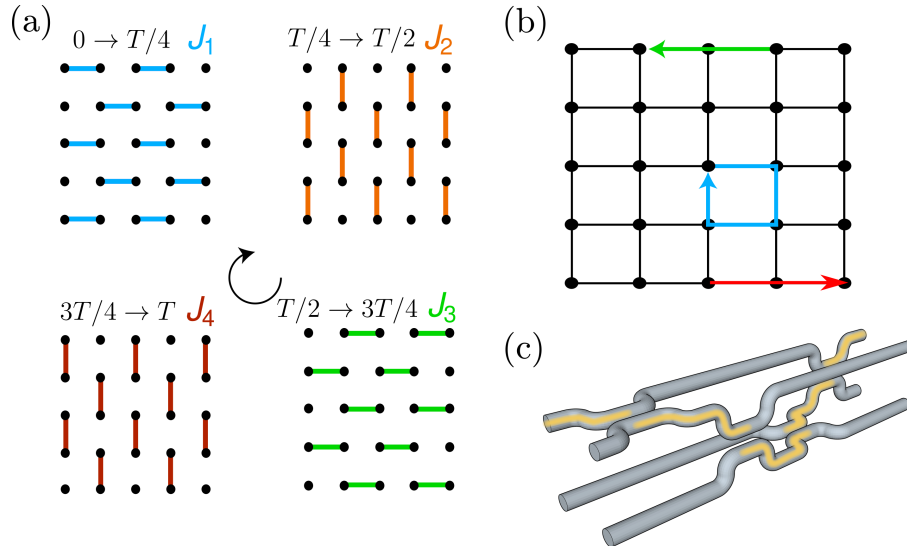


Figure 5.2: (a) illustrates the slowly-driven square lattice. The four different bonds present in the lattice (with coupling constants $J_{1,2,3,4}$) and the cyclic driving protocol employed. (b) In the simplest case where all bond strengths are equal, $JT/4 = \pi/2$, chiral edge modes arise whilst the evolution operator associated with the bulk is identity. (d) illustrating how, using laser inscription, different pairs of waveguides can be moved together to turn on a coupling and then apart to switch it off. This flexibility allows for a realisation of the driving protocol shown in (a). In waveguide arrays the propagation direction z plays a role analogous to time.

5.1.2 Anomalous topological edge modes

The theory works in refs [65, 102] introduced conceptually simple models that exhibited such anomalous topological edge modes. The model presented in ref. [102] is perhaps the simplest and consists of a square lattice with nearest-neighbour couplings, which are designed so that the couplings between a lattice site and its four nearest neighbours are independently controllable. These four couplings, denoted J_1 through J_4 , are then varied in a spatially homogeneous and time-periodic manner so that any lattice site is, at any given moment, coupled to only one of its nearest neighbours, see fig. 5.2(a). The simplest demonstration of this model is when the driving period T is split into four equal steps, and T is selected such that a particle that is initially localised on a certain site will be completely transferred to the neighbouring site after a time $T/4$. Therefore, in a system without any edges, this implies that after one complete period, any initial state is exactly reproduced, which in turn implies that the propagator, $\hat{U}(T)$, is the identity matrix. Consequently, the effective Hamiltonian in Eq. (5.1) is the identity matrix and the quasi-energy spec-

trum consists of two degenerate flat bands. The bulk eigenstates are completely localised, and the Chern numbers associated with the effective Hamiltonian are necessarily zero. In a geometry with edges, however, it is found that there are chiral propagating edge modes that are localised along the edge, see fig. 5.2(b). These occur because a particle launched at an edge cannot return to its initial position and instead move one unit cell along the edge, in direct analogy with the skipped cyclotron orbits of quantum Hall systems.

The adequate topological characterisation of driven systems is captured by a winding number that includes the entire driving period. In particular the winding number accounts for the changes in the Chern numbers that occur through the zone edge within a driving period. In an N -band driven system there can be at most N bandgaps, and for each of these bandgaps, there is a winding number W_m , which has the form [88]

$$W_m = \sum_{n=1}^m \mathcal{C}_n - \sum_i q_i^{ZES}, \quad m = 1, 2, \dots, N \quad (5.2)$$

where \mathcal{C}_n is the Chern number of the n^{th} band at time T . The second term accounts for the changes in Chern number that occur thorough the quasienergy zone edge with q_i^{ZES} corresponding to the the change in Chern number of the lowest band that occurs in the i^{th} zone-edge degeneracy. In direct analogy with static systems this winding number directly gives the number, $n_{edge}(m)$, of topologically protected chiral edge modes present in the m^{th} gap. This driven bulk-edge correspondence can be shown to have the form [88]

$$n_{edge}(m) = W_m = \sum_{n=1}^m \mathcal{C}_n - \sum_i q_i^{ZES} \quad (5.3)$$

The first term on the right hand side of Eq. (5.3) is the term that is found in static systems, whilst the second applies only to driven systems. It is this term that is the source of the anomalous edge modes as it allows the number of edge modes to be non-zero even if the standard topological invariants, i.e. the Chern numbers \mathcal{C}_n , are

zero for all of the bands.

5.2 Slowly-driven square lattice

In this section we consider a driven square lattice which is closely related to the system discussed in the previous section and in ref. [102]. The model introduced in that reference hosts a rich topological phase diagram consisting of both the sought-after anomalous phases as well as more standard phases where the static topological invariants accurately describe the physics. However, in order for all of these different phases to be reached a bipartite sublattice potential must also be included in the driving protocol. In photonic lattices the on-site energies can be controlled by changing the writing speed of the fabricating laser. It is, however, difficult to ascertain the precise relationship between the on-site energy and the write speed. In this section we will show that an equally rich topological phase diagram can instead be created by making the first bond J_1 have a different strength to the following three bonds ($J_{2,3,4} = \tilde{J}$). The considered lattice is the bipartite square lattice shown in fig. 5.2 and in a system without edges the time-dependent Hamiltonian can be written as

$$\hat{H}(t) = \sum_{\mathbf{k}} \begin{pmatrix} \hat{a}_{\mathbf{k}}^\dagger & \hat{b}_{\mathbf{k}}^\dagger \end{pmatrix} \hat{H}(\mathbf{k}, t) \begin{pmatrix} \hat{a}_{\mathbf{k}} \\ \hat{b}_{\mathbf{k}} \end{pmatrix} \quad (5.4)$$

$$\hat{H}(\mathbf{k}, t) = - \sum_{j=1}^{n=4} J_n(t) (e^{i\mathbf{b}_n \cdot \mathbf{k}} \sigma^+ + e^{-i\mathbf{b}_n \cdot \mathbf{k}} \sigma^-) \quad (5.5)$$

where $\hat{a}_{\mathbf{k}}^\dagger$ and $\hat{b}_{\mathbf{k}}^\dagger$ create particles with quasi-momentum \mathbf{k} on the a and b sublattices respectively. The Pauli matrices $\sigma^\pm = \frac{1}{2}(\sigma_x \pm i\sigma_y)$ act in the sublattice space and the vectors \mathbf{b}_i connect nearest-neighbour lattice sites, $\mathbf{b}_1 = -\mathbf{b}_3 = (a, 0)$ and $\mathbf{b}_2 = -\mathbf{b}_4 = (0, a)$. The driving period, T , is split into four equal sections and the parameters $J_n(t)$ control which bond is on during which section, see fig. 5.2(a). The bond strengths, J_1 and $J_{2,3,4} = \tilde{J}$, are chosen so as to satisfy $J_1 T/4 = \Lambda_1$ and $\tilde{J} T/4 = \Lambda_2$. This gives two experimentally controllable parameters that can be

independently tuned. The interplay between these two parameters produces a rich topological phase diagram, see fig. 5.3(a). The different topological phases of this driven two-band system are accurately labelled by the winding numbers associated with the two bandgaps; in the phase diagram shown in fig. 5.3, we have chosen W_1 to be the winding number for the bandgap centred around quasienergy zero and W_2 for the bandgap centred around π/T . The Chern number of the lowest Floquet band, C_1 , is also provided so as to highlight the anomalous regimes where $C_1 = 0$ and $W_{1,2} \neq 0$. In the waveguide realisation of this model, the propagation direction z plays a role analogous to time and the time period T is replaced by the spatial period L .

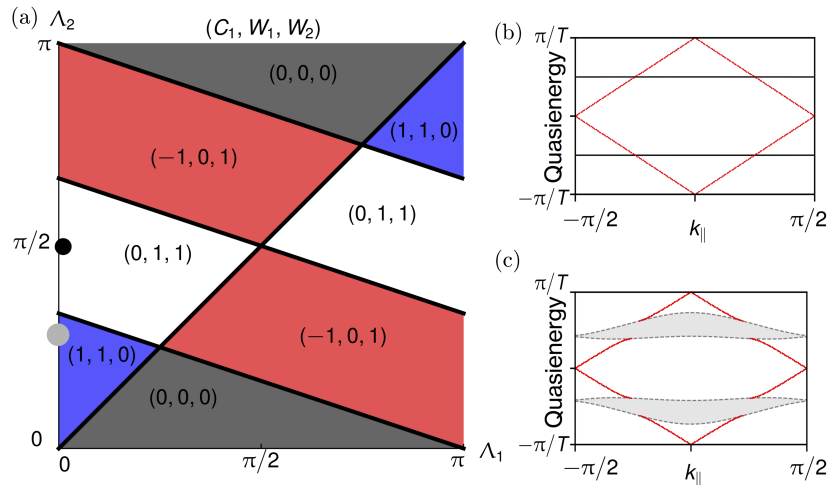


Figure 5.3: Figure (a) shows phase diagram for a generalisation of the model in Fig. 5.2(a), which allows the bond J_1 to be of a different strength to the bonds $J_{2-4} = \tilde{J}$. Here $\Lambda_1 = J_1 T/4$ and $\Lambda_2 = \tilde{J} T/4$. Each phase is described by three topological invariants: the Chern number of the lowest Floquet band C_1 , the winding number W_1 of the gap centred around zero, and the winding number W_2 of the gap centred around π/T . The white regions indicate where anomalous edge modes can be observed. (b) Quasienergy spectrum for the parameters indicated by the black dot in (a). Red curves indicate topological-edge-modes dispersions, while black curves correspond to the bulk bands. (c) Quasienergy spectrum for the experimentally achieved parameters.

The calculation of the phase diagram can be achieved by utilising the property that the topology of the system can only change when there is a gap closing between the two bulk bands. In this model the position of these gap-closing events can be found analytically by diagonalising the evolution operator at the end of the driving period. It is found that for $\Lambda_1 = \Lambda_2$ and $\Lambda_2 = \frac{1}{3}(2\pi - \Lambda_1)$, the system is gapless

at quasienergy zero, while for $\Lambda_2 = \frac{1}{3}(\pi - \Lambda_1)$ and $\Lambda_2 = \frac{1}{3}(3\pi - \Lambda_1)$, the system is gapless through the fundamental zone edge. The position of these gap closings thereby divides the phase space into the eight sectors shown in fig. 5.3(a). The topology within these different sectors can then be defined by calculation of the winding numbers. The calculation of the winding numbers can either be done by utilising the formalism discussed in ref. [88] or by tracking the changes in the Chern number that occur throughout the driving period. The latter method nicely illustrates how zone-edge degeneracies can lead to violations of the standard bulk-edge correspondence and so this approach will be used in this work. For the two-band model discussed above the time evolution operator at time t , where $0 \leq t < T$, may be written as

$$\hat{U}(\mathbf{k}, t) = \sum_{n=1,2} \hat{P}_n(\mathbf{k}, t) e^{-i\phi_n(\mathbf{k}, t)}, \quad (5.6)$$

where $\hat{P}_n(\mathbf{k}, t)$ and $e^{-i\phi_n(\mathbf{k}, t)}$ are the projectors onto the eigenstates and the corresponding eigenvalues of $\hat{U}(\mathbf{k}, t)$ respectively. The instantaneous energies, ϕ_n/T , are constrained to lie in the fundamental quasi-energy zone $[-\pi/T, \pi/T]$. At any time t the evolution operator may be diagonalised to yield the instantaneous Bloch bands of the driven system. The eigenstates associated with these bands can be used to calculate an instantaneous Chern number for that band, see ref. [31] for an efficient technique for calculating the Chern number. Therefore, in accordance with Eq. (5.2), the winding number can then be calculated by tracking changes in the Chern number of the lowest band that occur through the zone edge throughout the driving period. This procedure is illustrated in fig. 5.4 for the parameters $\Lambda_1 = 1$ and $\Lambda_2 = 1.4$, which shows how the instantaneous Chern number of the lowest band changes throughout the driving period. It can be seen that the Chern number changes twice within a driving period and computing the spectra at these times shows that the second of these changes occurs through the zone edge. This latter degeneracy causes the Chern number of the lowest band to decrease by one. This topological transition through the zone edge when combined with the Chern numbers of all the bands being zero at $t = T$ implies, using Eq. (5.2), that both W_1 and W_2 are equal to one.

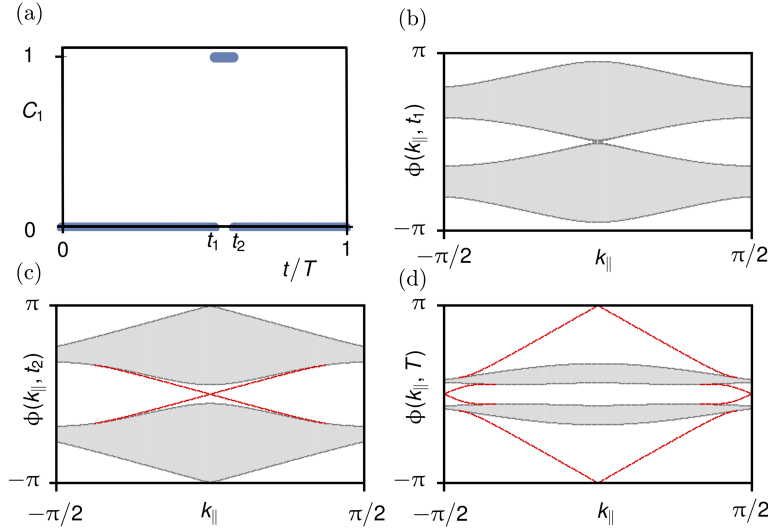


Figure 5.4: Example calculation of the winding number using the evolution of the instantaneous Chern number. (a) shows the evolution of the instantaneous Chern number of the lowest band, C_1 , over one driving period; the system parameters are $\Lambda_1 = 1$ and $\Lambda_2 = 1.4$. The Chern number changes twice within a driving period (at times t_1 and t_2). The first of these topological transitions occurs when the gap closes at $\phi = 0$, (b), whilst the second occurs at $\phi = \pi$, (c). This changing of the instantaneous Chern number that occurs through the zone edge is responsible for the winding numbers W_1 and W_2 being non-zero, and the Chern number of the Floquet bands to be zero. This non-trivial value for the winding number allows for the presence of edge modes in the spectrum at $t = T$, (d), even though the Chern numbers of all the Floquet bands (evaluated at $t = T$) are zero.

5.2.1 Coupling control

The exquisite control over waveguide placement that is allowed in laser-inscribed waveguides allows couplings between waveguides to be switched on and off as required by the driving protocol. The coupling between two waveguides is exponentially dependent upon the separation and so initially a large lattice constant is chosen so that the coupling between all waveguides is negligible. In order to turn on the coupling between two lattice sites the two waveguides are bent together along the propagation direction, as shown in fig. 5.2(c), and the coupling can be switched off by moving the waveguides apart. It can be shown that if the waveguides are synchronously bent together and then apart over a distance $L/4$, and the instantaneous coupling between the waveguides is $\kappa(z)$, then this z dependent coupling can be replaced by an effective coupling of strength $J_{eff} = \frac{4}{L} \int_0^{L/4} dz \kappa(z)$ [58]. The integrand, $\kappa(z)$, depends on the bending profile used and so by appropriately choosing

the shape of the bending the effective coupling can be tailored. In this way an array of synchronously bent waveguides exactly maps onto the driven square lattice that we wish to realise. A point to note is that the shape of the waveguide bending is a fixed parameter once the fabrication laser has finished writing. The coupling, $\kappa(z)$, is, however, also dependent on the wavelength of the input light used in the experiment and the wavelength is tunable in-situ. This offers an additional experimental parameter that allows for the optimisation of the coupling and additionally allows the same sample to be used to explore different topological regimes.

5.3 Experimental realisation

The experimental realisation of anomalous topological edge modes focused on the parameters $\Lambda_1 = 0$ and $\Lambda_2 = \pi/2$, as indicated by the black dot in fig. 5.3(a). In this configuration, the blue bonds in fig. 5.2(a) are never turned on, while nearly complete transfer of light can occur via the other three bonds. These parameters are desirable as not only is the resultant system located well within the anomalous regime but also there are robust chiral edges states that can be excited with unit efficiency, through the simple experimental technique of single-site excitation. Furthermore, for these parameters the bulk bands are energetically well separated which implies that weak disorder cannot close the energy gap and so cannot alter the topology.

The experimental procedure consisted of writing a 8×8 driven square lattice consisting of two driving periods. In addition 5 isolated copies of each of the bonds J_1 through J_4 were written. The isolated bonds were used to determine J_{1-4} as a function of wavelength and thereby find the wavelength where $J_1L/4 = 0$ and $J_2L/4 = J_3L/4 = J_4L/4 = \pi/2$ were best satisfied. The experimental characterisation of these isolated couplers revealed that when 785 nm light was used the mean and standard deviation of the couplings were found to be $J_1T/4 = 0$, $J_2T/4 = \pi/2(1.16 \pm 0.04)$, $J_3T/4 = \pi/2(1.15 \pm 0.04)$ and $J_4T/4 = \pi/2(0.85 \pm 0.03)$. The close proximity of these values to the ideal values discussed previously indicate that anomalous topological edge modes should be observable at 785 nm.

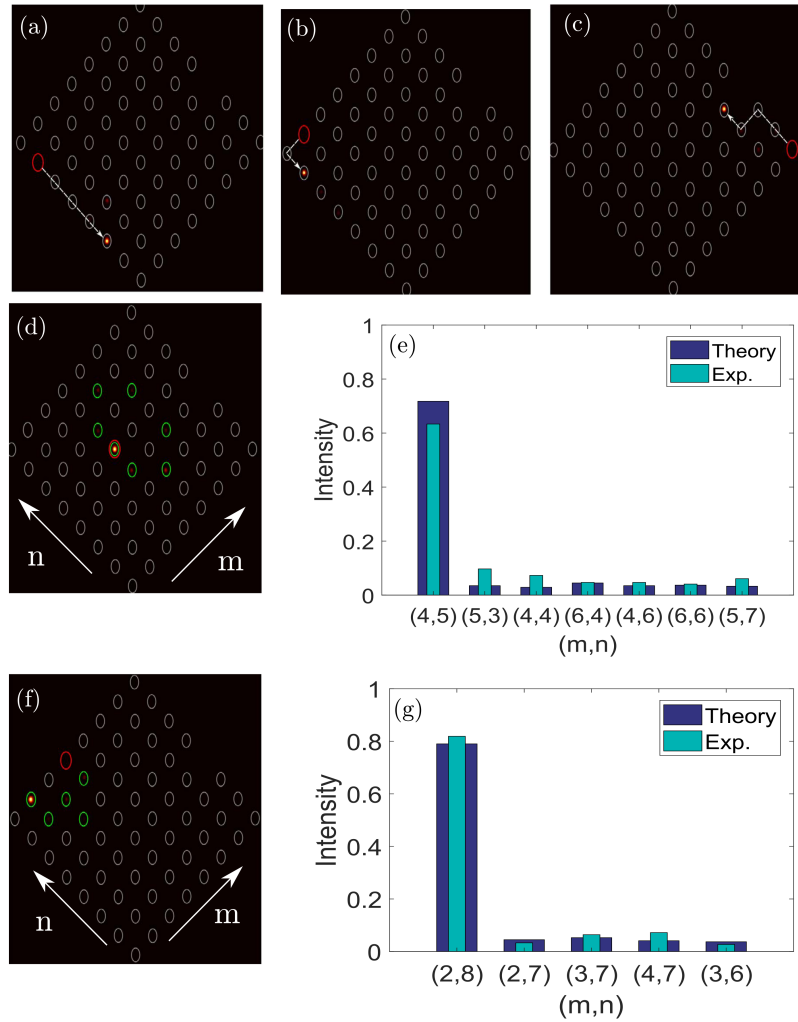


Figure 5.5: Figures (a-d,f) display the experimentally measured output intensity distribution when the light is launched at the lattice site indicated by the red circle. The figures display chiral edge modes (a,f) that are not scattered by corners (b) nor defects (d) as well as a largely localised bulk state (d). Figures (d) and (f) show the experiment output for bulk and edge excitations with the green circles showing the lattice sites at which light was detected at the output. Figures (e) and (g) compare the experimental and theoretical predictions for the green circles shown in (d) and (f). Theoretically these green lattice sites account for > 97% of output intensity. See ref. [84] for a similar experimental work.

To experimentally demonstrate the presence of anomalous topological edge modes, 785nm light was launched at multiple locations around the edge of the lattice; the red circles in fig. 5.5 indicate the launch site. If light is launched at the middle of an edge, as shown in fig. 5.5(a), then at the output it is observed that the light has moved along the edge with minimal penetration into the bulk. The white arrows show the theoretically predicted path of the light. Furthermore, if the input position of the beam is moved further down the edge, (b), the close proximity of

the launch site to the left edge means that the light will encounter the corner of the lattice during its evolution. This corner, as can be observed in the figure, does not cause backscattering but instead the light simply turns the corner and continues to propagate. This robustness is also observed in (c), which demonstrates the light moving around a missing lattice site without backscattering or penetrating into the bulk. These observations provide evidence for the existence of protected chiral edge modes that can be almost exclusively excited by single-site excitation.

The deviation of the couplings J_{2-4} from their ideal values can be observed in the experimental images. The first consequence is that the resultant bulk bands are no longer perfectly flat but now exhibit a finite dispersion, see fig. 5.3(c). The finite width of the bulk bands implies that single site excitation in the bulk shows a small amount of dispersion at the output in contrast to what is expected for perfectly flat bands where the light should completely return to the launch site after two driving periods. The green circles in fig. 5.5(e) indicate at which lattice sites light was detected at the output and fig. (f) compares theoretical and experimental outputs for these green highlighted sites. The second consequence of the couplings deviating from their ideal values is that single site excitation no longer exclusively excites the edge modes but also leads to excitation of the bulk modes. The experimentally measured couplings can be used to calculate that single-site excitation is approximately 75% efficient at exciting edge modes. The remaining 25% are excited bulk modes and this small bulk contribution can be observed in the experimental figures which shows a small amount of the light has penetrated away from the edge and into the bulk, see fig. (g). There is once again close agreement between theory and experimental results, fig. (h).

The central result of the experimental images is that they show the existence of edge modes propagating in a chiral manner, and which are not scattered by corners nor defects. The absence of scattering provides strong evidence that there is topological protection for these edge modes. The experimental bond-strength measurements, combined with the theoretical analysis of the corresponding model, provides strong evidence that these propagating states correspond to anomalous

topological edge modes.

5.4 Experimental disorder

The experimental setup provides the ability to modify in-situ the wavelength of light used as an input. This ability allows the effective coupling between waveguides to be altered without modifying the lattice. The capability of this wavelength-tuning technique allowed for the transfer of the bonds to be changed substantially from $\approx 100\%$ right down to $\approx 50\%$. This wavelength tuning corresponds to moving down the y-axis of the phase diagram from the black dot to the grey dot in fig. 5.3(a). Inspection of the phase diagram shows that this range of parameters should host a topological transition where the Chern number of the two bands become non-zero. Unfortunately, the experimental technique of single-site excitation is not sufficient to resolve this topological transition. In spite of this issue experimental and theoretical predictions can still be compared for a wide range of parameters. In order to perform such a comparison, the coupling strengths extracted from the bond characterisation data were used to calculate a theoretical centre of mass drift, \mathbf{r}_{cm} , that could be compared to experimental results. The centre of mass drift is defined as

$$\mathbf{r}_{cm} = \sum_{m,n} I_{m,n} \mathbf{r}_{m,n} - \mathbf{r}_0 \quad (5.7)$$

where $I_{m,n}$ is the output intensity in the site (m, n) , $\mathbf{r}_{m,n}$ is the spatial coordinate of the site (m, n) , and \mathbf{r}_0 are the coordinates of the launch site. In the experiment, we separately excited the lattice sites of coordinates $(4, 1)$, $(6, 1)$, $(4, 8)$ and $(6, 8)$ and by measuring the output intensity distributions after two driving periods, as a function of the incident-light wavelength, the centre-of-mass drift along the x and y directions could be obtained. These different positions should, in the absence of disorder, produce identical results for \mathbf{r}_{cm} , up to a sign change. However, the non-zero standard deviations measured in the bond characterisation data indicates the presence of bond strength disorder within the experimental lattice (such a disorder will be referred to as off-diagonal disorder). The effects of this disorder can be

directly observed in the experimental lattice with the four different launch sites producing slightly different results for \mathbf{r}_{cm} , see the error bars in fig. 5.6.

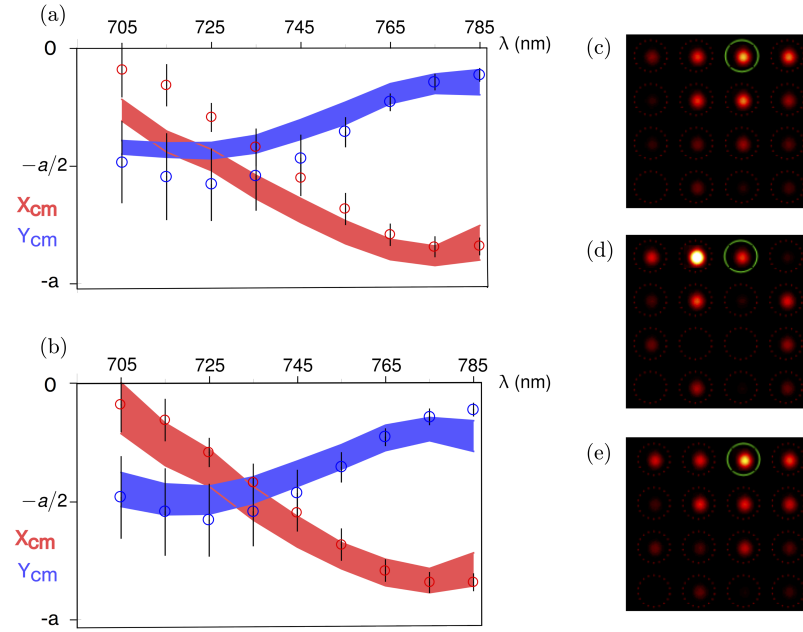


Figure 5.6: Figures (a) and (b) compare the experimental centre of mass drifts, as defined by Eq. (5.7), for two different disorder models: model 1, (a), includes bond strength disorder only whilst model 2 has additional on-site(diagonal) disorder. The centre of mass drift for four different launch sites is measured experimentally and the red and blue circles indicate the average drift in the x and y directions whilst the black error bars indicate the measured standard deviations. The shaded regions in (a) and (b) indicate the theoretical disorder-averaged value plus/minus one standard deviation. Figure (c) is the experimental output image, averaged over 4 launch sites, for an input light wavelength of 705 nm; this wavelength corresponds to $\Lambda_2 \approx 0.8$. (d) and (e) are the disordered averaged output facet images obtained from models 1 and 2 respectively.

In order to theoretically model this disorder, the strengths of the bonds J_{2-4} were randomly selected to lie within the range measured in the bond characterisation data. The comparison between the experimental data and the theoretical prediction shows good agreement around $\lambda \approx 785$ nm, see fig. 5.6(a), but deviations are observed at smaller wavelengths particularly in the x direction. The failure of the theoretical model in this region is further illustrated in fig. 5.6(c-d), which compares the averaged experimental output image, fig. (c), to the theoretical image, (d), averaged over 1000 disorder realisations.

The match between theory and experimental results can be improved by including a small onsite disorder term, $\Delta\beta_{m,n}$, in addition to the coupling disorder of the

previous model (this form of disorder will be referred to as diagonal disorder). The $\Delta\beta_{m,n}$ for the (m, n) site is a random number drawn from within a uniform distribution covering the interval $[-W, W]$. Note that, as is the case for the couplings, were $JT/4$ is the dimensionless parameter of interest, the disorder is likewise characterised by a dimensionless disorder strength $D = WT/4$. The disorder strength is chosen as $WT/4 = D = 0.6$, as this particular value results in the best fit to the experimental data over the whole wavelength range investigated. The corresponding centre of mass prediction, fig. 5.6(b), and output facet image, fig. (e), produced by this model are in closer agreement to the experimental results which hints towards a disordering of this type being present in the lattice.

5.4.1 Topological transition

The inclusion of disorder in the system can allow bandgap closings to occur which can modify the topology of the system. In particular, the disorder could potentially change the Chern numbers of the Floquet bands to different values compared to the clean system. The investigation of this possibility thereby requires the calculation of the Chern number in a disordered system. The presence of disorder means that quasimomentum is no longer a good quantum number which in turn precludes the use of the usual momentum space techniques in calculating the Chern number. In order to overcome this limitation a real-space Chern invariant, $C(\epsilon_0)$, was introduced by Bianco and Resta in ref. [11]. This invariant generalises the ability of the static bulk-edge correspondence in predicting the number of edge modes in a band gap at energy ϵ_0 to also include disordered and quasi-periodic lattices [11, 123]. In particular, when the energy, ϵ_0 , is placed in a mobility gap of the spectrum the Chern invariant will measure the number of chiral edge modes which cross this energy, as predicted by the Chern numbers of the bands below this energy. This real-space Chern invariant is based around an operator called the Chern marker, $\hat{\mathcal{C}}$, which is defined by

$$\hat{\mathcal{C}} = -4\pi Im[\hat{x}_Q \hat{y}_P] \quad (5.8)$$

Here the operators $\hat{\mathbf{r}}_P = \hat{P}\hat{\mathbf{r}}\hat{Q}$ and $\hat{\mathbf{r}}_Q = \hat{Q}\hat{\mathbf{r}}\hat{P}$ are expressed in terms of the position operator $\hat{\mathbf{r}} = (\hat{x}, \hat{y})$ and the projection operators

$$\hat{P}(\epsilon_0) = \sum_{\epsilon \leq \epsilon_0} |\psi(\epsilon)\rangle\langle\psi(\epsilon)| = 1 - \hat{Q} \quad (5.9)$$

where $|\psi(\epsilon)\rangle$ is an eigenstate of the disordered Hamiltonian with energy ϵ . In the absence of disorder a real space Chern number can be defined by averaging the Chern marker operator over a unit cell,

$$C = \int_{cell} \langle \mathbf{r} | \hat{\mathcal{C}} | \mathbf{r} \rangle d\mathbf{r} = \int_{cell} \mathcal{C}(\mathbf{r}) d\mathbf{r} \quad (5.10)$$

In the presence of disorder this real-space Chern number fluctuates depending upon the position of the unit cell. These fluctuations can be accounted for by replacing the unit-cell average by an average over an area A that is located within the bulk and is large compared to the fluctuation length.

The ability of the real space Chern marker to characterise the topology of disordered systems has important applications. In the anomalous regime it eliminates the possibility that the disorder has changed the Chern numbers of the Floquet bands to nontrivial values. Note that such disorder-driven topological transitions can be observed in both static [44, 74] and driven systems [121, 122]. The elimination of any disorder-driven transition would further strengthen the claim that the experimentally observed edge modes are in fact anomalous topological modes. In addition to this verification the analysis can also be conducted for shorter wavelengths corresponding to weaker couplings. Intriguingly this analysis suggests that for weak couplings, small Λ , the phenomenological on-site disorder that was needed to account for the experimental results is powerful enough to trigger a topological transition.

In order to understand the effects of the disorder on the topology of the driven systems the local Chern marker is calculated at the centre of the fundamental quasi-energy zone, $\epsilon_0 = 0$. The real-space average of this local Chern marker, the Chern invariant, can be viewed as the prediction coming from the *static* bulk-

edge correspondence for the number of chiral edge modes that are traversing the mobility gap between the two bands. Fig. 5.7(a) depicts how the Chern invariant changes with increasing disorder strength for the parameters ($\Lambda_1 = 0, \Lambda_2 = \pi/2$) and ($\Lambda_1 = 0, \Lambda_2 = 0.8$), parameters corresponding to the black and grey dots in the phase diagram of fig. 5.3 respectively. The results were obtained by averaging the Chern invariant over 100 realisations of the disorder and the error bars show the standard deviation. Within each disorder realisation the Chern invariant was calculated by averaging the local Chern marker over 20 lattice sites and it was checked that the results were independent of the location or size of this averaging. The black squares describe the parameters ($\Lambda_1 = 0, \Lambda_2 = \pi/2$) and show no disorder induced topological transition. Consequently, the Chern numbers of all the bands are zero and the *static* bulk-edge correspondence predicts the absence of any edge modes which is in sharp contrast to what is observed experimentally. This further strengthens the claim that the experimentally observed edge modes are anomalous.

The grey squares in fig. 5.7(a) describe lattices with the parameters ($\Lambda_1 = 0, \Lambda_2 = 0.8$) and the results show a disorder-induced topological transition for $D \approx 0.45$. In the previous section it was discussed how a good match between the experimental and theoretical results were obtained for $D = 0.6$ which indicates that the experimental disorder levels are sufficient to have driven a topological transition. Therefore, assuming that the disorder strength is approximately wavelength independent the experimental lattice should host two distinct topological regimes: a topological regime for parameters around $\Lambda_2 \approx \pi/2$ and a topologically trivial regime around $\Lambda_2 \approx 0.8$. In order to appreciate the transition between these two situations we study the disorder-averaged transmission probability, $G_{edge}(\epsilon)$, which informs on the presence of chiral edge modes at quasienergy ϵ [120, 121]. We consider the evolution of an initial state, ψ_0 , that is localised onto a single site on the edge of lattice. The transmission amplitude on the site \mathbf{r} , in each disorder realisation, is obtained by a Fourier transformation of the real-time probability amplitude

$$G^N(\mathbf{r}, \epsilon) = \frac{1}{N} \sum_{n=0}^N \langle \mathbf{r} | \hat{U}^n | \psi_0 \rangle e^{i\epsilon T_n}, \quad (5.11)$$

where $\hat{U} = \hat{U}(T)$ is the evolution operator for one driving period and N determines the total time of evolution. We define the edge transmission as $G_{edge}^N(\epsilon) = \sum_{\mathbf{r}_{edge}} G^N(\mathbf{r}, \epsilon)$ where \mathbf{r}_{edge} are the lattice sites on the edge of the sample. The disorder-averaged function $\langle |G_{edge}^N(\epsilon)|^2 \rangle$ is a quasi-energy resolved measurement that is sensitive to the existence of extended states which are localised around the edge of the lattice. Consequently, a large value of $\langle |G_{edge}^N(\epsilon)|^2 \rangle$ is an indicator of the presence of chiral edge modes in the system at the quasienergy ϵ . Fig. 5.7(b) shows how $\langle |G_{edge}^N(\epsilon)|^2 \rangle$ varies as a function of the quasienergy, ϵ , and the coupling strength Λ_2 . The strength of the disorder is chosen as $D = 0.6$. The results shown in (b) show that lattices with strong coupling, $\Lambda_2 \approx \pi/2$, exhibit edge modes around $\epsilon T = \pm\pi$ and $\epsilon T = 0$, whilst the low coupling lattices, $\Lambda_2 < 1.1$, do not feature any edge modes. This latter statement is in keeping with the topological transition that is predicted in (a).

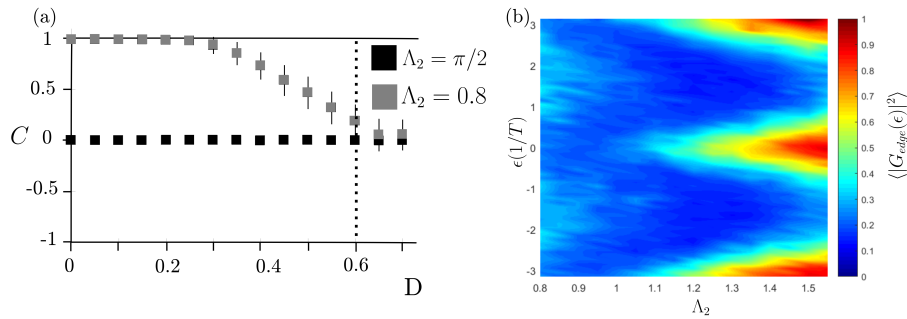


Figure 5.7: (a) illustrates the Chern number of the lower Floquet band for increasing levels of disorder for two different Λ_2 parameters, $\Lambda_1 = 0$ for both cases. The large Λ_2 case shows no topological transition and so the *static* bulk-edge correspondence predicts the absence of any edge modes, in contrast to what is observed experimentally. The weaker coupling case undergoes a topological transition for a disorder strength of $D \approx 0.45$. Fig. (b) plots the disorder averaged, quasienergy resolved, transmission function $\langle |G_{edge}(\epsilon)|^2 \rangle$ as a function of the coupling strength Λ_2 . Values greater than a half indicate the existence of chiral edge modes at that quasienergy. The disorder strength is taken to be $D = 0.6$.

5.4.2 Future work

The current phenomenological nature of the disorder model is not ideal and so future work investigating the nature and magnitude of the on-site disorder terms would be beneficial. The sensitivity of the topology to on-site disorder implies that if the

disorder can be experimentally controlled it would provide a powerful parameter with which to study disorder driven transitions in slowly-driven systems.

5.5 Chapter summary

In this chapter, we presented a slowly-driven photonic square lattice and demonstrated the existence of chiral topological edge modes which are robust against defects. The theoretical analysis shows that these edge modes have no static analogue and are associated with a distinct topological invariant known as the winding number. Two particularly interesting features of this slowly-driven photonic system are the ability to easily excite edge modes, with almost unit efficiency, and the co-existence of chiral edge modes with a dispersionless bulk. These properties make this lattice a promising platform for investigating topological transport properties in response to perturbations, such as external (engineered) fields, disorder, and particle-particle interaction (as generated by optical non-linearities).

Chapter 6

Two-Body physics in the cross-stitch and diamond lattices

6.1 Introduction

In the decades since the Hubbard model [59] was developed for describing the interaction between particles in a lattice this conceptually simple model has become the workhorse of the condensed matter field [19, 118]. The one-dimensional model in particular is of great interest as in the few-body limit there exist exact analytical solutions [20, 126, 128] whilst for larger particle numbers there exist powerful numerical techniques that allow almost exact solution [133, 137]. This interest has, in the last decade particularly, extended to the experimental regime with both cold-atom and photonic lattice experiments becoming capable of realising the few-body Hubbard model with almost complete control over the system parameters. This control has allowed for the experimental observation of a number of theoretically predicted effects [16, 30, 96, 110, 116, 138]. The capability of these experimental techniques is continually increasing and, as was shown in a recent paper [116], now allows for the study of few-body dynamics on quasi one-dimensional lattices. This possibility is an exciting development as quasi one-dimensional systems can display considerably richer single particle properties. In particular, a number of quasi one-dimensional lattices host flat energy bands wherein particles have no kinetic energy and thereby their dynamics become fully determined by the interactions between the particles.

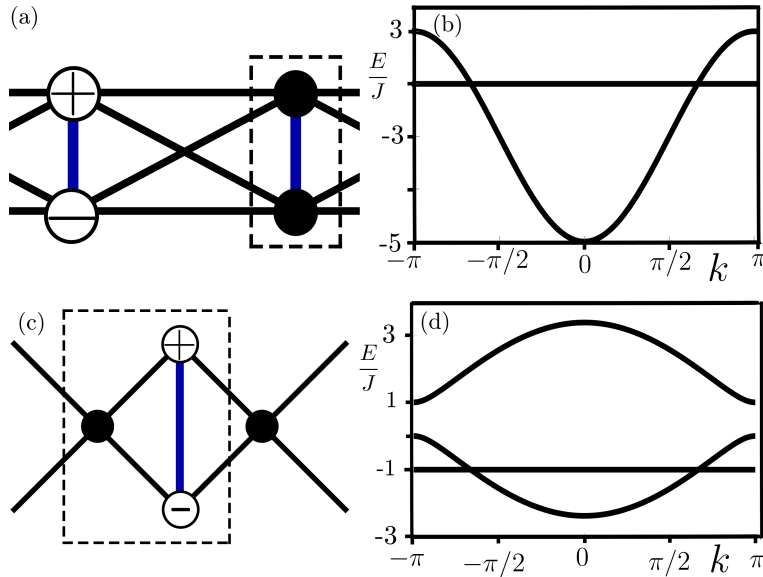


Figure 6.1: Figures (a) and (c) show the geometries of the cross-stitch and diamond lattices respectively where the black lines show bonds of strength J and the vertical blue lines show bonds of strength t . The unit cell of the lattices is shown with the dashed box. The single particle energy spectrums, show in (b) and (d) for $t = J$, both exhibit a flat band. The linear superposition of flat-band Bloch states gives rise to compact eigenfunctions that equally occupy only two lattice sites as shown by the white circles in (a) and (c). The sign of the wavefunction is shown inside the white circle. A simple check shows that destructive interference stops the state from expanding.

The strongly correlated nature of these particles has attracted considerable theoretical attention and it has been studied in both the few- [129, 134] and many-body limits [21, 45, 60, 94].

In this chapter the interaction of two particles in the cross-stitch and diamond lattices, see fig. 6.1 for their geometries, are studied. The two-body case in the diamond lattice has been studied by Vidal et al. [134] for the case when the lattice is subject to a very particular value of magnetic flux. The flux is chosen so that all the single-particle Bloch bands are flat bands, so-called Aharonov-Bohm caging [134, 135]. In this work, by contrast, the lattices are studied in the absence of any flux and consequently the dynamics are the result of the interplay between flat and dispersive bands. It is found that for both lattices the dynamics depend critically on how many particles are initially placed in the flat band. In the case where a single particle occupies the flat band the model becomes equivalent to a one-dimensional scattering problem with the dispersive particle scattering off the

infinitely heavy flat-band particle. In the alternative case where both particles are placed in either the dispersive or flat bands the two-body Schrödinger equation is shown to be equivalent to a single particle moving in a quasi-three-dimensional lattice consisting of two layered square lattices. In the case of the cross-stitch lattice the problem is shown to be equivalent to the famous Fano-Anderson model and is analytically solvable. In the case of the diamond lattice a modified Bethe Ansatz is used to show the existence of a number of interesting phenomena including bound states in the continuum and the possibility for realising a quasi-flat bound state band.

6.1.1 Cross-Stitch lattice

In this chapter, we study two interacting bosonic particles in the cross-stitch and diamond lattices. The cross-stitch lattice owing to its smaller unit cell is the simpler case and so is studied first. The single-particle Hamiltonian is given by

$$\hat{H}_0 = -J \sum_m (\hat{a}_m^\dagger \hat{a}_{m+1} + \hat{a}_m^\dagger \hat{b}_{m+1} + \hat{b}_m^\dagger \hat{b}_{m+1} + \hat{b}_m^\dagger \hat{a}_{m+1}) - t \sum_m \hat{a}_m^\dagger \hat{b}_m + \text{h.c} \quad (6.1)$$

where \hat{a}_m^\dagger creates a particle in the m^{th} unit cell on the sublattice $\alpha = \{a, b\}$, J and t represent the nearest neighbour and cross-link hopping amplitudes respectively. The unit cell and the geometry of the bonds are shown in fig. 6.1(a). An intriguing feature of the cross-stitch single particle Hamiltonian is its support of a flat band, see figure 6.1(b), that arises due to the presence of geometrical frustration within the lattice. The macroscopic degeneracy of the flat band means that highly localised eigenstates may be obtained by a linear superposition of these degenerate flat-band states. In the cross-stitch and diamond lattices these compact states occupy only two sites as shown by the white circles in figure 6.1(a). Importantly, these localised states only occupy one unit cell which consequently implies that the localised states on neighbouring unit cells are orthogonal. The presence of these localised states, as was noted in ref. [29], allows the single-particle Hamiltonians to be rewritten in a simpler form. Introducing the operator $\hat{f}_m^\dagger = \frac{1}{\sqrt{2}}(\hat{a}_m^\dagger - \hat{b}_m^\dagger)$, which creates a localised state in the m^{th} unit cell and its orthogonal counterpart $\hat{g}_m^\dagger = \frac{1}{\sqrt{2}}(\hat{a}_m^\dagger + \hat{b}_m^\dagger)$

the single-particle Hamiltonian can be rewritten as

$$\hat{\mathcal{H}}_0^C = -2J \sum_m \hat{g}_m^\dagger \hat{g}_{m+1} + h.c + 2t \sum_m \hat{f}_m^\dagger \hat{f}_m. \quad (6.2)$$

This transformed single-particle Hamiltonian can be visualised as a one-dimensional chain with the addition that for each unit cell there exists a side lattice site which is uncoupled to the main chain, as shown in fig. 6.2(a).

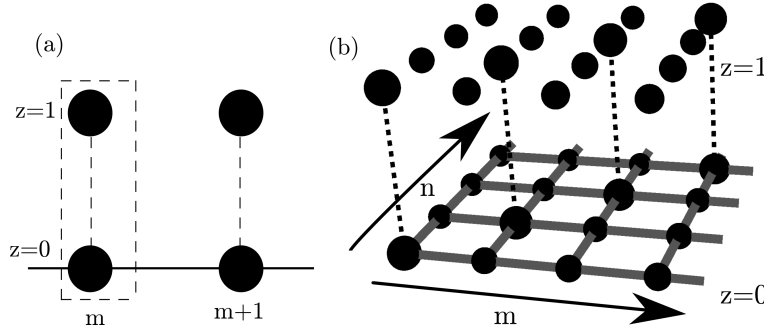


Figure 6.2: Figure (a) illustrates the transformed single-particle cross-stitch lattice, equation 6.2, where the black lines show bonds of strength $2J$. The top lattice sites are only coupled to the main chain via the dashed lines which are interaction-induced cotunneling terms, see equation 6.4. In the case where both particles are placed in either the dispersive or flat bands the two-body wavefunction describing the dynamics is equivalent to a single particle moving in the three-dimensional lattice shown in (b). Note that in the upper layer only the diagonal lattice sites have any coupling and are coupled to the lower lattice by an interaction induced tunnelling, the dashed lines. The presence of the interaction is further encoded in the diagonal lattice sites of both the upper and lower layers which have a sublattice energy that depends on the interaction strength U .

6.1.2 Interaction

In this work we consider that the two particles interact via an attractive or a repulsive on-site interaction of strength U . In second quantized form this on-site interaction is described by the Hamiltonian \hat{H}_U which takes the form

$$\hat{H}_U = \frac{U}{2} \sum_m (\hat{a}_m^\dagger \hat{a}_m^\dagger \hat{a}_m \hat{a}_m + \hat{b}_m^\dagger \hat{b}_m^\dagger \hat{b}_m \hat{b}_m). \quad (6.3)$$

Applying the basis transformation provided by the operators \hat{f}_m^\dagger and \hat{g}_m^\dagger gives

$$\hat{H}_U = \frac{U/2}{2} \sum_m \left[4\hat{g}_m^\dagger \hat{f}_m^\dagger \hat{g}_m \hat{f}_m + \hat{g}_m^\dagger \hat{g}_m^\dagger (\hat{g}_m \hat{g}_m + \hat{f}_m \hat{f}_m) + \hat{f}_m^\dagger \hat{f}_m^\dagger (\hat{g}_m \hat{g}_m + \hat{f}_m \hat{f}_m) \right]. \quad (6.4)$$

The last three terms of Eq. (6.4) are co-tunnelling operators that move both particles between the main chain of fig. 6.1(a) and the side sites. Consequently, if the system is initialised in the state with one particle on the main chain, i.e. in the dispersive band, and the other particle on the side sites, i.e. in the flat band, then these co-tunnelling terms will have no effect. Furthermore, the first term forms the product of the number of particles on the f and g sublattices and so in the two-particle sector is only non-zero when the particles are on different sublattices. The consequence of these two statements is that the Hilbert space consisting of two particles in the same band is independent from the subspace where the particles occupy different bands.

6.2 Wave functions of the two-body problem

6.2.1 Single particle mapping

A useful technique for studying two-body physics in a N -dimensional lattice is to convert the two-body problem into the study of a single particle moving in a $2N$ -dimensional lattice [80]. The interaction between the particles translates into a modification of the local potential of some of the lattice sites in the 2D-dimensional structure. For instance the Schrödinger equation for two particles in a one dimensional lattice with on-site interaction of strength U is equivalent to a single particle moving in a square lattice but where the diagonal lattice sites have an on-site energy U . This approach is useful in the study of the cross-stitch and diamond lattices. This analysis will explicitly reveal the partitioning of the Hilbert space depending on the occupancy of the bands. The Schrödinger equations for these two independent subspaces can then be mapped into equivalent single-particle Schrödinger equations.

The two-body wavefunction can be written as

$$|\Psi\rangle = \sum_{m,n} \left[\psi^0(m,n)(\hat{c}_m^0)^\dagger(\hat{c}_n^0)^\dagger + \psi^1(m,n)(\hat{c}_m^1)^\dagger(\hat{c}_n^1)^\dagger + \psi^M(m,n)(\hat{c}_m^1)^\dagger(\hat{c}_n^0)^\dagger \right] |0\rangle \quad (6.5)$$

where $(\hat{c}_m^z)^\dagger$ creates a particle on the $(m, z)^{th}$ lattice site with $m \in \mathbb{Z}$ and $z = \{0, 1\}$, see figure 6.2(a). The amplitudes $\psi^z(m, n)$ define the probabilities to find the two particles at lattice sites (m, z) and (n, z) . The amplitude, $\psi^M(m, n)$ defines the probability to find the two particles at lattice sites $(m, 1)$ and $(n, 0)$. This can be interpreted as describing one particle in the flat band and one particle in one of the dispersive bands. Inserting the wavefunction into the Schrödinger equation, $E|\Psi\rangle = (\hat{\mathcal{H}}_0 + \hat{\mathcal{H}}_U)|\Psi\rangle$, yields the following eigenvalue problem for the amplitudes

$$E \begin{bmatrix} \psi^0(m, n) \\ \psi^1(m, n) \\ \psi^M(m, n) \end{bmatrix} = \begin{bmatrix} H_{00} & \delta_{m,n} \frac{U}{2} & 0 \\ \delta_{m,n} \frac{U}{2} & H_{11} & 0 \\ 0 & 0 & H_{MM} \end{bmatrix} \begin{bmatrix} \psi^0(m, n) \\ \psi^1(m, n) \\ \psi^M(m, n) \end{bmatrix}. \quad (6.6)$$

The matrix elements H_{00} , H_{11} and H_{MM} will be discussed in the upcoming sections but there are several important comments to be made about Eq. (6.6). Firstly, the probability amplitudes $\psi^M(m, n)$ are uncoupled from the probability amplitudes $\psi^{0,1}(m, n)$. In terms of the cross-stitch lattice this statement implies that the subspace consisting of one particle in the flat band and one in the dispersive band is independent from the remainder of the Hilbert space—which consists of both particles being in either the dispersive or flat bands. This was previously eluded to in section 6.1.2. Secondly, only the interaction links the probability amplitudes $\psi^0(m, n)$ and $\psi^1(m, n)$ together.

6.2.2 One flat-band particle

The eigenvalue equation for the probability amplitudes, Eq. (6.6), makes it clear that the dynamics of the mixed probability amplitude, $\psi^M(m, n)$, is determined by

the matrix element H_{MM} . The Schrödinger equation gives

$$\begin{aligned} E\psi^M(m, n) &= H_{MM}\psi^M(m, n) \\ &= -2J \left(\psi^M(m, n+1) + \psi^M(m, n-1) \right) + U\psi^M(m, n)\delta_{m,n}. \end{aligned} \quad (6.7)$$

Clearly there is no coupling between the mixed states $\psi^M(m, n)$ and $\psi^M(m', n')$ if $m' \neq m$. This can be interpreted as saying that if one particle is loaded into the state \hat{f}_m^\dagger , i.e. into the flat band, and the other particle is loaded into the dispersive band then the particle in the flat band remains in the state \hat{f}_m^\dagger for all time. In contrast, the dispersive particle is free to move and in doing so scatters off the fixed particle. In the case of an infinite lattice or periodic boundary conditions the Schrödinger equation for each m becomes identical and is equivalent to a one-dimensional lattice with an impurity located at the centre of the lattice. In the case of open boundary conditions the Schrödinger equation for the mixed states with different values of m describe one-dimensional impurity scattering but where the position of the impurity depends on m . The scattering of a particle in a one-dimensional lattice off a fixed impurity is closely related to the study of the two particle sector in the one dimensional Bose-Hubbard model and, as such, the eigenenergies and eigenstates are well-known [126].

6.2.3 Doubly occupied bands

In the previous section it was shown that in the case where only one particle occupies the flat band the resultant dynamics remain within that subspace indefinitely. The case where both particles are in the same band is decidedly different with the interaction allowing the co-tunneling of both particles from the flat band into the dispersive band and vice-versa. Consequently, this interaction induced tunnelling provides a mechanism by which the doubly occupied flat band can decay. The Schrödinger equation describing these dynamics is equivalent to a single particle moving in a quasi-three dimensional lattice consisting of two vertically stacked square lattices,

see fig. 6.2(b). The wavefunction obeys the Schrödinger equation given by

$$-2J \sum_{\mu=-1,1} [\psi^0(m + \mu, n) + \psi^0(m, n + \mu)] \delta_{z,0} + \frac{U}{2} \delta_{m,n} \psi^z(m, n) + \frac{U}{2} \delta_{m,n} \psi^{z+1}(m, n) + 2t \psi^1(m, n) \delta_{z,1} = E \psi^z(m, n) \quad (6.8)$$

where $(m, n) \in \mathbb{Z}$ and $z \in \{0, 1\}$ and it is defined that $\psi^2(m, n) = \psi^0(m, n)$. The presence of the interaction is encoded in two ways: firstly, the diagonal lattice sites, sites with $m = n$, have an on-site energy that depends on the interaction strength and secondly, the tunnelings in the z-direction, the dashed lines in figure 6.2(b), are interaction induced tunnellings of strength $U/2$. An important note is that in the upper lattice only the diagonal lattice sites are coupled. This is a consequence of the on-site nature of the interaction. The lattice sites with coordinates $z = 1$ and $m \neq n$ correspond to both particles being placed in spatially separated flat band states and so feel no interaction and so consequently are eigenstates of the system.

6.2.4 Fano-Anderson model

It is instructive to study the $z = 0$ and $z = 1$ sections of the Schrödinger equation, Eq. (6.8), separately. This analysis naturally leads to the Fano-Anderson model [5, 28, 85], an iconic model in condensed matter. The $z = 0$ component of the lattice is intimately related to the study of the two-particle sector of the one-dimensional Bose-Hubbard model and, as such, the exact real-space eigenstates of this problem are well known [126]. These eigenstates can be separated into extended Bloch-like scattering states, $\psi_s^{K,k}(R, r, z)$, and exponentially localised bound states, $\psi_B^K(R, r, z)$. These states make a sensible basis for the $z = 0$ section of the lattice whilst a good basis for the $z = 1$ lattice are plane waves

$$\begin{aligned} \psi_s^{K,k}(R, r, z) &= \delta_{z,0} \frac{\sqrt{2} e^{iKR}}{N} \cos(k|r| + \phi_{K,k}), \\ \psi_B^K(R, r, z) &= \delta_{z,0} \frac{e^{iKR}}{\sqrt{N}} \frac{\sqrt{|U_K|}}{\sqrt[4]{|U_k|^2 + 1}} (U_K - \text{sgn}(U) \sqrt{U_K^2 + 1})^{|r|}, \\ \psi_p^K(R, r, z) &= \delta_{z,1} \delta_{r,0} \frac{1}{\sqrt{N}} e^{iKR} \end{aligned} \quad (6.9)$$

where $U_K = \frac{U}{4J_K}$, $\tan(\phi_{K,k}) = -U_K \csc(k)$, $J_K = 4J \cos(K/2)$ and N is the number of unit cells in the original cross-stitch lattice. The spatial form of the wavefunctions are expressed in terms of the centre-of-mass ($R = (m + n)/2$) and relative ($r = m - n$) coordinates of the two particles. The variables $K = [-\pi, \pi]$ and $k = [0, \pi]$ describe the total and relative quasi-momenta of the two particles respectively. The Schrödinger equation in this basis is diagonal in terms of the total quasimomentum K and introducing the operators $\hat{d}_K^\dagger |0\rangle = |\psi_p^K\rangle$, $\hat{c}_{K,k}^\dagger |0\rangle = |\psi_s(K, k)\rangle$ and $\hat{b}_K^\dagger |0\rangle = |\psi_b(K)\rangle$ allows the Hamiltonian to be written in second quantised notation as

$$\frac{1}{2J_K} \hat{\mathcal{H}} = \epsilon_d \hat{d}^\dagger \hat{d} + \epsilon_b \hat{b}^\dagger \hat{b} + \sum_k \epsilon_k \hat{c}_k^\dagger \hat{c}_k + \sum_k t_k (\hat{c}_k^\dagger \hat{d} + \hat{d}^\dagger \hat{c}_k) + t (\hat{b}^\dagger \hat{d} + \hat{d}^\dagger \hat{b}) \quad (6.10)$$

where the subscript K on the operators has been dropped for convenience. This Hamiltonian is closely related to a well-known condensed matter model called the Fano-Anderson model which describes a localised state of energy ϵ_d and operators \hat{d} and \hat{d}^\dagger mixing with a continuous set of states of energy ϵ_k with operators \hat{c}_k and \hat{c}_k^\dagger . The Hamiltonian of Eq. (6.10) is very similar however it features an additional term which is the coupling between the localised d state and another localised state which has energy ϵ_b and is described by the operators \hat{b} and \hat{b}^\dagger .

6.2.5 Green's function solution

The Fano-Anderson model is most commonly approached by solving for the Green's function of the localised state and is discussed in many textbooks, see for instance [85]. A brief derivation is provided here. The Green's function of the localised state in the time-domain is defined by $G_{dd}(t) = -i\theta(t)\langle\{\hat{d}(t), \hat{d}^\dagger(0)\}\rangle$, where $\theta(t)$ is the Heaviside step function. This Green's function has a clear physical interpretation; at time $t = 0$ a particle is placed into the d state and allowed to evolve. The quantity $|G_{dd}(t)|^2$ provides the probability of retrieving the particle from the d state after a time t has elapsed. In terms of the original cross-stitch lattice this can be interpreted as meaning at time $t = 0$ both particles are initialised in flat-band states of the form $\sum_m e^{iKm} \hat{f}_m^\dagger |0\rangle$ and allowed to evolve. The quantity $G_{dd}(t)$ therefore quantifies how the probability amplitude for finding the two particles in the

flat band changes with time. In time-independent problems the Green's functions are most easily obtained in the energy domain. The energy domain Green's functions are related to the time dependent Green's functions by Fourier transformation, $G_{dd}(E) = \frac{1}{2\pi} \int_{-\infty}^{\infty} dt e^{-iEt} G_{dd}(t)$. The Green's function for the localised state is

$$G_{dd}(t) = -i\theta(t)\langle\{\hat{d}(t), \hat{d}^\dagger(0)\}\rangle \quad (6.11)$$

where we have, without loss of generality, set the creation time to zero. Its time-derivative is thus given by

$$i\dot{G}_{dd}(t) = \delta(t) + \theta(t)\langle\{\dot{\hat{d}}(t), \hat{d}^\dagger(0)\}\rangle \quad (6.12)$$

By the Heisenberg equation of motion, the time-evolution of the operator $\hat{d}(t)$ is given by

$$i\dot{\hat{d}} = [\hat{d}, \hat{H}], \quad (6.13)$$

$$= \epsilon_d \hat{d} - \sum_k t_k \hat{c}_k - \tilde{t} \hat{b} \quad (6.14)$$

Substituting this into Eq. (6.12), we obtain

$$i\dot{G}_{dd}(t) = \delta(t) + \epsilon_d G_{dd} - \sum_k t_k G_{kd} - \tilde{t} G_{bd} \quad (6.15)$$

where we have defined the 'mixed' Green's functions G_{kd} and G_{bd} by

$$\begin{aligned} G_{kd}(t) &= -i\theta(t)\langle\{\hat{c}_k(t), \hat{d}^\dagger(0)\}\rangle, \\ G_{bd}(t) &= -i\theta(t)\langle\{\hat{b}(t), \hat{d}^\dagger(0)\}\rangle \end{aligned} \quad (6.16)$$

To close the equations, we now need the time-evolution of G_{kd} and G_{bd} as well. Following a similar path to that used for G_{dd} of taking the time derivative and using

the Heisenberg equations yields

$$\begin{aligned} i\dot{G}_{kd} &= \epsilon_k G_{kd} - t_k G_{dd}, \\ i\dot{G}_{bd} &= \epsilon_b G_{bd} - \tilde{t} G_{dd} \end{aligned} \quad (6.17)$$

Thus, we have three coupled differential equations for the dd , kd and bd Green's functions. Upon Fourier transformation to energy space the differential equations become algebraic and G_{kd} and G_{bd} can be obtained in terms of G_{dd} . The Green's function for the localised state can then be written as

$$G_{dd} = \frac{1}{E_K - \epsilon_d + is - \Sigma_{dd}} \quad (6.18)$$

where is is a small complex part that has been added to the unperturbed level energies and the dimensionless energy $E_K = E/(2J_K)$ has been introduced. Σ_{dd} is the self-energy and accounts for the effect of the other states on the localised state. The self-energy can be obtained in exact form and can be separated into real and imaginary parts

$$\Sigma_{dd} = \int_0^\pi dk \left(\frac{t_k^2}{E_K - \epsilon(k) + is} \right) + \frac{\tilde{t}^2}{E_K - \epsilon_b + is}, \quad (6.19)$$

$$\Sigma_{dd} = \left(-\frac{U_K^3}{1 + U_K^2 - E_K^2} \right) + i \left(-\frac{U_K^2 \sqrt{1 - E_K^2}}{1 + U_K^2 - E_K^2} \right) \quad \text{if } E_K^2 \leq 1, \quad (6.20)$$

$$= - \left(\frac{U_K^2 (U_K + sgn(E_K) \sqrt{E_K^2 - 1})}{1 + U_K^2 - E_K^2} \right) \quad \text{if } E_K^2 > 1 \quad (6.21)$$

where the expressions in brackets are real. The explicit knowledge of the self-energy allows all the Green's functions such as the mixed Green's functions, G_{kd} and G_{bd} , to be obtained via simple algebraic manipulations and so allows for complete characterisation of the problem.

The knowledge of the self-energy can be further exploited in allowing the spectral function, $A(E_K)$, to be obtained. The spectral function is intimately linked to the time dynamics of the localised state as the Green's function in the time domain

can be obtained by Fourier Transformation of the spectral function. The spectral function can be written as a sum of contributions coming from the bound states and a contribution coming from the continuum band which is defined as the region where $\Im(\Sigma) \neq 0$ [85].

$$A(\omega) = \sum_i 2\pi Z_i \delta(\tilde{\omega} - \Omega_i) - \frac{2\Im(\Sigma)}{(\tilde{\omega} - \tilde{\epsilon}_d - \Re(\Sigma))^2 + (\Im(\Sigma))^2} \quad (6.22)$$

$$Z_i = |1 - \frac{\partial}{\partial \tilde{\omega}} \Re(\Sigma)|_{\tilde{\omega}=\Omega_i}^{-1} \quad (6.23)$$

Here Z is the so-called renormalisation factor and gives the weight of $\hat{d}^\dagger |0\rangle$ in the i^{th} bound state. The second term in Eq. (6.22) comes from the continuum band and has the functional form of a Lorentzian which upon Fourier transformation to the time domain becomes a decaying exponential. This decay process has a clear physical interpretation and corresponds to the particle leaking from the localised state into the reservoir of continuum states. Consequently, in the long-term limit the contribution from this latter term disappears and the time domain Green's function becomes:

$$G_{dd}(t \rightarrow \infty) = -i\theta(t) \sum_i Z_i e^{-i\Omega_i t} \quad (6.24)$$

Therefore, the bound states play a crucial role in determining the long-term dynamics of the localised state. The poles of the Green's function correspond to the eigenenergies of the system and so can be used to find the energies and renormalisation factors of the bound states of the system.

6.2.6 Bound states

The interaction between the two particles can cause them to become bound together in a eigenstate that is exponentially localised in terms of the particle separation. The formation of these bound states can be predicted from the self-energy by finding the set of energies, denoted by E_i , that satisfy [85]

$$E_i = \epsilon_d + \Re(\Sigma_{dd}(E_i)) \quad \text{and} \quad \Im(\Sigma_{dd}(E_i)) = 0. \quad (6.25)$$

There are three important properties that can be obtained generally. Firstly, the imaginary part of the self-energy only vanishes outside the continuum which precludes the existence of bound states in the continuum, see diamond lattice analysis and refs. [78, 85]. Secondly, there is always at least one solution and the energy of this solution, E_1 , must obey the inequality $|E_1| > \sqrt{1 + U^2}$. Finally, a second bound state exists provided that the inequality $-1 + \epsilon_d \leq U_K \leq 1 + \epsilon_d$ is *not* fulfilled. Furthermore, if the interaction lies to the left of the inequality, i.e. $U \leq -1 + \epsilon_d$, then the energy of the second bound state, E_2 , satisfies $E_2 \geq 1$ whilst if the interaction strength lies to the right of the inequality the bound state energy satisfies $E_2 \leq -1$. The exact solutions of these equations can be found easily by a root-finding algorithm. Figure 6.3(a) shows how the bound states energy varies as a function of U_K for $\epsilon_d = 0$ whilst figure (b) shows a sample energy spectrum for $U = 5J$ and $\epsilon_d = 0$.

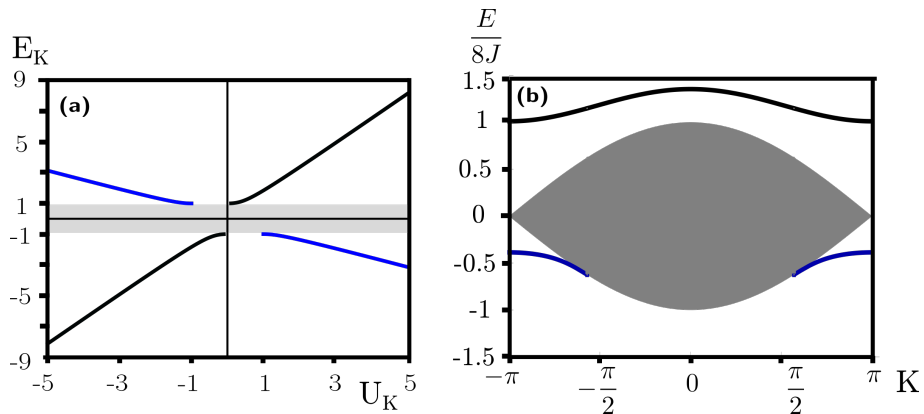


Figure 6.3: Figure (a) shows the dispersion of the bound states in terms of the dimensionless parameters U_K and E_K for $\epsilon_d = 0$. It can be clearly seen that there is always at least one solution and that for $|U_K| \geq 1$ a second bound state emerges from the continuum. Figure (b) shows an example spectrum for the case $U = 5J$ and $\epsilon_d = 0$ where the grey region shows the continuum band and the blue and black lines show the bound states.

6.2.7 Bound state wavefunctions

In the previous section it was shown that the cross-stitch lattice with non-zero interaction always possess at least one bound state. In this section the real space

form of the bound state wavefunctions is obtained. The following ansatz is used

$$\psi_K(R, r, z) = \left[\delta_{z,0}x^{|r|} + \delta_{z,1}\delta_{r,0}C \right] e^{iKR}. \quad (6.26)$$

Insertion of the ansatz at $(m = n, z = 0)$, $(m = n, z = 1)$ and $(m \neq n, z = 0)$ gives a set of three equations that can be written in terms of the energy of the bound state

$$C = \frac{U_K}{E_K - \epsilon_d}, \quad (6.27)$$

$$x = -E_K + U_K + \frac{U_K^2}{E_K - \epsilon_d}, \quad (6.28)$$

$$E_K^2 = 1 + \frac{U_K^2(E_K + U_K - \epsilon_d)^2}{(E_K - \epsilon_d)^2}. \quad (6.29)$$

The energy of the bound states can be obtained by finding the values of E_K which satisfy the final equality in Eq. (6.29). This equation is a fourth-order polynomial in E_K and therefore gives four potential bound state energies. Of these solutions, however, only real energies and energies that give $|x| \leq 1$ are physically acceptable. This latter condition is enforced as solutions with $|x| > 1$ cause the bound state wavefunction to diverge as $|r| \rightarrow \infty$. It can be easily checked numerically that the correct number of bound states, as predicted by the Green's function analysis, are obtained and therefore the ansatz of Eq. (6.26) correctly describes all the possible bound states.

6.3 Diamond lattice

The diamond lattice, the geometry of which is shown in fig. 6.1(c), is another example of a quasi one-dimensional lattice that hosts a flat band. The flat band supports localised states which are the same localised states as those in the cross-stitch lattice. This similarity means that the same operator transformation that was used in analysing the cross-stitch lattice can also be applied to the diamond lattice. The transformed lattice, as a result of it possessing three Bloch bands, is more complex but a number of the simplifications that applied to the cross-stitch lattice still apply.

The single-particle Hamiltonian for the diamond lattice is given by

$$\hat{H}_0 = -J \sum_m (\hat{c}_m^\dagger \hat{a}_m + \hat{c}_m^\dagger \hat{b}_m + \hat{a}_m^\dagger \hat{c}_{m+1} + \hat{b}_m^\dagger \hat{c}_{m+1}) - t \sum_m \hat{a}_m^\dagger \hat{b}_m + \text{h.c.} \quad (6.30)$$

where $\hat{\alpha}_m^\dagger$ creates a particle in the m^{th} unit cell on the sublattice $\alpha = \{a, b, c\}$, J and t represent the nearest neighbour and cross-link hopping amplitudes respectively. Using the transformation provided by the localised states \hat{f}_m and \hat{g}_m gives the transformed single-particle Hamiltonian

$$\hat{\mathcal{H}}_0 = -\sqrt{2}J \sum_m (\hat{g}_m^\dagger \hat{c}_m + \hat{g}_m^\dagger \hat{c}_{m+1}) + \text{h.c.} + \frac{3t}{2} \sum_m \hat{f}_m^\dagger \hat{f}_m + \frac{t}{2} \sum_m (\hat{c}_m^\dagger \hat{c}_m - \hat{g}_m^\dagger \hat{g}_m). \quad (6.31)$$

The transformed Hamiltonian, as it was for the cross-stitch lattice, can be visualised as a one-dimensional chain with nearest-neighbour hoppings only and a set of uncoupled side lattice sites, see fig. 6.4(a). The interaction Hamiltonian is composed of on-site interaction terms on the a, b and c sublattices, the latter of which will be unaffected by the operator transformation,

$$\hat{H}_U = \frac{U}{2} \sum_m (\hat{a}_m^\dagger \hat{a}_m^\dagger \hat{a}_m \hat{a}_m + \hat{b}_m^\dagger \hat{b}_m^\dagger \hat{b}_m \hat{b}_m + \hat{c}_m^\dagger \hat{c}_m^\dagger \hat{c}_m \hat{c}_m) \quad (6.32)$$

In terms of the transformed basis the interaction Hamiltonian becomes

$$\hat{\mathcal{H}}_U = \frac{U/2}{2} \sum_m [2\hat{c}_m^\dagger \hat{c}_m^\dagger \hat{c}_m \hat{c}_m + \hat{g}_m^\dagger \hat{g}_m^\dagger (\hat{g}_m \hat{g}_m + \hat{f}_m \hat{f}_m)] \quad (6.33)$$

$$+ \hat{f}_m^\dagger \hat{f}_m^\dagger (\hat{g}_m \hat{g}_m + \hat{f}_m \hat{f}_m) + 4\hat{g}_m^\dagger \hat{g}_m \hat{f}_m^\dagger \hat{f}_m] \quad (6.34)$$

6.3.1 Single-particle mapping

In a similar manner to the cross-stitch lattice analysis the dynamics of the two particles moving in this system of chain plus side sites can be mapped into the study of a single particle in a higher-dimensional lattice. The two-body wavefunction can

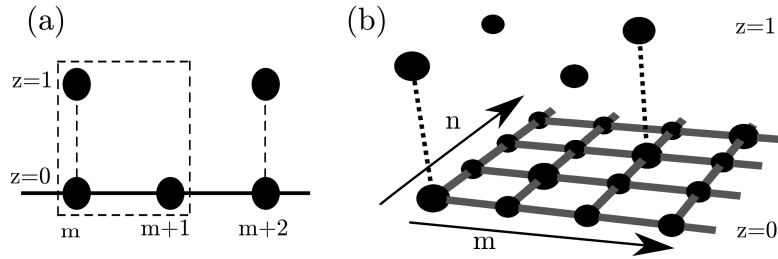


Figure 6.4: Figure (a) illustrates the transformed single-particle diamond lattice. The black lines show bonds of strength $\sqrt{2}J$ whilst the dashed bonds indicate the interaction induced co-tunnelling terms and the boxed region shows the unit cell. In contrast to the cross-stitch case the co-tunnelling only occurs between certain sites. The Schrödinger equation for the case where both particles are placed in the flat band or one of the dispersive bands is equivalent to a single particle moving in a three dimensional lattice, figure (b). The dashed lines show the interaction induced tunnelling and note that the upper lattice only has sites when both the m and n coordinates of the lattice sites are even.

be written as

$$|\Psi\rangle = \sum_{m,n} \left[\psi^0(m, n)(\hat{c}_m^0)^\dagger(\hat{c}_n^0)^\dagger + \psi^1(m, n)(\hat{c}_m^1)^\dagger(\hat{c}_n^1)^\dagger + \psi^M(m, n)(\hat{c}_m^1)^\dagger(\hat{c}_n^0)^\dagger \right] |0\rangle \quad (6.35)$$

where $(\hat{c}_m^z)^\dagger$ creates a particle on the $(m, z)^{th}$ lattice site. In contrast to the cross-stitch case where $m \in \mathbb{Z}$ for both $z = 0$ and $z = 1$ here $m \in \mathbb{Z}$ for $z = 0$ whilst $m \in \text{even}$ for $z = 1$. This difference is a result of their being only one $z = 1$ lattice sites for every two $z = 0$ lattice sites, see figure 6.4(a). This in turn is due to their being two dispersive bands and only a single flat band. In the cross-stitch lattice there are equal number of flat and dispersive bands.

The amplitudes $\psi(m, n)^z$, as in the cross-stitch case, define the probability to find the two particles at lattice sites (m, z) and (n, z) . The mixed amplitude, $\psi^M(m, n)$ defines the probability to find the two particles at lattice sites $(m, 1)$ and $(n, 0)$. This amplitude, as for the cross-stitch lattice, can be interpreted as describing one particle in the flat band and one particle in one of the dispersive bands. Inserting the wavefunction into the Schrödinger equation, $E|\Psi\rangle = (\hat{\mathcal{H}}_0 + \hat{\mathcal{H}}_U)|\Psi\rangle$, yields the

following eigenvalue problem for the amplitudes

$$E \begin{bmatrix} \psi^0(m, n) \\ \psi^1(m, n) \\ \psi^M(m, n) \end{bmatrix} = \begin{bmatrix} H_{00} & \delta_{m,n} \frac{U}{2} & 0 \\ \delta_{m,n} \frac{U}{2} & H_{11} & 0 \\ 0 & 0 & H_{MM} \end{bmatrix} \begin{bmatrix} \psi^0(m, n) \\ \psi^1(m, n) \\ \psi^M(m, n) \end{bmatrix}. \quad (6.36)$$

The eigenvalue equation has the same form to that obtained in the cross-stitch analysis with firstly, the mixed probability amplitudes $\psi^M(m, n)$ uncoupled from $\psi^{0,1}(m, n)$ and secondly, the probability amplitudes $\psi^0(m, n)$ and $\psi^1(m, n)$ are again only linked together by the interaction. In contrast to the cross-stitch case however, $\psi^1(m, n)$ is only defined for m and n both even.

6.3.1.1 One flat-band particle

In close analogy with the cross-stitch lattice the mixed probability amplitude, $\psi^M(m, n)$, is decoupled from the rest of the Hilbert space. The eigenvalue equation for $\psi^M(m, n)$ is

$$\begin{aligned} E\psi^M(m, n) &= H_{MM}\psi^M(m, n) \\ &= -\sqrt{2}J\left(\psi^M(m, n+1) + \psi^M(m, n-1)\right) + \frac{t}{2}(-1)^n\psi^M(m, n) + U\psi^M(m, n)\delta_{m,n} \end{aligned} \quad (6.37)$$

where $m \in \text{even}$ and $n \in \mathbb{Z}$. Within this mixed space the eigenvalue equation for different values of m are uncoupled. In the case of an infinite lattice or periodic boundary conditions the eigenvalue equation for each m becomes identical and is equivalent to a one dimensional superlattice with an impurity located at the centre of the lattice, site 0. In the same way as was discussed for the cross-stitch lattice this can be interpreted as one particle being loaded into the flat-band localised state f_0^\dagger which is infinitely heavy and hence fixed and the other particle scatters off this particle. The scattering and bound state eigenfunctions of this scattering problem have already been obtained in ref. [124] where it is found that there are two scattering bands and two bound states, one with energy below the lowest scattering

continuum and one in the gap.

6.3.1.2 Two flat-band particles

The subspace in which both particles are in the flat band, $\psi^1(m, n)$, is connected by the interaction to the states in which neither particle is located in the flat band, $\psi^0(m, n)$. The Schrödinger equation governing this subspace is equivalent to a single particle moving in a quasi-three-dimensional lattice composed of a stack of two square lattices but where the upper square lattice has a lattice constant of twice that of the lower. A visualisation of this lattice is shown in figure 6.4(b) where the solid lines represent hoppings of strength $\sqrt{2}J$ and the dashed lines represent interaction-induced hoppings. Note that for $z = 0$ we have $(m, n) \in \mathbb{Z}$ whilst $(m, n) \in \text{even}$ for $z = 1$. The single-particle Schrödinger equation can be written as

$$-\tilde{J} \sum_{\mu=-1,1} [\psi^0(m + \mu, n) + \psi^0(m, n + \mu)]\delta_{z,0} + \delta_{z,0}\epsilon_0^{m,n}\psi^0(m, n) + \delta_{z,1}\epsilon_1^{m,n}\psi^1(m, n) + \frac{U}{2}\delta_{m,n}\psi(m, n, z + 1) = E\psi^z(m, n) \quad (6.38)$$

where $\tilde{J} = \sqrt{2}J$ is the hopping amplitude and $\epsilon_0^{m,n} = -\frac{t}{2}((-1)^m + (-1)^n) + \delta_{m,n}\frac{U}{4}(3 - (-1)^m)$ and $\epsilon_1^{m,n} = 3t + \delta_{m,n}U/2$ determine the sublattice energies of the $z = 0$ and $z = 1$ lattices respectively. This Schrödinger equation bears a close resemblance to the one obtained in the cross-stitch analysis with a few important differences. Firstly, the $z = 0$ lattice has a non-trivial sublattice energy, first term of $\epsilon_0^{m,n}$. Secondly, the interaction between the particles, which is encoded in the sublattice energies of the diagonal lattice sites ($m = n$), takes different values for odd and even sites, second term of $\epsilon_0^{m,n}$. The bipartite nature of the $z = 0$ diagonal lattice sites originates due to an interaction whose strength depends on whether the two particles are on even or odd lattices sites. This can be seen in Eq. (6.34) where the pre-factor of the $(\hat{g}^\dagger)^2\hat{g}^2$ term is $U/4$ while it is $U/2$ for $(\hat{c}^\dagger)^2\hat{c}^2$.

6.3.2 Bethe ansatz

In principle Eq. (6.38) could be recast in a Fano-Anderson type equation as was done for the cross-stitch lattice. In practice, however, the eigenstates of the $z = 0$ lattice do not have a simple analytical form which makes the Green's function approach much more complicated. A different approach to the problem is to use a modified Bethe ansatz to find analytical forms for the eigenstates. In this section this modified Bethe ansatz approach is used to investigate the presence of interaction-induced bound states. A Schrödinger equation with a form very close to that of Eq. (6.38) has already been solved in ref. [125]. In that work the authors investigate the interaction of two particles in a one dimensional superlattice using a modified Bethe ansatz. The connection between the two models can be strengthened by using Eq. (6.38) to rewrite $\psi^1(m, m)$ in terms of $\psi^0(m, m)$ leading to an effective two-dimensional equation

$$-\tilde{J} \sum_{\mu=-1,1} [\psi(m + \mu, n) + \psi(m, n + \mu)] - \frac{t}{2} [(-1)^m + (-1)^n] \psi(m, n) + \delta_{m,n} \left[\frac{U}{2} (1 - (-1)^m) + \frac{\mathcal{U}}{2} (1 + (-1)^m) \right] \psi(m, n) = E \psi(m, n) \quad (6.39)$$

where $\mathcal{U} = \frac{U}{2} \left(1 + \frac{U/2}{(E - 3t - U/2)} \right)$ depends on the energy E .

The eigenstates of this two-dimensional Schrödinger equation can be classified into extended Bloch-like waves where the particles scatter off one another and localised states where the particles are bound together by the interaction. The scattering states, for a finite range interaction, have an energy which is just the sum of the single-particle energies of both particles [125]. Solving eq. (6.31) yields the single-particle energy spectrum which consists of two bands given by $\epsilon_s(k) = (-1)^s \sqrt{(2\tilde{J} \cos(k))^2 + (t/2)^2}$, where $s = \{1, 2\}$ is the band index. Conse-

quently, the allowed eigenenergies of the scattering states are given by

$$E_{s_1,s_2,k_1,k_2} = \epsilon_{s_1}(k_1) + \epsilon_{s_2}(k_2) = (-1)^{s_1} \sqrt{(2\tilde{J} \cos(k_1))^2 + (t/2)^2} + (-1)^{s_2} \sqrt{(2\tilde{J} \cos(k_2))^2 + (t/2)^2} \quad (6.40)$$

where $s_{1,2}$ and $k_{1,2}$ denote the band indices and allowed quasi-momenta of the non-interacting particles. In ref. [125] the explicit form for the scattering states are found by invoking a periodically modulated generalisation of the two-body Bethe ansatz

$$\Psi_B(m, n) = \Psi_0(m, n) + B\Psi_F(m, n) + C\Psi_1(m, n) \quad (6.41)$$

where $\Psi_{0,F} = \hat{O}_{S,A}(\phi_{k1,s1}(m)\phi_{k2,s2}(n)e^{i(k_1 m + k_2 n)})$ and $\hat{O}_{S,A}$ are the symmetrization and anti-symmetrization operators respectively and $\phi_{k,s}(m)$ are the real-space single particle Bloch functions, obtained by solving eq. (6.31) with periodic boundary conditions. The extra wave, Ψ_1 , is parameterised by the quasi-momenta, $k'_{1,2}$, which can be complex, and has a general form given by

$$\begin{aligned} \Psi_1^{k'_1, k'_2}(m, n) = & [\theta(m - n)\phi_{k'_1, s'_1}(m)\phi_{k'_2, s'_2}(n)e^{i(l_1 m + l_2 n)} \\ & + \tilde{\theta}(m - n)\phi_{k'_1, s'_1}(n)\phi_{k'_2, s'_2}(m)e^{i(l_1 n + l_2 m)}]e^{-|\nu||m - n|} \end{aligned} \quad (6.42)$$

where $k'_{1,2} = l_{1,2} \pm i\nu$ and $\theta(\tilde{\theta})$ is the step function being zero (one) at $m - n = 0$. The extra wave and $\Psi_{0,F}$ are defined as having the same total quasi-momentum and the same asymptotic energy, i.e.

$$\begin{aligned} k_1 + k_2 = & K = k'_1 + k'_2, \\ E_{s_1,s_2,k_1,k_2} = & E_{s'_1,s'_2,k'_1,k'_2} \end{aligned} \quad (6.43)$$

The form of the ansatz and the constraints of eq. (6.43) ensure that the Schrödinger equation for $m \neq n$ is satisfied. In order to satisfy the Schrödinger equation for $m = n$ the ansatz is substituted into Eq. (6.39) at $m = n$ even and odd, thereby obtaining a set of two linear equations in B and C that can be solved. In the next

section this methodology will be used to show the existence of bound states in the continuum.

6.3.3 Bound state in the continuum

In the presence of a non-zero interaction the eigenstates of the two-body problem can be classified into two types consisting of extended scattering states and bound states. As was discussed in the previous section the eigenenergies of the scattering states form energy bands which are given by the sum over all the particles of the allowed single-particle energies. Consequently, a bound state can be classified by whether its energies lies within or outwith one of these bands. The former of these is termed a bound state in the continuum (BIC) and these states have generated interest since almost the beginning of quantum mechanics [109, 136]. Fundamentally, these bound states are wave phenomena and so have been observed in both optical [69, 95] and acoustic settings [18, 92], see ref. [56] for a review. In terms of few-body systems on a lattice BICs have been theoretically predicted to occur in both static [140] and driven systems [82]. The underlying mechanism at the heart of these few-body proposals is the presence of an impurity lattice site around which the bound state forms. In the diamond lattice however, BICs can form without an impurity but instead relies on the differing interaction strengths on odd and even lattice sites to sustain it. In order to show the presence of the BIC a fermionized ansatz is used

$$\Phi = B\Psi_F + \Psi_1 \quad (6.44)$$

with $k_2 = K - k_1$ $k'_{1,2} = K/2 + \pi/2 \pm i\nu$ and $s_1 = s_2 = s'_1 = s'_2 = s$. The requirement that both components of the ansatz have the same asymptotic energy gives a relationship between the energy of the ansatz, denoted E_F and given by Eq. (6.40), and the ansatz parameters K , k_1 and ν . The equations for $m = n$ odd and even can then be used to solve, for a fixed K , the value of E_F and B that allow Φ to be a solution.

The fermionized ansatz is not a BIC as it still contains the extended Bloch-like wave Ψ_F but if, however, for some value of K the B coefficient becomes zero then

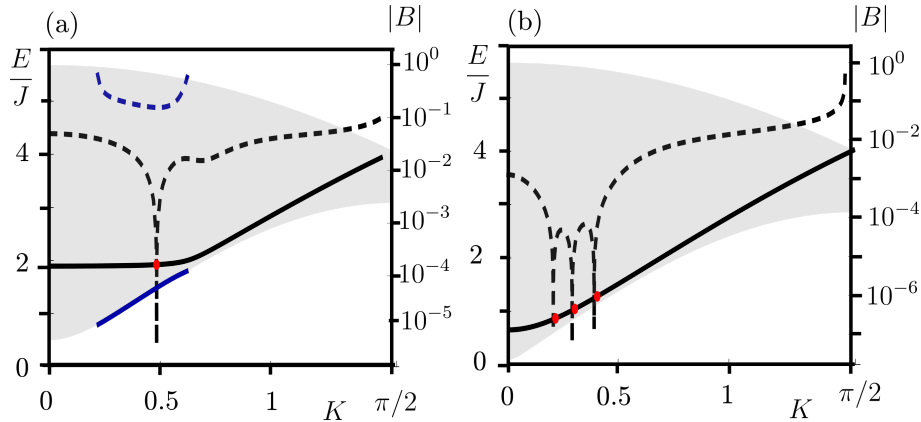


Figure 6.5: Interaction induced bound states in the continuum. The shaded region denote the scattering continuum and the solid lines indicate the energy of the eigenfunctions that take the form Φ_F which is a superposition of scattering and bound state parts. The dashed lines indicate the scattering contribution to the wavefunction which means that at the zeros bound states in the continuum are formed, red dots. Figures (a) and (b) correspond to the parameters $U/J = 0.7$, $t/J = 0.5$ and $U/J = 0.7$, $t/J = -0.063$ respectively. Note that a simultaneous flip of the sign of U and t only flips the sign of the energy and that the figures are symmetric with respect to $K = 0$.

a bound state in the continuum would be formed. There are numerous different possible scenarios that are realisable by tuning the strength and signs of U and t . In fig. 6.5 two examples are shown with the grey region indicating a band of the scattering continuum whilst the solid black and blue lines denote E_F , i.e. states which have the form of the fermionized ansatz Φ . The dashed lines give the absolute value of the B coefficient which indicates how much of the scattering state Ψ_F is contained in the ansatz. The K values for which B is exactly zero are indicated by the red dots and hence these dots show the BICs. In figure (a) which corresponds to the parameters $U/J = 0.7$ and $t/J = 0.5$ there is only a single bound state in the continuum whilst for $U/J = 0.7$ and $t/J = -0.063$ there are three bound states. Furthermore, for these latter parameters the contribution from the scattering state for $K \approx [0.2, 0.4]$, i.e. between the red dots, is less than 10^{-4} which indicates a quasi-bound state band in the continuum. The number of BICs observed is very sensitive to the parameters U/J and t/J and so future work mapping out the BIC number as a function of these parameters could be of interest.

6.3.4 Bound states

The system also supports bound states which have an energy outside any of the scattering continua, so called bound states outside the continuum (BOC). As was mentioned in the previous section the Schrödinger equation is closely related to the ionic Hubbard model discussed in ref. [125] and consequently the real space bound states may be found using the same methodology used there. In that reference the bound states are separated into two types: type 1 bound states which have energies above or below all the scattering bands and type 2 bound states that lie in the band gaps between the scattering bands. In this section the focus will be on the type 1 bound states as they show particularly interesting behaviour. In accordance with ref. [125] the following ansatz is used for the wave functions

$$\Psi(m, n) = \Psi_1^{k_1, k_2}(m, n) + B\Psi_1^{k'_1, k'_2}(m, n) \quad (6.45)$$

where Ψ_1 is the extra wave given by Eq. (6.42) and $k_{1,2} = K/2 \pm i\nu_1$ and $k'_{1,2} = (K+\pi)/2 \pm i\nu_2$. The requirement that the two wavefunctions have asymptotically the same energy, denoted E_B , implies that for a given K and E_B the decay parameters $\nu_{1,2}$ become fixed. Inserting the ansatz into the Schrödinger equation for $m = n$ odd and even gives two equations for the coefficient B that depend on the energy of the bound state, E_B , which is as yet unknown. In order to be a valid solution the two B coefficients must be made equal by varying E_B which, upon equality, yields the energy of the bound state.

In this section the focus will be the regime where all the parameters of the Hamiltonian are in competition: $U/J = [0, 10]$ and $t/J = [1, 2]$ (note that flipping the sign of both U and t does not change the shape of the spectrum, only its sign). In this parameter regime there can be at most two bound state bands with an energy greater than any of the scattering bands. The lower energy bound state band shows an interesting resonance behaviour whereby for certain values of U and t the band becomes almost dispersionless. In order to characterise the flatness of a band the bandwidth, $B_W = E_B^{\max} - E_B^{\min}$, is used where $E_B^{\max/\min}$ are the maximum and

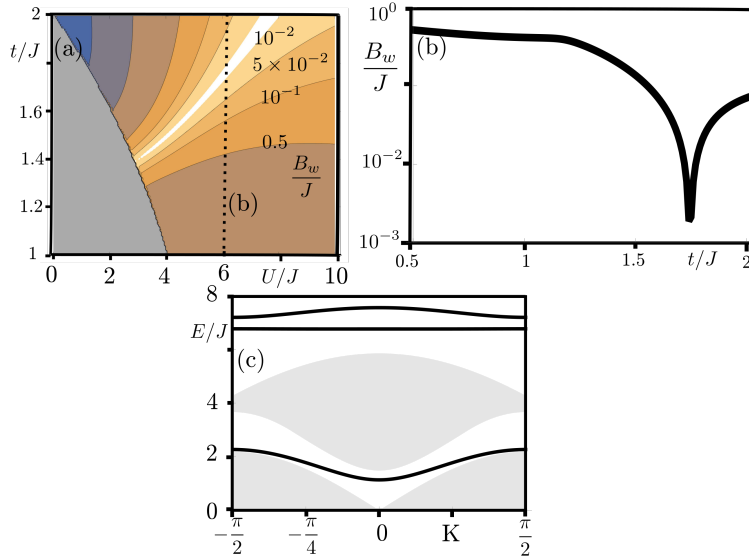


Figure 6.6: The diamond lattice for certain values of U/J and t/J can support two bound states bands that have an energy above all the scattering bands. The lower energy band can become almost flat. (a) shows the bandwidth of the lower band as function of the sublattice energy t and the interaction strength U . The white region indicates where the bandwidth, B_W , is less than $10^{-2}J$. The grey region indicates the parameters for which the lower energy band is not complete, i.e. for some K the bound state band enters the continuum. Figure (b) shows a cut through (a) as indicated by the dotted line. Figure (c) shows an example spectrum for the parameters $U/J = 4$ and $t/J = 1.492$ and the flat band is clearly visible.

minimum eigenenergies in that bound state band.

The resonant behaviour of the bandwidth is shown in fig. 6.6(a) which shows the numerically calculated bandwidth of the lower energy band with the white region showing where the bandwidth, B_W , is less than $10^{-2}J$. The gray region around the origin shows the region where the lower bound state band is not complete, i.e. the band enters the continuum at some K . The resonant behaviour is further shown in fig. (b) which shows the bandwidth for a cut through the parameter space marked by the dotted line in (a) and illustrates the sharp reduction in bandwidth that occurs as the coupling t is varied. An example spectrum for the case in which all the parameters of the Hamiltonian are comparable, $U/J = 4$ and $t/J = 1.492$, is shown fig. (c) where the bound state bands are shown by black lines and the gray shaded regions indicate the scattering bands. The presence of a quasi-flat band is clearly seen. A simple effective model that captures this resonance behaviour can be obtained by realising that for a flat band the energy dependent effective interaction, \mathcal{U} , discussed in Eq. (6.39) is a constant for every state within the

flat band. Therefore, in order to simplify the analysis the effective interaction is replaced by gU where g is a tunable constant. This effective model fails to describe the scattering bands or any of the dispersive bound state bounds but for certain values of g shows a bound state band that becomes almost flat.

6.4 Chapter summary

In this chapter we have considered two interacting particles in the cross-stitch and diamond lattices. The single-particle energy spectra of these lattices exhibit a dispersionless flat band and closely related compact localised eigenstates which appear due to destructive interference. A transformation based upon these localised states partitions the two-body Hilbert space into independent sectors depending upon the number of particles occupying the flat band. In the case of one particle occupying the flat band the problem is equivalent to a one-dimensional scattering model where the dispersive particle scatters off the infinitely heavy flat-band particle. In the alternative case of zero or two particles occupying the flat band the problem is mapped onto a single particle moving in a quasi-three-dimensional lattice. In the case of the cross-stitch lattice the problem is exactly solved using Green's functions techniques whilst for the diamond lattice a modified Bethe ansatz is used to show the existence of a number of interesting phenomena such as bound states in the continuum and a quasi-flat bound state band.

Chapter 7

Conclusion and future work

The main topic of this thesis has been the development of theoretical models to explore lattice-based transport phenomena for both single-particle and interacting two-particle systems. This work involved both driven and static situations and covered a range of different lattice geometries. Whilst the analysis conducted was primarily centred around the experimental platform of coupled optical waveguides, as this technique was often used to implement many of the models considered, the results obtained are of interest to a wide audience of researchers in fields such as quantum optics, photonics, cold atomic gases and condensed matter physics. In addition, the experimental work presented in this thesis proves the capabilities of the photonic system as a powerful simulator of quantum particles in a lattice.

Here we summarise the main topics discussed in this work. In Chapter 2 a brief theoretical introduction to coupled optical waveguide arrays was presented. The Schrödinger-like paraxial equation that governs the propagation of light waves within these systems was derived and it was shown how a coupled-mode analysis of the photonic lattice emulates the tight-binding models used in condensed matter models. In Chapter 3, experimental and theoretical results were presented for the Lieb lattice that showed a novel type of particle localisation that does not rely on disorder, non-linearity or external forces. The trapping is the result of destructive interference that prevents the localised state from expanding. Remarkably, it was shown that this effect persists in the presence of arbitrary strength disorder in the tunnelling strengths. In Chapter 4, a new technique for simulating a particle

in a lattice subject to a magnetic field using coupled optical waveguides was discussed. This novel approach involved utilising the ability present in laser-written waveguides to individually control waveguide placement to inhomogeneously bend the waveguides along the propagation direction. A theoretical description of such a system was given in terms of an effective time-independent Floquet Hamiltonian that to leading order exactly reproduced the iconic Hofstader-Harper model. It was shown through simulation that the inhomogeneously bent waveguide array very accurately reproduced the expected dynamics of a particle subject to a magnetic field. In Chapter 5, a novel type of edge mode was experimentally demonstrated using a slowly-driven photonic lattice. These edge modes, known as anomalous topological modes, are unique to driven systems and can exist even if all the topological invariants that are used to characterise static systems are zero. The effect on these edge modes stemming from both disorder in the bond strengths and in the onsite energies was investigated. In chapter 6, the dynamics of two interacting particles in the cross-stitch and diamond lattices was discussed. These geometries both feature a flat energy band and the absence of any kinetic energy terms in these bands means the dynamics are generated solely by the interaction between the particles. In the case of the cross-stitch lattice the problem was mapped onto the exactly solvable Fano-Anderson model. In the case of the diamond lattice the problem was studied via a Bethe ansatz approach and the existence of bound states in the continuum and a quasi-flat bound state band were explicitly shown.

7.0.1 Future work

In each of the chapters contained in this thesis there is scope for future work and in this section we highlight some of the most promising. It is a well established result that the flat band in the Lieb lattice persists even in the presence of a magnetic field [6, 39]. Furthermore, it can be shown numerically that, as in the flux free case, this flat band is resistant to disorder in the tunnelling strengths. This is in contrast to this result for the Kagome lattice which, like Lieb, hosts a flat band, only has nearest neighbour couplings and has 3 lattice sites per unit cell. This geometry, for certain

values of magnetic flux, features a flat energy band but yet this flat band is not robust to disordering of the bond strengths. The disparity in the reaction of these lattices to disorder is noteworthy and uncovering the underlying cause could allow flat-band lattices to be classified by their response to disorder. The potential for generating a magnetic flux, as discussed in chapter 4, opens a new range of possibilities for photonic lattices to explore. Combining this potential with the ability contained within these systems to tailor lattice geometries, incorporate non-linearities [72] and engineer external forces [64] presents many interesting future avenues of research. The demonstration of anomalous edge modes discussed in chapter 5 opens up the possibilities to investigate similar phenomena in the presence of nonlinearity and disorder. The two-particle physics discussed in chapter 6 present many possible extensions. Firstly, there exist other lattices such as the 1D pyrochlore lattice [29] that could be treated using a similar analysis to that conducted in chapter 6. The 1D pyrochlore lattice has an energy spectrum consisting of 2 flat bands and 2 dispersive bands. The presence of multiple flat bands could lead to potentially interesting interaction induced dynamics. A further extension of the work conducted could be to develop the analysis for the cross-stitch and diamond lattice to include a nearest neighbour interaction term, the so called extended Bose-Hubbard model [22, 127]. The addition of an extra interaction strength gives an additional tunable parameter which could lead to potentially interesting physics.

Appendix A

Derivation of inhomogeneous bending couplings

As discussed in the chapter 4 the effect of the inhomogenous bending is contained in the coupling integrals $t_{a,m}^{n,b}$. The dominant contribution to this integral can be written as:

$$t_{a,m}^{n,b} = e^{2ip(\dot{x}_0(x_{a,b}-x_{m,n}+x_{a,b}^0-x_{m,n}^0)+\dot{y}_0(y_{a,b}^0-y_{m,n}^0))} e^{\int_0^z \left(2ip\dot{x}_0(\dot{x}_{m,n}-\dot{x}_{a,b}) + ip(\dot{x}_{m,n}^2 - \dot{x}_{a,b}^2) \right)} \\ \frac{1}{N\lambda} \int_{-\infty}^{\infty} \int_{-\infty}^{\infty} dx dy e^{2ip \left((x-x_{m,n}^0-x_0-x_{m,n})\dot{x}_{m,n} - (x-x_{a,b}^0-x_0-x_{a,b})\dot{x}_{a,b} \right)} \\ u[x - x_{a,b}^0 - x_0 - x_{a,b}, y - y_{a,b} - y_0] V_0[x - x_{a,b}^0 - x_0 - x_{a,b}, y - y_{a,b} - y_0] \\ u[x - x_{m,n}^0 - x_0 - x_{m,n}, y - y_{m,n}^0 - y_0]. \quad (\text{A.1})$$

The terms outside the integral are just modifications of the phase of the integral and terms of this form appear also in homogeneous shaking. The differences to the homogeneous case are the appearance of an x dependent phase term in the integrand and that the overlap between the modes calculated by this integral could change with propagation distance. Therefore, to study the effects of these terms we initially focus just on the integral, i.e. the last two lines of Eqn. A.1. This integral can be rewritten in terms of new variables $x' = x - x_0 - (x_{a,b}^0 + x_{a,b})$ and

$y' = y - y_{a,b} - y_0$ as:

$$\tilde{I} = \frac{1}{N\lambda} e^{2ip\dot{x}_{m,n}(x_{a,b}-x_{m,n}+x_{a,b}^0-x_{m,n}^0)} \int_{-\infty}^{\infty} \int_{-\infty}^{\infty} dx' dy' e^{2ipx'(\dot{x}_{m,n}-\dot{x}_{a,b})} u[x', y'] V_0[x', y'] u[x' - (x_{m,n}^0 - x_{a,b}^0) - (x_{m,n} - x_{a,b}), y' + y_{a,b}^0 - y_{m,n}^0], \quad (\text{A.2})$$

where the new phase term outside the integral is a result of this change of variables. Making the assumption that the modes and refractive index profile have a circular symmetry the integral can then be rewritten using normalised polar coordinates: (R, θ) , where $R = \frac{r}{\rho}$ and ρ is the half-width of V_0 .

$$\tilde{I} = e^{2ip\dot{x}_{m,n}(x_{a,b}-x_{m,n}+x_{a,b}^0-x_{m,n}^0)} \rho^2 \int_0^{\infty} \int_0^{2\pi} R dR d\theta e^{2ip\rho R \cos(\theta)(\dot{x}_{m,n}-\dot{x}_{a,b})} u[R] V_0[R] u[R_1], \quad (\text{A.3})$$

The normalised separation between the two waveguides, R_1 , can be written as:

$$R_1 = \sqrt{(R \cos(\theta) + \alpha_0 + \alpha(z))^2 + (a_0 - R \sin(\theta))^2}$$

where $\alpha(z) = \frac{1}{\rho}(x_{m,n}(z) - x_{a,b}(z))$, $\alpha_0 = \frac{1}{\rho}(x_{m,n}^0 - x_{a,b}^0)$ and $a_0 = \frac{1}{\rho}(y_{m,n}^0 - y_{a,b}^0)$.

In the following sections we will limit our analysis to a square lattice geometry and only consider bending profiles of the form: $x_{m,n}(z) = x_n = A \sin(\omega z + \phi_n)$. The assumption that the shaking depends only on the y coordinate of the lattice means that for x-hoppings the integrand of Eq. (A.3) becomes z independent whilst the assumption of a square geometry implies that $\alpha_0 = 0$ for y-hoppings. The particular form of bending profile used means that the argument of the exponential can be written as

$$2K_x \frac{R \cos(\theta)}{a_0} \sin\left(\frac{1}{2}(\phi_b - \phi_n)\right) \sin\left(\omega z + \frac{1}{2}(\phi_b + \phi_n)\right). \quad (\text{A.4})$$

The dimensionless variable $K_x = 2pA\omega a$ for typical experimental parameters is of order 1. The presence of the $V_0[R]$ in the integrand of Eq. (A.3) means that the majority of the weight of the integral will lie in the region $0 \leq R \leq 1$. In this range the amplitude of Eq. (A.4) will be small which subsequently implies that the

exponential in the integrand of eqn. A.3 may be expanded to first order to give

$$\tilde{I} = e^{2ip\hat{x}_{m,n}(x_{a,b}-x_{m,n}+x_{a,b}^0-x_{m,n}^0)} \left(I_1 + i\epsilon(z)I_2 \right), \quad (\text{A.5})$$

$$I_1 = \frac{\rho^2}{\lambda N} \int_0^\infty \int_0^{2\pi} R dR d\theta u[R] V_0[R] u[R_1], \quad (\text{A.6})$$

$$I_2 = \frac{\rho^2}{\lambda N} \int_0^\infty \int_0^{2\pi} R^2 dR d\theta \cos(\theta) u[R] V_0[R] u[R_1], \quad (\text{A.7})$$

$$\epsilon(z) = \frac{2K_x \sin(\frac{1}{2}(\phi_b - \phi_n)) \sin(\omega z + \frac{1}{2}(\phi_b + \phi_n))}{a_0} \quad (\text{A.8})$$

A.1 Integrals

To proceed further with the integral I_2 we assume that the waveguide separations are much larger than ρ , the half-width of V_0 . This assumption means that in the region $0 \leq R \leq 1$ the mode $u[R_1]$ has the approximate form $u[R_1] = UK_0(WR_1)$, where K_0 is the modified Bessel function of the second kind and W and U are constants of order 1. This function is thereby slowly varying within this region and so we expand $u[R_1]$ to second order around $R = 0$. This expansion allows the integration over θ to be performed.

$$\epsilon(z)I_2 = \frac{AK_x \sin^2(\frac{\phi_b - \phi_n}{2}) \sin(2\omega z + \phi_b + \phi_n)}{a\sqrt{a_0^2 + \alpha^2}} K_1(\sqrt{a_0^2 + \alpha^2}) \frac{2\pi\rho^2}{\lambda N} \int_0^\infty R^3 dR u[R] V_0[R] \quad (\text{A.9})$$

This can be made more meaningful by making the approximation

$$C_0 \approx \frac{\rho^2 K_0(a_0)}{\lambda N} \int_0^\infty \int_0^{2\pi} R dR d\theta u[R] v[R] \approx \frac{\rho^2 K_0(a_0)}{\lambda N} \int_0^\infty \int_0^{2\pi} R^3 dR d\theta u[R] V_0[R]. \quad (\text{A.10})$$

This rough estimation allows Eq. (A.9) to be approximated as:

$$\epsilon(z)I_2 = \frac{AK_x \sin^2(\frac{\phi_{a,b} - \phi_{m,n}}{2}) \sin(2\omega z + \phi_{a,b} + \phi_{m,n})}{a\sqrt{a_0^2 + \alpha^2} K_0(a_0)} K_1(\sqrt{a_0^2 + \alpha^2}) C_0. \quad (\text{A.11})$$

Making the further assumption that $a_0 \gg \alpha(z)$ simplifies this result to:

$$\epsilon(z)I_2 \approx i \frac{\rho A K_x \sin^2(\frac{\phi_b - \phi_n}{2})}{a^2} \sin(2\omega z + \phi_{a,b} + \phi_{m,n}) C_0. \quad (\text{A.12})$$

The amplitude of this term is much smaller, for typical experimental parameters, than the static coupling constant and so this term only represents a small correction to the dynamics. This term will in practice be sub-dominant to other neglected effects such as next-nearest neighbour couplings.

The integral I_1 is of the form of a standard coupling integral but one where the waveguide-waveguide separation is not necessarily constant with z . However, at any particular value of z the integral can be performed and typically the result is exponentially dependent upon the waveguide-waveguide separation. Therefore, in the case of x-hoppings we obtain $I_1 = \kappa_0 e^{-\frac{a}{\tau}}$, where κ_0 and τ are constants. The y-hopping case by contrast depends upon z :

$$I_1 = \kappa_0 e^{-\frac{1}{\tau} \sqrt{a^2 + (\rho\alpha(z))^2}} \quad (\text{A.13})$$

Assuming that the amplitude of the shaking is small compared to the lattice constant, a , then I_1 can be simplified to the form:

$$I_1 \approx \kappa_0 \exp \left[-\frac{1}{\tau} \left(a + \frac{A^2}{a} \sin^2((\phi_m - \phi_a)/2) \right) - \frac{A^2}{a\tau} \sin^2((\phi_m - \phi_a)/2) \cos(2\omega z + \phi_m + \phi_a) \right] \quad (\text{A.14})$$

The knowledge of this integral combined with the assumed forms for $x_0, x_{m,n}$ and y_0 allows the couplings along the x and y directions to be written explicitly as :

$$t_{m,m+1}^n = \exp[iK_x \cos(\omega z + \phi_n) + i\omega z] \kappa_0 e^{-\frac{a}{\tau}}, \quad (\text{A.15})$$

$$\begin{aligned} t_{m,m}^{n,n+1} = & \exp[iF_0 + iK_y \cos(\omega z) + iP \sin(\omega z + \gamma) \\ & + iQ \sin(2\omega z + \Phi)] I_1, \end{aligned} \quad (\text{A.16})$$

$$\begin{aligned} K_x &= 2pA\omega a, \\ F_0 &= \frac{A}{a} \left(\cos(\phi_{n+1}) - \cos(\phi_n) \right) + \frac{K_x A}{2a} \sin(\gamma^-) \left(1 + \frac{1}{2} \cos(2\gamma) \right), \\ K_y &= 2pB\omega a, \\ P &= \frac{2A}{a} \sin(\gamma^-), \\ Q \sin(2\omega z + \Phi) &= \frac{K_x A}{2a} \left(\sin(2\omega z + 2\gamma) - \frac{1}{4} \sin(2\omega z + 2\phi_{n+1}) - \frac{3}{4} \sin(2\omega z + 2\phi_n) \right), \\ \gamma &= \frac{1}{2}(\phi_n + \phi_{n+1}), \\ \gamma^- &= \frac{1}{2}(\phi_{n+1} - \phi_n), \\ C_0 &= \kappa_0 e^{-\frac{a}{\tau}} \end{aligned} \quad (\text{A.17})$$

In the high-frequency modulation regime, $\omega \gg C_0$, effective tunnelings that are independent of z can be obtained by averaging Eqns. A.15 and A.16 over one period. The Jacobi-Anger expansion,

$\exp(ix \cos(y)) = \sum_{n=-\infty}^{\infty} i^n \mathcal{J}_n(x) e^{iny}$, allows the couplings to be written as

$$(t_{m,m+1}^{n,n})_{eff} = C_0 \mathcal{J}_1(K_x) i e^{-i\phi_n} \quad (\text{A.18})$$

$$\begin{aligned} (t_{m,m}^{n,n+1})_{eff} = & \kappa_0 e^{-\frac{1}{\tau} \left(a + \frac{A^2}{a} \sin^2((\phi_m - \phi_a)/2) \right)} e^{iF_0} \\ & \sum_{q=-\infty}^{\infty} (-1)^q \mathcal{J}_{2q}(\Gamma) \mathcal{I}_q \left(\frac{A^2}{a\tau} \sin^2((\phi_{n+1} - \phi_n)/2) \right) e^{i2q(\gamma-\delta)} \end{aligned} \quad (\text{A.19})$$

$$\Gamma = \sqrt{K_y^2 + P^2 + 2K_y P \sin(\gamma)}, \quad (\text{A.20})$$

$$\psi = \arctan\left(\frac{K_y \cos(\gamma)}{P + K_y \sin(\gamma)}\right), \quad (\text{A.21})$$

$$\delta = \arctan\left(\frac{K_y + P \sin(\gamma)}{P \cos(\gamma)}\right) \quad (\text{A.22})$$

Here \mathcal{J}_n , \mathcal{I}_n are Bessel functions of n^{th} order of the first and second modified kind respectively. The effective y tunnelings can be simplified by again assuming that amplitude of shaking is much smaller than the lattice constant. This assumption means that the argument of the I_q in eqn. (A.19) is small and so the sum will be dominated by the $q = 0$ contribution. A further simplification can be made by noting that the term e^{iF_0} in eqn. A.19 does not contribute to the flux as it cancels with its respective partner on the opposing bond upon summing round a plaquette. The effect of this term is therefore to shift the dispersion relation in quasi-momentum space by a small amount which we will neglect. These approximations simplify the y tunnelling into the form

$$(t_{m,m}^{n,n+1})_{eff} = C_0 e^{-\frac{1}{\tau} \left(\frac{A^2}{a} \sin^2((\phi_{n+1} - \phi_n)/2) \right)} \mathcal{J}_0\left(\sqrt{K_y^2 + P^2 + 2K_y P \sin(\gamma)}\right). \quad (\text{A.23})$$

Bibliography

- [1] Aidelsburger, M., Atala, M., Lohse, M., Barreiro, J. T., Paredes, B. and Bloch, I. [2013], ‘Realization of the hofstadter hamiltonian with ultracold atoms in optical lattices’, *Physical review letters* **111**(18), 185301.
- [2] Aidelsburger, M., Lohse, M., Schweizer, C., Atala, M., Barreiro, J., Nascimbène, S., Cooper, N., Bloch, I. and Goldman, N. [2015], ‘Measuring the chern number of hofstadter bands with ultracold bosonic atoms’, *Nature Physics* **11**, 162–166.
- [3] An, F. A., Meier, E. J. and Gadway, B. [2017], ‘Direct observation of chiral currents and magnetic reflection in atomic flux lattices’, *Science Advances* **3**(4), e1602685.
- [4] Anderson, P. W. [1958], ‘Absence of diffusion in certain random lattices’, *Physical review* **109**(5), 1492.
- [5] Anderson, P. W. [1961], ‘Localized magnetic states in metals’, *Physical Review* **124**(1), 41.
- [6] Aoki, H., Ando, M. and Matsumura, H. [1996], ‘Hofstadter butterflies for flat bands’, *Physical Review B* **54**(24), R17296.
- [7] Atala, M., Aidelsburger, M., Lohse, M., Barreiro, J. T., Paredes, B. and Bloch, I. [2014], ‘Observation of chiral currents with ultracold atoms in bosonic ladders.’, *Nature Physics* **10**(8).
- [8] Bauer, F. L. and Fike, C. T. [1960], ‘Norms and exclusion theorems’, *Numerische Mathematik* **2**(1), 137–141.

- [9] Bermudez, A., Schaetz, T. and Porras, D. [2012], ‘Photon-assisted-tunneling toolbox for quantum simulations in ion traps’, *New Journal of Physics* **14**(5), 053049.
- [10] Bernevig, B. A. and Hughes, T. L. [2013], *Topological insulators and topological superconductors*, Princeton University Press.
- [11] Bianco, R. and Resta, R. [2011], ‘Mapping topological order in coordinate space’, *Physical Review B* **84**(24), 241106.
- [12] Bodyfelt, J. D., Leykam, D., Danieli, C., Yu, X. and Flach, S. [2014], ‘Flatbands under correlated perturbations’, *Physical Review Letters* **113**(23), 236403.
- [13] Buluta, I. and Nori, F. [2009], ‘Quantum simulators’, *Science* **326**(5949), 108–111.
- [14] Cayssol, J., Dóra, B., Simon, F. and Moessner, R. [2013], ‘Floquet topological insulators’, *physica status solidi (RRL)-Rapid Research Letters* **7**(1-2), 101–108.
- [15] Chen, Y.-A., Nascimbène, S., Aidelsburger, M., Atala, M., Trotzky, S. and Bloch, I. [2011], ‘Controlling correlated tunneling and superexchange interactions with ac-driven optical lattices’, *Physical review letters* **107**(21), 210405.
- [16] Corrielli, G., Crespi, A., Della Valle, G., Longhi, S. and Osellame, R. [2013], ‘Fractional bloch oscillations in photonic lattices’, *Nature Communications* **4**.
- [17] Creffield, C. and Platero, G. [2010], ‘Coherent control of interacting particles using dynamical and aharonov-bohm phases’, *Physical review letters* **105**(8), 086804.
- [18] Cumpsty, N. A. and Whitehead, D. [1971], ‘The excitation of acoustic resonances by vortex shedding’, *Journal of Sound and Vibration* **18**(3), 353–369.
- [19] Dagotto, E. [1994], ‘Correlated electrons in high-temperature superconductors’, *Reviews of Modern Physics* **66**(3), 763.
- [20] Denschlag, J. H. and Daley, A. [2006], ‘Exotic atom pairs: Repulsively bound states in an optical lattice’, *arXiv preprint cond-mat/0610393* .

- [21] Derzhko, O., Honecker, A. and Richter, J. [2009], ‘Exact low-temperature properties of a class of highly frustrated hubbard models’, *Physical Review B* **79**(5), 054403.
- [22] Di Liberto, M., Recati, A., Carusotto, I. and Menotti, C. [2017], ‘Two-body bound and edge states in the extended ssh bose-hubbard model’, *The European Physical Journal Special Topics* **226**(12), 2751–2762.
- [23] Dreisow, F., Szameit, A., Heinrich, M., Pertsch, T., Nolte, S., Tünnermann, A. and Longhi, S. [2009], ‘Bloch-zener oscillations in binary superlattices’, *Physical review letters* **102**(7), 076802.
- [24] Dunlap, D. and Kenkre, V. [1986], ‘Dynamic localization of a charged particle moving under the influence of an electric field’, *Physical Review B* **34**(6), 3625.
- [25] Eckardt, A., Jinasundera, T., Weiss, C. and Holthaus, M. [2005], ‘Analog of photon-assisted tunneling in a bose-einstein condensate’, *Physical review letters* **95**(20), 200401.
- [26] Emin, D. and Hart, C. [1987], ‘Existence of wannier-stark localization’, *Physical Review B* **36**(14), 7353.
- [27] Fang, K., Yu, Z. and Fan, S. [2012], ‘Realizing effective magnetic field for photons by controlling the phase of dynamic modulation’, *Nature photonics* **6**(11), 782–787.
- [28] Fano, U. [1961], ‘Effects of configuration interaction on intensities and phase shifts’, *Physical Review* **124**(6), 1866.
- [29] Flach, S., Leykam, D., Bodyfelt, J. D., Matthies, P. and Desyatnikov, A. S. [2014], ‘Detangling flat bands into fano lattices’, *EPL (Europhysics Letters)* **105**(3), 30001.
- [30] Fölling, S., Trotzky, S., Cheinet, P., Feld, M., Saers, R., Widera, A., Müller, T. and Bloch, I. [2007], ‘Direct observation of second-order atom tunnelling’, *Nature* **448**(7157), 1029.

- [31] Fukui, T., Hatsugai, Y. and Suzuki, H. [2005], ‘Chern numbers in discretized brillouin zone: efficient method of computing (spin) hall conductances’, *Journal of the Physical Society of Japan* **74**(6), 1674–1677.
- [32] Fukuyama, H., Bari, R. A. and Fogedby, H. C. [1973], ‘Tightly bound electrons in a uniform electric field’, *Physical Review B* **8**(12), 5579.
- [33] Gao, F., Gao, Z., Shi, X., Yang, Z., Lin, X., Xu, H., Joannopoulos, J. D., Soljačić, M., Chen, H., Lu, L. et al. [2016], ‘Probing topological protection using a designer surface plasmon structure’, *Nature communications* **7**.
- [34] Garanovich, I. L., Longhi, S., Sukhorukov, A. A. and Kivshar, Y. S. [2012], ‘Light propagation and localization in modulated photonic lattices and waveguides’, *Physics Reports* **518**(1), 1–79.
- [35] Georgescu, I., Ashhab, S. and Nori, F. [2014], ‘Quantum simulation’, *Reviews of Modern Physics* **86**(1), 153.
- [36] Goldman, N., Budich, J. and Zoller, P. [2016], ‘Topological quantum matter with ultracold gases in optical lattices’, *Nature Physics* **12**(7), 639–645.
- [37] Goldman, N. and Dalibard, J. [2014], ‘Periodically driven quantum systems: effective hamiltonians and engineered gauge fields’, *Physical Review X* **4**(3), 031027.
- [38] Goldman, N., Dalibard, J., Aidelsburger, M. and Cooper, N. [2015], ‘Periodically driven quantum matter: The case of resonant modulations’, *Physical Review A* **91**(3), 033632.
- [39] Goldman, N., Urban, D. and Bercioux, D. [2011], ‘Topological phases for fermionic cold atoms on the lieb lattice’, *Physical Review A* **83**(6), 063601.
- [40] Golshani, M., Weimann, S., Jafari, K., Nezhad, M. K., Langari, A., Bahrampour, A., Eichelkraut, T., Mahdavi, S. and Szameit, A. [2014], ‘Impact of loss on the wave dynamics in photonic waveguide lattices’, *Physical Review Letters* **113**(12), 123903.

- [41] Grifoni, M. and Hänggi, P. [1998], ‘Driven quantum tunneling’, *Physics Reports* **304**(5), 229–354.
- [42] Grossmann, F., Dittrich, T., Jung, P. and Hänggi, P. [1991], ‘Coherent destruction of tunneling’, *Physical Review Letters* **67**(4), 516.
- [43] Grosso, G. and Pastori Parravicini, G. [2003], ‘Solid state physics’.
- [44] Groth, C., Wimmer, M., Akhmerov, A., Tworzydło, J. and Beenakker, C. [2009], ‘Theory of the topological anderson insulator’, *Physical Review Letters* **103**(19), 196805.
- [45] Gulácsi, Z., Kampf, A. and Vollhardt, D. [2007], ‘Exact many-electron ground states on the diamond hubbard chain’, *Physical Review Letters* **99**(2), 026404.
- [46] Guzmán-Silva, D., Mejía-Cortés, C., Bandres, M., Rechtsman, M., Weimann, S., Nolte, S., Segev, M., Szameit, A. and Vicencio, R. [2014], ‘Experimental observation of bulk and edge transport in photonic lieb lattices’, *New Journal of Physics* **16**(6), 063061.
- [47] Hafezi, M., Demler, E. A., Lukin, M. D. and Taylor, J. M. [2011], ‘Robust optical delay lines with topological protection’, *Nature Physics* **7**(11), 907.
- [48] Hafezi, M., Mittal, S., Fan, J., Migdall, A. and Taylor, J. [2013], ‘Imaging topological edge states in silicon photonics’, *Nature Photonics* **7**(12), 1001–1005.
- [49] Harper, P. G. [1955], ‘Single band motion of conduction electrons in a uniform magnetic field’, *Proceedings of the Physical Society. Section A* **68**(10), 874.
- [50] Hasan, M. Z. and Moore, J. E. [2011], ‘Three-dimensional topological insulators’, *Annu. Rev. Condens. Matter Phys.* **2**(1), 55–78.
- [51] Hatsugai, Y. [1993a], ‘Chern number and edge states in the integer quantum hall effect’, *Physical Review Letters* **71**(22), 3697.
- [52] Hatsugai, Y. [1993b], ‘Edge states in the integer quantum hall effect and the riemann surface of the bloch function’, *Physical Review B* **48**(16), 11851.

- [53] Hauke, P., Tielemans, O., Celi, A., Ölschläger, C., Simonet, J., Struck, J., Weinberg, M., Windpassinger, P., Sengstock, K., Lewenstein, M. et al. [2012], ‘Non-abelian gauge fields and topological insulators in shaken optical lattices’, *Physical Review Letters* **109**(14), 145301.
- [54] Henneberger, W. C. [1968], ‘Perturbation method for atoms in intense light beams’, *Physical Review Letters* **21**(12), 838.
- [55] Hofstadter, D. R. [1976], ‘Energy levels and wave functions of Bloch electrons in rational and irrational magnetic fields’, *Physical Review B* **14**(6), 2239.
- [56] Hsu, C. W., Zhen, B., Stone, A. D., Joannopoulos, J. D. and Soljačić, M. [2016], ‘Bound states in the continuum’, *Nature Reviews Materials* **1**, 16048.
- [57] Hu, W., Pillay, J. C., Wu, K., Pasek, M., Shum, P. P. and Chong, Y. [2015], ‘Measurement of a topological edge invariant in a microwave network’, *Physical Review X* **5**(1), 011012.
- [58] Huang, W. and Haus, H. A. [1990], ‘Self-consistent vector coupled-mode theory for tapered optical waveguides’, *Journal of Lightwave Technology* **8**(6), 922–926.
- [59] Hubbard, J. [1963], Electron correlations in narrow energy bands, in ‘Proceedings of the royal society of London A: mathematical, physical and engineering sciences’, Vol. 276, The Royal Society, pp. 238–257.
- [60] Huber, S. D. and Altman, E. [2010], ‘Bose condensation in flat bands’, *Physical Review B* **82**(18), 184502.
- [61] Hügel, D. and Paredes, B. [2014], ‘Chiral ladders and the edges of quantum Hall insulators’, *Physical Review A* **89**(2), 023619.
- [62] Jaksch, D. and Zoller, P. [2003], ‘Creation of effective magnetic fields in optical lattices: the Hofstadter butterfly for cold neutral atoms’, *New Journal of Physics* **5**(1), 56.

- [63] Jotzu, G., Messer, M., Desbuquois, R., Lebrat, M., Uehlinger, T., Greif, D. and Esslinger, T. [2014], ‘Experimental realization of the topological haldane model with ultracold fermions’, *Nature* **515**, 237–240.
- [64] Khomeriki, R. and Flach, S. [2016], ‘Landau-zener bloch oscillations with perturbed flat bands’, *Physical Review Letters* **116**(24), 245301.
- [65] Kitagawa, T., Berg, E., Rudner, M. and Demler, E. [2010], ‘Topological characterization of periodically driven quantum systems’, *Physical Review B* **82**(23), 235114.
- [66] Kitagawa, T., Broome, M. A., Fedrizzi, A., Rudner, M. S., Berg, E., Kasal, I., Aspuru-Guzik, A., Demler, E. and White, A. G. [2012], ‘Observation of topologically protected bound states in photonic quantum walks’, *Nature Communications* **3**.
- [67] Klitzing, K. v., Dorda, G. and Pepper, M. [1980], ‘New method for high-accuracy determination of the fine-structure constant based on quantized hall resistance’, *Physical Review Letters* **45**(6), 494.
- [68] Kohmoto, M. [1989], ‘Zero modes and the quantized hall conductance of the two-dimensional lattice in a magnetic field’, *Physical Review B* **39**(16), 11943.
- [69] Lee, J., Zhen, B., Chua, S.-L., Qiu, W., Joannopoulos, J. D., Soljačić, M. and Shapira, O. [2012], ‘Observation and differentiation of unique high-q optical resonances near zero wave vector in macroscopic photonic crystal slabs’, *Physical Review Letters* **109**(6), 067401.
- [70] Lenz, G., Talanina, I. and De Sterke, C. M. [1999], ‘Bloch oscillations in an array of curved optical waveguides’, *Physical review letters* **83**(5), 963.
- [71] Leykam, D., Bahat-Treidel, O. and Desyatnikov, A. S. [2012], ‘Pseudospin and nonlinear conical diffraction in lieb lattices’, *Physical Review A* **86**(3), 031805.
- [72] Leykam, D. and Chong, Y. D. [2016], ‘Edge solitons in nonlinear-photonic topological insulators’, *Physical Review Letters* **117**(14), 143901.

- [73] Leykam, D., Flach, S., Bahat-Treidel, O. and Desyatnikov, A. S. [2013], ‘Flat band states: Disorder and nonlinearity’, *Physical Review B* **88**(22), 224203.
- [74] Li, J., Chu, R.-L., Jain, J. and Shen, S.-Q. [2009], ‘Topological anderson insulator’, *Physical Review Letters* **102**(13), 136806.
- [75] Lifante, G. [2003], *Integrated photonics: fundamentals*, J. Wiley.
- [76] Lindner, N. H., Refael, G. and Galitski, V. [2010], ‘Floquet topological insulator in semiconductor quantum wells’, *arXiv preprint arXiv:1008.1792*.
- [77] Lipson, A., Lipson, S. G. and Lipson, H. [2010], *Optical physics*, Cambridge University Press.
- [78] Longhi, S. [2007], ‘Bound states in the continuum in a single-level fano-anderson model’, *The European Physical Journal B-Condensed Matter and Complex Systems* **57**(1), 45–51.
- [79] Longhi, S. [2009], ‘Quantum-optical analogies using photonic structures’, *Laser & Photonics Reviews* **3**(3), 243–261.
- [80] Longhi, S. [2011], ‘Optical realization of the two-site bose–hubbard model in waveguide lattices’, *Journal of Physics B: Atomic, Molecular and Optical Physics* **44**(5), 051001.
- [81] Longhi, S. [2013], ‘Effective magnetic fields for photons in waveguide and coupled resonator lattices’, *Optics Letters* **38**(18), 3570–3573.
- [82] Longhi, S. and Della Valle, G. [2013], ‘Tamm–hubbard surface states in the continuum’, *Journal of Physics: Condensed Matter* **25**(23), 235601.
- [83] Longhi, S., Marangoni, M., Lobino, M., Ramponi, R., Laporta, P., Cianci, E. and Foglietti, V. [2006], ‘Observation of dynamic localization in periodically curved waveguide arrays’, *Physical review letters* **96**(24), 243901.
- [84] Maczewsky, L. J., Zeuner, J. M., Nolte, S. and Szameit, A. [2017], ‘Observation of photonic anomalous floquet topological insulators’, *Nature communications* **8**, 13756.

- [85] Mahan, G. D. [2013], *Many-particle physics*, Springer Science & Business Media.
- [86] Miyake, H., Siviloglou, G. A., Kennedy, C. J., Burton, W. C. and Ketterle, W. [2013], ‘Realizing the harper hamiltonian with laser-assisted tunneling in optical lattices’, *Physical review letters* **111**(18), 185302.
- [87] Mukherjee, S., Spracklen, A., Choudhury, D., Goldman, N., Öhberg, P., Andersson, E. and Thomson, R. R. [2015], ‘Observation of a localized flat-band state in a photonic lieb lattice’, *Physical Review Letters* **114**(24), 245504.
- [88] Nathan, F. and Rudner, M. S. [2015], ‘Topological singularities and the general classification of floquet–bloch systems’, *New Journal of Physics* **17**(12), 125014.
- [89] Niță, M., Ostahie, B. and Aldea, A. [2013], ‘Spectral and transport properties of the two-dimensional lieb lattice’, *Physical Review B* **87**(12), 125428.
- [90] Okamoto, K. [2010], *Fundamentals of optical waveguides*, Academic press.
- [91] Orignac, E. and Giamarchi, T. [2001], ‘Meissner effect in a bosonic ladder’, *Physical Review B* **64**(14), 144515.
- [92] Parker, R. [1966], ‘Resonance effects in wake shedding from parallel plates: some experimental observations’, *Journal of Sound and Vibration* **4**(1), 62–72.
- [93] Peierls, R. [1933], ‘Zur theorie des diamagnetismus von leitungselektronen’, *Zeitschrift für Physik A Hadrons and Nuclei* **80**(11), 763–791.
- [94] Phillips, L. G., De Chiara, G., Öhberg, P. and Valiente, M. [2015], ‘Low-energy behavior of strongly interacting bosons on a flat-band lattice above the critical filling factor’, *Physical Review B* **91**(5), 054103.
- [95] Plotnik, Y., Peleg, O., Dreisow, F., Heinrich, M., Nolte, S., Szameit, A. and Segev, M. [2011], ‘Experimental observation of optical bound states in the continuum’, *Physical Review Letters* **107**(18), 183901.

- [96] Preiss, P. M., Ma, R., Tai, M. E., Lukin, A., Rispoli, M., Zupancic, P., Lahini, Y., Islam, R. and Greiner, M. [2015], ‘Strongly correlated quantum walks in optical lattices’, *Science* **347**(6227), 1229–1233.
- [97] Qi, X.-L., Wu, Y.-S. and Zhang, S.-C. [2006], ‘General theorem relating the bulk topological number to edge states in two-dimensional insulators’, *Physical Review B* **74**(4), 045125.
- [98] Qi, X.-L. and Zhang, S.-C. [2011], ‘Topological insulators and superconductors’, *Reviews of Modern Physics* **83**(4), 1057.
- [99] Rahav, S., Gilary, I. and Fishman, S. [2003], ‘Effective hamiltonians for periodically driven systems’, *Physical Review A* **68**(1), 013820.
- [100] Rechtsman, M. C., Zeuner, J. M., Plotnik, Y., Lumer, Y., Podolsky, D., Dreisow, F., Nolte, S., Segev, M. and Szameit, A. [2013], ‘Photonic floquet topological insulators’, *Nature* **496**(7444), 196.
- [101] Roati, G., D’Errico, C., Fallani, L., Fattori, M., Fort, C., Zaccanti, M., Modugno, G., Modugno, M. and Inguscio, M. [2008], ‘Anderson localization of a non-interacting bose–einstein condensate’, *Nature* **453**(7197), 895–898.
- [102] Rudner, M. S., Lindner, N. H., Berg, E. and Levin, M. [2013], ‘Anomalous edge states and the bulk-edge correspondence for periodically driven two-dimensional systems’, *Physical Review X* **3**(3), 031005.
- [103] Schwartz, T., Bartal, G., Fishman, S. and Segev, M. [2007], ‘Transport and anderson localization in disordered two-dimensional photonic lattices’, *Nature* **446**(7131), 52.
- [104] Scully, M. O. and Zubairy, M. S. [1999], ‘Quantum optics’.
- [105] Shirley, J. H. [1965], ‘Solution of the schrödinger equation with a hamiltonian periodic in time’, *Physical Review* **138**(4B), B979.

- [106] Sias, C., Lignier, H., Singh, Y., Zenesini, A., Ciampini, D., Morsch, O. and Arimondo, E. [2008], ‘Observation of photon-assisted tunneling in optical lattices’, *Physical Review Letters* **100**(4), 040404.
- [107] Snyder, A. W. and Love, J. [2012], *Optical waveguide theory*, Springer Science & Business Media.
- [108] Sørensen, A. S., Demler, E. and Lukin, M. D. [2005], ‘Fractional quantum hall states of atoms in optical lattices’, *Physical Review Letters* **94**(8), 086803.
- [109] Stillinger, F. H. and Herrick, D. R. [1975], ‘Bound states in the continuum’, *Physical Review A* **11**(2), 446.
- [110] Strohmaier, N., Greif, D., Jördens, R., Tarruell, L., Moritz, H., Esslinger, T., Sensarma, R., Pekker, D., Altman, E. and Demler, E. [2010], ‘Observation of elastic doublon decay in the fermi-hubbard model’, *Physical Review Letters* **104**(8), 080401.
- [111] Struck, J., Weinberg, M., Ölschläger, C., Windpassinger, P., Simonet, J., Sengstock, K., Höppner, R., Hauke, P., Eckardt, A., Lewenstein, M. et al. [2013], ‘Engineering ising-xy spin-models in a triangular lattice using tunable artificial gauge fields’, *Nature Physics* **9**, 738–743.
- [112] Stuhl, B., Lu, H.-I., Aycock, L., Genkina, D. and Spielman, I. [2015], ‘Visualizing edge states with an atomic bose gas in the quantum hall regime’, *Science* **349**(6255), 1514–1518.
- [113] Szameit, A., Burghoff, J., Pertsch, T., Nolte, S., Tünnermann, A. and Lederer, F. [2006], ‘Two-dimensional soliton in cubic fs laser written waveguide arrays in fused silica’, *Optics express* **14**(13), 6055–6062.
- [114] Szameit, A., Dreisow, F., Pertsch, T., Nolte, S. and Tünnermann, A. [2007], ‘Control of directional evanescent coupling in fs laser written waveguides’, *Optics express* **15**(4), 1579–1587.

- [115] Szameit, A. and Nolte, S. [2010], ‘Discrete optics in femtosecond-laser-written photonic structures’, *Journal of Physics B: Atomic, Molecular and Optical Physics* **43**(16), 163001.
- [116] Tai, M. E., Lukin, A., Rispoli, M., Schittko, R., Menke, T., Borgnia, D., Preiss, P. M., Grusdt, F., Kaufman, A. M. and Greiner, M. [2016], ‘Microscopy of the interacting harper-hofstadter model in the few-body limit’, *arXiv preprint arXiv:1612.05631* .
- [117] Taie, S., Ozawa, H., Ichinose, T., Nishio, T., Nakajima, S. and Takahashi, Y. [2015], ‘Coherent driving and freezing of bosonic matter wave in an optical lieb lattice’, *Science advances* **1**(10), e1500854.
- [118] Tasaki, H. [1998], ‘The hubbard model-an introduction and selected rigorous results’, *Journal of Physics: Condensed Matter* **10**(20), 4353.
- [119] Thouless, D., Kohmoto, M., Nightingale, M. and Den Nijs, M. [1982], ‘Quantized hall conductance in a two-dimensional periodic potential’, *Physical Review Letters* **49**(6), 405.
- [120] Titum, P. [2016], Disorder driven transitions in non-equilibrium quantum systems, PhD thesis, California Institute of Technology.
- [121] Titum, P., Berg, E., Rudner, M. S., Refael, G. and Lindner, N. H. [2016], ‘Anomalous floquet-anderson insulator as a nonadiabatic quantized charge pump’, *Physical Review X* **6**(2), 021013.
- [122] Titum, P., Lindner, N. H., Rechtsman, M. C. and Refael, G. [2015], ‘Disorder-induced floquet topological insulators’, *Physical Review Letters* **114**(5), 056801.
- [123] Tran, D.-T., Dauphin, A., Goldman, N. and Gaspard, P. [2015], ‘Topological hofstadter insulators in a two-dimensional quasicrystal’, *Physical Review B* **91**(8), 085125.
- [124] Valiente, C. et al. [2010], ‘Few quantum particles on one dimensional lattices’.

- [125] Valiente, M., Küster, M. and Saenz, A. [2010], ‘Frustrated collisions and unconventional pairing on a quantum superlattice’, *EPL (Europhysics Letters)* **92**(1), 10001.
- [126] Valiente, M. and Petrosyan, D. [2008], ‘Two-particle states in the hubbard model’, *Journal of Physics B: Atomic, Molecular and Optical Physics* **41**(16), 161002.
- [127] Valiente, M. and Petrosyan, D. [2009], ‘Scattering resonances and two-particle bound states of the extended hubbard model’, *Journal of Physics B: Atomic, Molecular and Optical Physics* **42**(12), 121001.
- [128] Valiente, M., Petrosyan, D. and Saenz, A. [2010], ‘Three-body bound states in a lattice’, *Physical Review A* **81**(1), 011601.
- [129] Valiente, M. and Zinner, N. T. [2017], ‘Quantum collision theory in flat bands’, *Journal of Physics B: Atomic, Molecular and Optical Physics* **50**(6), 064004.
- [130] Vicencio, R. A., Cantillano, C., Morales-Inostroza, L., Real, B., Mejía-Cortés, C., Weimann, S., Szameit, A. and Molina, M. I. [2015], ‘Observation of localized states in lieb photonic lattices’, *Physical review letters* **114**(24), 245503.
- [131] Vicencio, R. A. and Johansson, M. [2013], ‘Discrete flat-band solitons in the kagome lattice’, *Physical Review A* **87**(6), 061803.
- [132] Vicencio, R. A. and Mejía-Cortés, C. [2013], ‘Diffraction-free image transmission in kagome photonic lattices’, *Journal of Optics* **16**(1), 015706.
- [133] Vidal, G. [2004], ‘Efficient simulation of one-dimensional quantum many-body systems’, *Physical Review Letters* **93**(4), 040502.
- [134] Vidal, J., Douçot, B., Mosseri, R. and Butaud, P. [2000], ‘Interaction induced delocalization for two particles in a periodic potential’, *Physical Review Letters* **85**(18), 3906.
- [135] Vidal, J., Mosseri, R. and Douçot, B. [1998], ‘Aharonov-bohm cages in two-dimensional structures’, *Physical Review Letters* **81**(26), 5888.

- [136] Von Neuman, J. and Wigner, E. [1929], ‘Über merkwürdige diskrete eigenwerte. über das verhalten von eigenwerten bei adiabatischen prozessen’, *Physikalische Zeitschrift* **30**, 467–470.
- [137] White, S. R. [1992], ‘Density matrix formulation for quantum renormalization groups’, *Physical Review Letters* **69**(19), 2863.
- [138] Winkler, K., Thalhammer, G., Lang, F., Grimm, R., Denschlag, J. H., Daley, A., Kantian, A., Buchler, H. and Zoller, P. [2006], ‘Repulsively bound atom pairs in an optical lattice’, *Nature* **441**(7095), 853–857.
- [139] Xia, S., Hu, Y., Song, D., Zong, Y., Tang, L. and Chen, Z. [2016], ‘Demonstration of flat-band image transmission in optically induced lieb photonic lattices’, *Optics letters* **41**(7), 1435–1438.
- [140] Zhang, J., Braak, D. and Kollar, M. [2012], ‘Bound states in the continuum realized in the one-dimensional two-particle hubbard model with an impurity’, *Physical Review Letters* **109**(11), 116405.